Total Temperature Probe Performance for Subsonic Flows using Mixed Fidelity Modeling

Tyler Graham Vincent

Dissertation submitted to the Faculty of the
Virginia Polytechnic Institute and State University
in partial fulfillment of the requirements for the degree of

Doctor of Philosophy
in
Mechanical Engineering

Joseph A. Schetz, Co-Chair
K. Todd Lowe, Co-Chair
Walter F. O'Brien
Wing F. Ng
Joseph W. Meadows

March 25, 2019
Blacksburg, Virginia

Keywords: Total temperature, gas turbine instrumentation, Computational Fluid Dynamics (CFD), Conjugate Heat Transfer (CHT), conduction, convection, radiation

Total Temperature Probe Performance for Subsonic Flows using Mixed Fidelity Modeling

Tyler Graham Vincent

(Abstract)

An accurate measurement of total temperature in turbomachinery flows remains critical for component life models and cycle performance optimization. While many techniques exist to measure these flows, immersed thermocouple based probes remain highly desirable due to well established practices for probe design and implementation in typical industrial flow applications. However, as engine manufacturers continue to push towards higher maximum cycle temperatures and smaller flow passages, the continued use of these probes requires new probe designs considering both improved sensor durability and measurement accuracy. Increased maximum temperatures introduce many challenges for total temperature measurements using conventional immersed probes, including increased influences of conduction, convection, and radiation heat transfer between the sensor, fluid and the surroundings due to large thermal gradients present in real turbomachinery systems. While these effects have been previously investigated, the available design models are very limited to specific geometries and flow conditions. In this Dissertation, a more fundamental understanding of the flow behavior around typical vented shield style total temperature probes as a function of probe geometry and operating condition is gained using results from high-fidelity Computational Fluid Dynamics simulations with Conjugate Heat Transfer. A parametric study was conducted considering three non-dimensional probe geometric ratios (vent location to shield length (0.029-0.806), sensor diameter to shield inner diameter (0.252-0.672), and shield outer diameter to strut/mount thickness (0.245-0.759)) and three operating conditions (total temperature (70, 850, 2500°F) and pressure (1, 1, 10 atm), respectively) at a moderate Mach number of 0.4. Results were further quantified in the form of new empirical correlations necessary for rapid thermal performance evaluations of current and future probe designs. Additionally, a new mixed-fidelity or Reduced Order Modeling technique was developed which allows the coupling of high fidelity surface heat transfer data from CFD with a generalized form of the 1-D conducting solid equations for evaluating radiation and transient influences on sensor performance. These new flow and heat transfer correlations together with the new Reduced Order Modeling technique developed here greatly enhance the capabilities of designers to evaluate performance of current and future probe designs, with higher accuracy and with significant reductions in computational resources.

(349 words)

This work received support from Pratt & Whitney through the Center of Excellence at Virginia Tech.

Total Temperature Probe Performance for Subsonic Flows using Mixed Fidelity Modeling

Tyler Graham Vincent

(General Audience Abstract)

An accurate measurement of total temperature in turbomachinery flows remains critical for component life models and cycle performance optimization. While many techniques exist to measure these flows, immersed thermocouple based probes remain highly desirable due to well established practices for probe design and implementation in typical industrial flow applications. However, as engine manufacturers continue to push towards higher maximum cycle temperatures and smaller flow passages, the continued use of these probes requires new probe designs considering both improved sensor durability and measurement accuracy. Increased maximum temperatures introduce many challenges for total temperature measurements using conventional immersed probes, including increased influences of conduction, convection, and radiation heat transfer between the sensor, fluid and the surroundings due to large thermal gradients present in real turbomachinery systems. While these effects have been thoroughly described and quantified in the past, the available design models are very limited to specific geometries and flow conditions. In this Dissertation, a more fundamental understanding of the flow behavior around typical vented shield style total temperature probes as a function of probe geometry and operating condition is gained using results from high-fidelity Computational Fluid Dynamics simulations with Conjugate Heat Transfer (CHT) capabilities. Results were further quantified in the form of new empirical correlations necessary for rapid thermal performance evaluations of current and future probe designs. Additionally, a new mixed-fidelity or Reduced Order Modeling (ROM) technique was developed which allows the coupling of high fidelity surface heat transfer data from CFD with a generalized form of the 1-D conducting solid equations for readily predicting the impact of radiation environment and transient errors on sensor performance.

Acknowledgements

I have many individuals to acknowledge during my graduate school journey. I would like to begin with my co-advisor Dr. Joseph A. Schetz. It was because of his support that I ultimately decided to pursue my Doctorate of Philosophy. Beyond his support of project and research needs, he gave me many opportunities to travel the world for conference presentations, resulting in experiences that I will never forget. Second, I would like to strongly acknowledge the support of my co-advisor Dr. K. Todd Lowe. He provided regular research and technical guidance that allowed me to continually contribute to my project and research goals. He also secured project funding throughout the duration of my graduate school career, for which I am extremely grateful.

I would like to acknowledge the insightful technical discussions with Dr. Charles Haldeman, Andy Consiglio, and Ian Agoos at Pratt & Whitney. It is your feedback that progressed much of the work presented in this Dissertation. Also, thank you Eric Rolfe for providing your computational efforts that provided many of the necessary components for the analysis presented in Chapter 3 of this Dissertation.

Next, I acknowledge the necessary emotional support of my friends, many of whom I have met during my time at Virginia Tech. I have enjoyed the time spent with my fellow students in the CREATE group in the Aerospace and Ocean Engineering, who despite my associations with the Mechanical Engineering Department have accepted me as on of their own. I am also honored to have had the opportunity to play club ultimate with VT Burn and finally make it to Nationals.

During my time at Virginia Tech, I was lucky enough to meet the love of my life, Samantha Sunshine. Finding you has made this whole journey worthwhile.

Lastly, I would like to dedicate this Dissertation to my Family who have always supported my endeavors. To my parents, Myron and Vicki Vincent and my brother, Aaron Vincent, I love you.

Tyler G. Vincent
March 2019

Contents

List of Figures

List of Tables

Attributions

Several professors and colleagues contributed to the research and writing contained in this Dissertation. A brief description of their contributions is included below:

Dr. Joseph A. Schetz and Dr. K. Todd Lowe are co-advisors and committee chairs for this research. Both provided extensive guidance on the research plan, secured research funding, and provided editorial revisions and advice on the analysis of all data in manuscripts.

Dr. Charles Haldeman is a technical fellow at Pratt & Whitney. He provided extensive guidance on the research plan and facilitated weekly technical discussions.

Ian Agoos is an engineer in the Systems Engineering and Validation group at Pratt & Whitney. He provided extensive guidance on the research plan and facilitated weekly technical discussions.

Eric Rolfe is a Master of Science recipient of the Aerospace and Ocean Engineering Department at Virginia Tech. He contributed significantly by conducting a portion of the simulations presented in Chapter 3.

[this page intentionally left blank]

1. Introduction

The improved measurement of temperature remains a topic of great interest throughout a wide variety of industrial applications. Of particular interest is the measurement of fluid temperatures in various turbomachinery flows for engine control, performance and health management. Both current and future engine designs operate at conditions that test the limits of various engine components in order to achieve the maximum power output and fuel efficiency. This, of course, demands the design of sensors capable of withstanding these extreme environments, while improving measurement accuracy. To accommodate these types of measurements, engineers and researchers are leveraging a wide variety of existing and new sensor technologies, ranging from immersive sensors directly subjected to the measured flow such as thermocouple (TC) , Resistance Temperature Detector (RTD) or fiber optic based sensors, to non-intrusive techniques such as tomography or various laser-based techniques. This Dissertation will focus exclusively on the thermal performance of immersed total-temperature probes. Similar to engine components subjected to high flow temperatures, probe components may be cooled to improve survivability. In the most extreme cases, the sensor itself has material limitations below that of the measured flow temperature, requiring active cooling of the mount and/or sensor. Despite the difficulty of designing a sensor operating in these conditions to directly measure flow temperature, building a fundamental understanding of the heat transfer modes affecting the sensor-indicated temperature is critical for applying the appropriate *a posteriori* corrections.

In a gas turbine engine, the measurement of flow temperatures within the hot section of the engine serves several key functions as enumerated by Bentz et al. (1969): (1) Limiting overtemperature for increased hot section life (2) Cycle performance optimization and power control and (3) Improved engine transient response within thermal cycling limits. Von Moll et al. (2014) added an additional function: (4) More accurate data to input into life consumption models. While more advanced temperature resistant materials and component cooling techniques are being developed and successfully employed, the desired temperature margins between component limitations and ideal operating conditions are still shrinking, requiring these measurements to be made with higher levels of accuracy and reliability. For these temperature measurements to be successful, measurement accuracy must be accompanied with desired spatial and temporal resolution and an acceptable level of survivability for the given operating conditions.

Gaylord et al. (1969) provided an insightful quantitative example that demonstrates the importance of accuracy when measuring turbine inlet temperature (commonly denoted as T4). In the example, a 1400hp gas turbine engine with a maximum T4 of 1750°F would have an expected 50% reduction in turbine blade life if the operational temperature was increased by just 30°F above maximum T4. Conversely, if the maximum T4 temperature was decreased by 30°F, the engine would lose 50hp of power output, which would amount to a 700lb reduction in payload for a twin engine helicopter powered by these engines. In many fuel control systems, it is the measurement of T4 that provides information to the engine controls, thus error during temperature measurement is directly responsible for component life cycle reductions or reduced engine performance.

The goal of this Dissertation is to introduce new and improved models and tools necessary for the rapid evaluation and design of immersed total temperature probes tailored for use in subsonic, high-temperature flow environments. Computational Fluid Dynamics (CFD) simulations with Conjugate Heat Transfer (CHT) capabilities was heavily relied upon to accurately quantify flow and heat transfer behavior on fine length scales on and around the probes investigated. These investigations revealed fundamental insights to the physics governing probe performance based on the probe geometric design and operating environment. These insights were used for the creation of new empirical models for rapid evaluation of current and new probe designs. Additionally, a new reduced-order performance evaluation technique was developed allowing for the coupling of high fidelity surface heat transfer data from CFD with a generalized form of the 1-D conducting solid equations for readily predicting the impact of radiation environment and transient errors on sensor performance.

1.1 Dissertation Structure and Contents

This Dissertation is divided into the following chapters:

Chapter 1 provides a general introduction and overview of the Dissertation.

Chapter 2 presents a literature review of the relevant theory behind the work.

Chapter 3 is the first manuscript, "Aerodynamic Analysis of Total Temperature Probe Thermal Performance using Conjugate Heat Transfer," to be published in Journal of Thermophysics and Heat Transfer. This paper provides a deeper understanding of the flow physics responsible for establishing the convective heat transfer on the sensor surface of vented-shield style total temperature probe. See Figure 1.1 for a typical probe. This was accomplished by using high-fidelity Computational Fluid Dynamics (CFD) with Conjugate Heat Transfer (CHT) to examine the details of the aerodynamic environment establishing the heat transfer on the surface. A parametric study was conducted considering three non-dimensional probe geometric ratios (vent location to shield length (x_{vent}/L_{shield} = 0.029-0.806), sensor diameter to shield inner diameter (d_{sensor}/d_{shield} = 0.252-0.672), and shield outer diameter to strut/mount thickness (D_{shield}/t_{strut} = 0.245-0.759)) and three operating conditions (total temperature (70°F, 850°F, 2500°F) and pressure (1 atm, 1 atm, 10 atm), respectively) all at a moderate Mach number of 0.4. These investigations led to the development of a new non-dimensional parameter based on the ratio of the actual to ideal mass flow rate into a vented shield allowed for quantification of sensor local Reynolds numbers, which better describe the convection heat transfer into the sensor. An empirical correlation for this new mass flow ratio was developed and further shown to be largely independent of the free stream flow Reynolds number. Lastly, new Stanton-Reynolds number correlations were developed for estimation of the convection heat transfer coefficients along the tip and side regions of the sensor where forced convection exists.

Chapter 4 is the second manuscript, "Enhanced Low-Order Model with Radiation for Total Temperature Probe Analysis and Design," published in the SAE International Journal of Aerospace. This work addresses the need for a simple tool for the rapid, yet accurate, estimation of radiation error impacting total temperature measurements in high temperature environments by providing a numerical solution code (MATLAB based) for a highly generalized 1-D conducting sensor analogous to a so-called pin fin with simultaneous conduction, convection and radiation heat transfer. The code is validated by comparing the numerical solutions to available exact solutions from the literature. Various examples are provided to show the influence of radiation on sensor shapes with

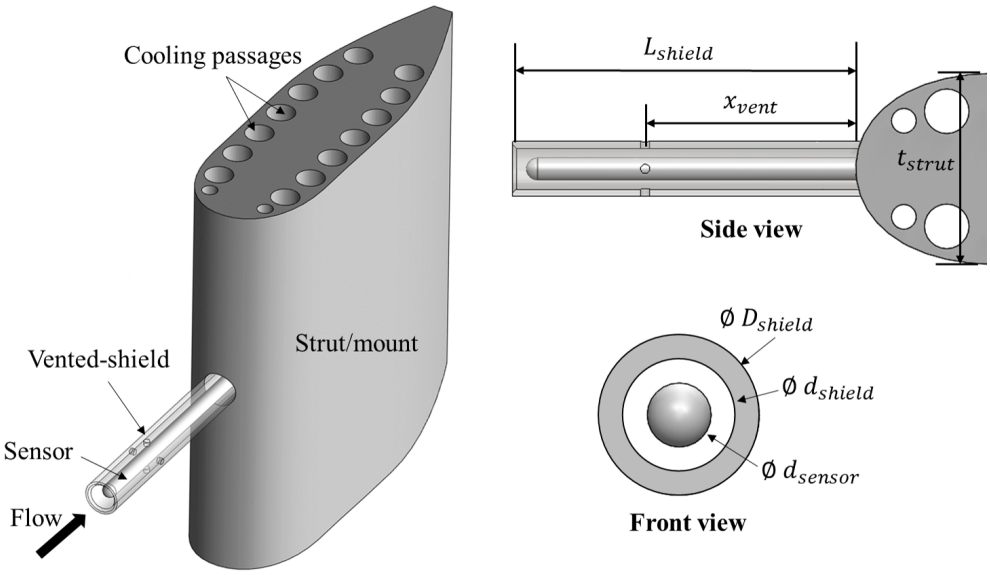

Figure 1.1: Typical vented-shield style total temperature probe.

different length to diameter ratios, axially varying area profiles, non-uniform convection coefficient distributions, and variable thermal conductivity.

Chapter 5 is the final manuscript, "Analysis of Pin Fins Including Radiation and Transients," to be published in Computational Thermal Sciences. This work builds on the work of "Enhanced Low-Order Model with Radiation for Total Temperature Probe Analysis and Design," further generalizing the numerical solution to include transients. Further examples including temperature time response due to temporally changing boundary conditions greatly enhances the applicability of this numerical solution to total temperature probes in transient environments as well as other generalized applications where accurate estimations of temperature profile or heat transfer from a 1-D conducting fin is required. Additionally, a new Reduced Order Modeling (ROM) approach was developed, which couples high-fidelity surface heat transfer data from CFD with the generalized 1-D fin equations, allowing for more rapid estimations of fin thermal profiles due to variations in key problem parameters (i.e. fin material, fin base temperature, surrounding temperature for radiation, etc.) at a fraction of the cost of subsequent high-fidelity computations.

Chapter 6 concludes the overall research efforts and provides an outlook on future work.

Formatting of each chapter contents and citation style may deviate due to the different publication guidelines of the journal in which they have or will be published.

1.2 Achievements

Key outcomes of the present research include:

- Development of a new low-order analytic conduction model designed to account for the distinct convection heat transfer regions over the surface of a sensor contained inside a vented shield.
- A detailed visualization and quantification of the flow field around shielded probes with various geometries using CFD/CHT modeling enhanced the understanding of convection heat transfer behavior along the sensor surface.
- The development of a new non-dimensional parameter based on the ratio of the actual to ideal mass flow rate into a vented shield allowed for quantification of sensor local Reynolds numbers, which better describe the convection heat transfer into the sensor.
- An empirical correlation for this new mass flow ratio was developed as a function of key probe geometric parameters including vent position, shield inner and outer diameters, sensor diameter, and strut/mount thickness. This correlation was further shown to be largely independent to the free stream flow Reynolds number over the ranges tested, making this correlation applicable to a wide range of operating conditions.
- New Stanton-Reynolds number correlations were developed using CFD/CHT for estimating convection heat transfer coefficients along the tip and side regions of the sensor where forced convection exists.
- A MATLAB script capable of solving a highly generalized version of the 1-D pin-fin equations was developed, allowing for the solution of the temperature distribution in a sensor-representative homogeneous rod with simultaneous conduction, convection, and radiation heat transfer not possible with existing analytic solutions.
- A new Reduced Order Modeling technique was created allowing for the coupling of high fidelity surface heat transfer data from CFD with a generalized form of the 1-D conducting solid equations for readily predicting the impact of radiation environment and transient errors on sensor performance.

1.2.1 List of Publications

The scientific publications of the author during his Ph.D. work are listed in this section.

Peer-reviewed Journal Publications:

- T. G. Vincent, J. A. Schetz, K. T. Lowe. Aerodynamic Analysis of Total Temperature Probe Thermal Performance using Conjugate Heat Transfer. *Accepted pending revisions in Journal of Thermophysics and Heat Transfer, 2019.*
- T. G. Vincent, J. A. Schetz, K. T. Lowe. Enhanced Low-Order Model with Radiation for Total Temperature Probe Analysis and Design. In *SAE International Journal of Aerospace* 11(1):47-60,2018. doi: 10.4271/01-11-01-0003
- T. G. Vincent, J. A. Schetz, K. T. Lowe. Analysis of Pin Fins Including Radiation and Transients. *Accepted in Computational Thermal Sciences, 2019.*

Conference Proceedings:

- T. G. Vincent, J. A. Schetz, K. T. Lowe. Analysis of Base-Cooled Total Temperature Probes With Radiation. In *ASME International Mechanical Engineering Congress and Exposition*, Paper No. IMECE2016-65130, 2016.
- T. G. Vincent, J. A. Schetz, K. T. Lowe. Enhanced Low-Order Model with Radiation for Total Temperature Probe Analysis and Design. In *SAE International AeroTech Congress & Exhibition*, Paper No. 2017-01-2047, 2017.
- T. G. Vincent, J. A. Schetz, K. T. Lowe. Analysis of Pin Fins With Radiation. In *13th International Conference on Heat Transfer, Fluid Mechanics, and Thermodynamics*, 2017. uri: `http://hdl.handle.net/2263/62422`

2. Literature Review

2.1 History of Total Temperature Probe Design

Dating back to the early 20th century, researchers used immersed temperature sensors (thermocouples and mercury thermometers were most common) in an attempt to measure temperatures in high-velocity fluids (Stodola (1903); Batho (1908); Nusselt (1916); Müller (1920); Wimmer (1941)). These pioneering investigations revealed that instead of an immersed sensor measuring fluid static temperature as was originally anticipated, the sensor indication tends toward the stagnation temperature due to the interaction of the sensor and the oncoming fluid. This discovery motivated the next generation of probes to incorporate features designed to stagnate the oncoming fluid, with the new goal of measuring the fluid total (or stagnation) temperature rather than the static temperature.

In order to better describe the temperatures being measured by these various sensors, a temperature recovery factor, r, was devised, which states the ratio of the measured temperature rise to adiabatic temperature rise (Equation 2.1):

$$r = \frac{T_{measured} - T_s}{T_t - T_s} \tag{2.1}$$

A recovery factor of r = 0 indicates the exact measurement of the flow static temperature (T_s), whereas a factor of r = 1.0 indicates the exact measurement of the flow total temperature (T_t). As indicated by Hottel and Kalitinsky (1945), many early attempts to correlate measured recovery factors with probe shape or test conditions were unsuccessful, attributing these failures to a lack of care to mitigate conduction and radiation errors. These errors are described later here in more detail. Hottel and Kalitinsky (1945) performed a wide range of experiments in an effort to better describe recovery performance for thermocouple sensors of various shapes in a range of flow conditions, all the while taking care to isolate sensor recovery from conduction and radiation. These tests showed that thermocouple junction shape (spherical or butt-welded), wire alignment to flow (axial or perpendicular), and twisted or untwisted lead wires have a significant impact on the

resulting recovery, and each responds differently to increases in flow velocity.

In the late 1930's and 1940's, the measurement of temperature in high-velocity air streams became desirable for the estimation of aircraft-engine supercharger efficiency and power output (Hottel and Kalitinsky (1945)). At this time, the understanding of total versus static temperature measurements was well understood, and most probes were designed with the goal of measuring the former. Franz (1940), one of the first to attempt the design and experimentation of true total-temperature sensors, designed and tested two probe configurations in which the flow was stagnated or diffused, shown in Figure 2.1.

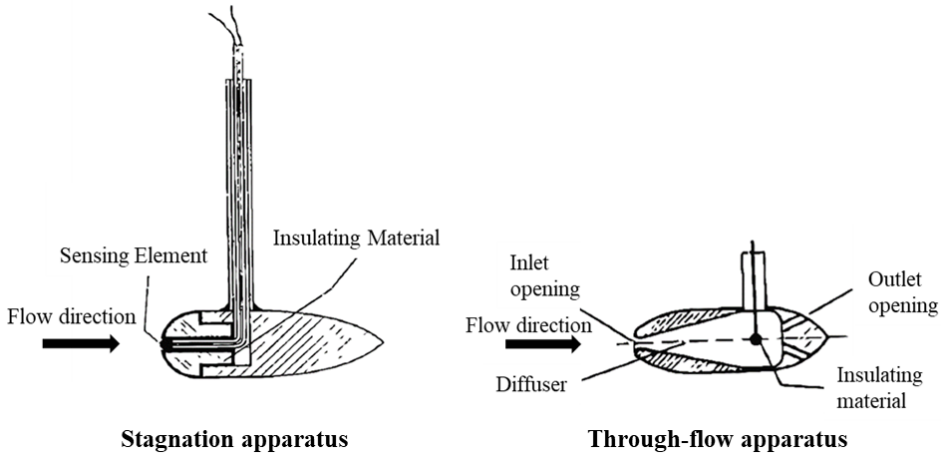

Figure 2.1: Franz (1940) total temperature probe designs.

The probe shown in Figure 2.1 (left) was designed to completely stagnate the flow at the sensing element. Compared to a sensor directly immersed in the flow, this stagnated sensor achieved much higher temperature recoveries. However, this sensor design was highly sensitive to cross-flow velocities due to the shifting of the stagnation point location on the probe body away from the sensing location. The second probe shown in Figure 2.1 (right) attempted to remedy this angle sensitivity by allowing a small portion of the free-stream flow to pass through the probe body where the sensor was located before discharging back into the free-stream. Still true to date, this bleed flow was required to ensure the sensor is exposed to fluid at the current total temperature (especially critical in transient flows), rather than stagnated fluid that has lost energy to the probe via heat transfer over a long duration. The flow entering the probe was internally diffused before passing over the sensor at a low enough velocity to allow total flow conditions to be easily assumed. This design achieved noticeable improvements with regards to off-angle sensitivity, and would be shown later to further mitigate conduction and radiation heat transfer effects via fluid heat convection. Hottel and

Kalitinsky (1945) tested a reduced-scale Franz (1940) diffuser-style probe, but observed a highly sensitive response to off-angle flows and significantly reduced recovery values, likely attributed to the reduction in overall probe size and increased boundary layer influences. Lindsey (1942), who tested several variations of the Franz-type probe in a high speed wind-tunnel, also observed a decreased temperature recovery as probe size decreased. The performance of the Franz-type probe was further complicated by inherent instabilities in the diffuser when operating in specific Reynolds number regimes. The Franz-type probe design was soon to be out-performed by two "straight-tube" diffusing probes designed by MIT and Pratt & Whitney as shown in Figure 2.2, each of which had very similar performance characteristics with respect to flow velocity, flow angle, and radiation error correction. Despite similar performance, the Pratt & Whitney probe, only requiring a single diffusing shield, was more desirable due to the improved sensor performance relative to the Franz-type probe and simplicity of design compared to the MIT probe.

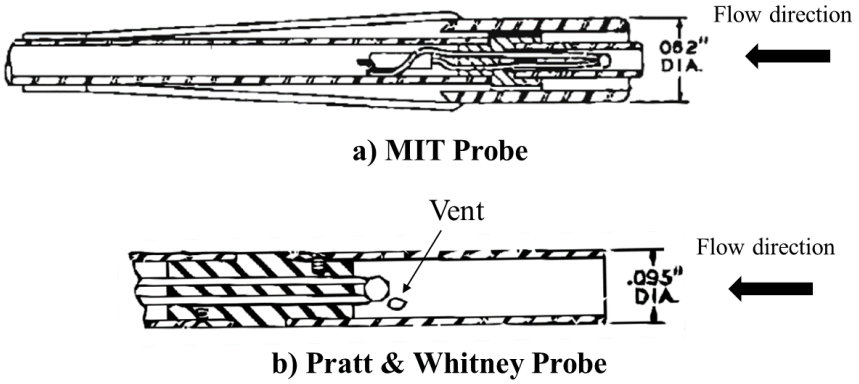

Figure 2.2: Early "Straight-tube" vented-diffuser style total temperature probes designed by MIT and Pratt & Whitney with nearly identical thermal performance characteristics (Hottel and Kalitinsky (1945)).

Around the same time, King (1943) worked on probe designs specifically for Exhaust Gas Temperature (EGT) measurements in the exhaust-gas pipe of engines. Similar to flows in superchargers, the exhaust gas flows are at high velocity, resulting in errors due to the non-ideal conversion of fluid kinetic energy to thermal energy at the sensor surface. Further measurement errors are introduced when attempting to measure the temperature of high temperature fluids. One such error is conduction heat transfer from the sensor junction along the sensor wires or along the protective tube or mounting. King (1943) readily showed the effects of conduction could be mitigated by increasing the length of immersion of the probe in the flow, due to the increased length of convection heat transfer from the moving fluid into the sensor. The second error is radiation heat transfer

from the sensor junction to the surroundings at a different temperature. One way to mitigate this error is to set the temperature of the surroundings equal to the sensor temperature. While it is impractical to enforce this relationship in a real engine environment, the use of a shield(s) placed concentrically around the sensor would act as the primary surrounding surface that drives radiation heat transfer to or from the sensor. Because the shield would be subjected to the same flow as the sensor, it is likely that the shield temperature would be more similar to that of the sensor, minimizing heat transfer and associated radiation measurement errors. King (1943) performed a series of tests comparing the performance of a thermocouple sensor in unshielded, single-shielded, and multi-shielded configurations. See Figure 2.3 for an example quadruple-shielded thermocouple used in King's studies. As expected, results show that radiation errors were made less significant as more shields were added. By combining the presented benefits of a shield on radiation errors in high temperature environments with the reduced velocity errors in high speed flows, it is clear to see why many of the more modern probe designs employ some variation of the vented shield design.

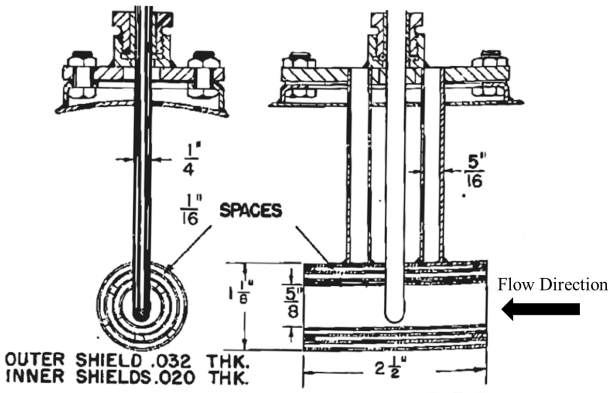

Figure 2.3: Quadruple-shielded thermocouple design tested (King (1943)).

Later, Glawe et al. (1956) conducted a series of experiments in order to measure the time response, radiation and conduction corrections, and aerodynamic heating effects for various shielded and unshielded thermocouple probe designs. These probe designs were each created with a specific measurement objective. Of the shielded probes tested, three were aspirated, meaning air was forced across the sensor due a suction pressure line attached to one end of the probe. This style probe is desirable because the flow subjected to the sensor can be more directly controlled, compared to more passive, non-aspirated designs that are based entirely on aerodynamic behavior resulting from probe interactions with the free stream. In one aspirated probe, the sensor junction was placed at the throat of a venturi nozzle section where the flow was designed to be sonic. It

was observed that creating a high velocity flow past the sensor, the time response of the sensor to temperature changes in the measured flow was significantly improved. The improved time response of the sonic aspirated probe comes at the cost of increased manufacturing difficulty and performance sensitivity to junction placement within the venturi body compared to the subsonic, double-shielded, aspirated probes also tested. Glawe et al. (1956) also performed a series of tests directly comparing the performance of a "wedge-shaped" bare wire sensing element aligned with the wedge facing the flow both shielded and unshielded (see Figure 2.4). Experimental results showed that by shielding the sensor, the required radiation correction was halved, but the time response was decreased threefold. Glawe et al. (1956) remarked from this study that probe selection for a given application would likely involve a compromise among desirable characteristics; that is still highly true today.

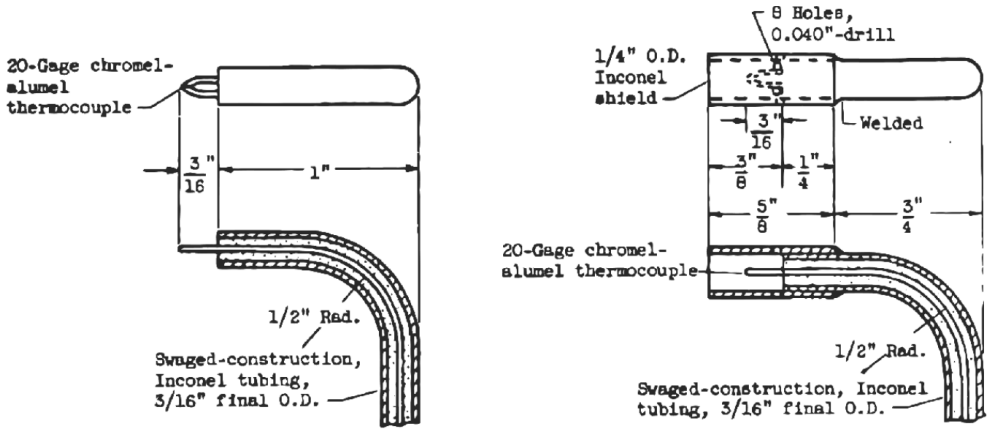

Figure 2.4: Unshielded (left) and shielded (right) wedge-shaped thermocouple probes tested (Glawe et al. (1956)).

In the early 1950's, interest in high supersonic and hypersonic boundary layer stagnation temperature measurements for aeroballistics research led to the development of shielded thermocouple based stagnation temperature probes. One of the earliest known works in this area was conducted by Winkler (1954), whose goal was to obtain temperature surveys of turbulent boundary layers on the nozzle wall of a hypersonic tunnel with Mach numbers between 1.5 and 7.6, supply pressures up to 50 atmospheres, and supply temperatures up to 800K. Since boundary layer flows have large gradients (velocity and temperature) in the wall-normal direction, high spatial resolution can only be achieved with probes having small overall heights. Due to the high velocity of the fluid being measured, a shielded design is desirable for adequately diffusing the oncoming flow to a low enough velocity for stagnation conditions to be assumed, as well as minimizing radiation heat transfer from the sensor to the surroundings. Using probes with 1mm shield inlet height, Win-

kler (1954) was able to successfully measure temperature profiles well into the laminar sublayer (0.5mm from the wall) in a 1 inch turbulent hypersonic boundary layer. Similar measurements were conducted by Albertson and Bauserman Jr. (1993) with flattened shielded probes (Figure 2.5) agreeing well with Crocco-Busemann predictions for the enthalpy distribution in a high speed boundary layer.

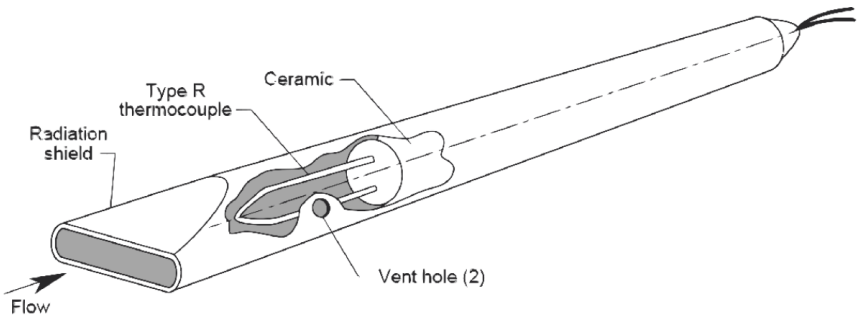

Figure 2.5: Probe design used by Albertson and Bauserman Jr. (1993) for the measurement of hypersonic boundary layer temperature profiles over a flat plate.

Of high significance to the work later presented in this Dissertation was Winkler's insight regarding the correlation of fluid convection heat transfer coefficient on the sensor to shield internal flow conditions, rather than free stream flow conditions. It will be later shown that sensor recovery due to conduction error is a strong function of the convective heat transfer coefficient on the sensor surface. Winkler (1954) showed that for a given probe, sensor recovery was strongly correlated to sensor Nusselt number, which was experimentally shown to relate to a function of the shield internal stagnation temperature and shield internal density. See Equation (2.2).

$$\left(Nu\frac{k_f}{k}\right)^2 \propto \frac{\rho}{T_t^{3/4}} \tag{2.2}$$

The impact of the use of shield internal flow conditions is better illustrated graphically. Figure 2.6 shows the variation of probe temperature recovery factor with free stream Reynolds number for various free stream Mach numbers. It can be observed that the sensor recovery is clearly a function of both Reynolds number and Mach number, therefore it cannot be fully described by the free stream Reynolds number alone. By using the shield internal density and total temperature parameter presented in Equation 2.2, the same temperature recovery factor data in Figure 2.6 was shown to be fully described by a single curve in Figure 2.7.

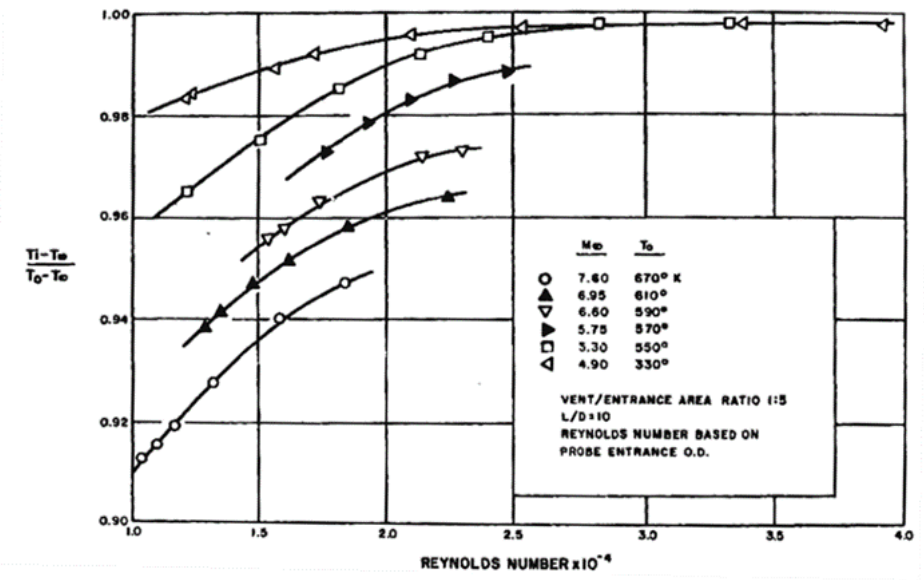

Figure 2.6: Temperature Recovery factor (see Equation 2.1) versus free stream Reynolds number at various free stream Mach numbers (Winkler (1954)).

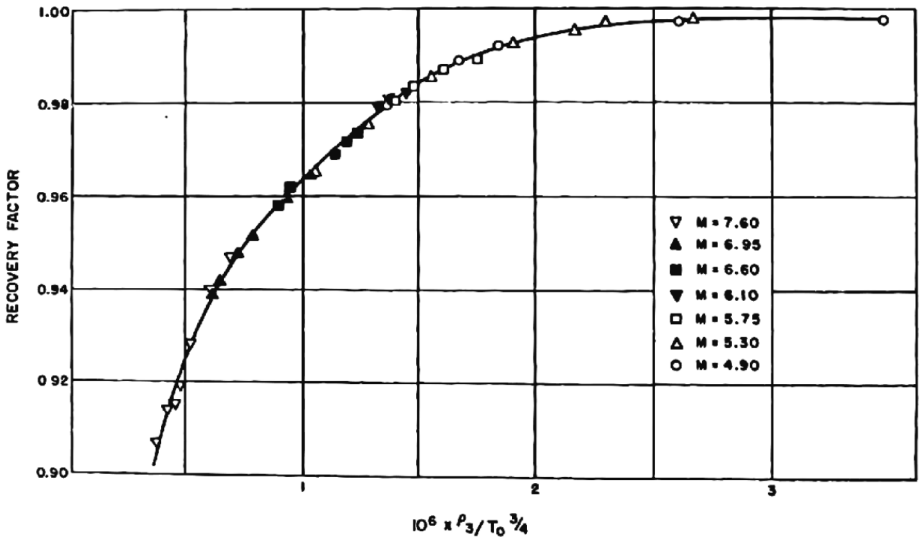

Figure 2.7: Temperature recovery factor versus $\rho/T_t^{3/4}$ at various free stream Mach numbers, where the density is based on shield internal flow conditions (Winkler (1954)).

For most work regarding total temperature probe design and performance, the main objective has been to maximize sensor recovery. In other words, it is the goal of the designer to create a probe that is expected to have a sensor indicated temperature as close to the flow total temperature as possible. Of course, the maximization of sensor recovery requires an understanding of the

sources of sensor error and how each of these errors can be mitigated (these primary sensor errors will be discussed in detail in a later section). It has been made clear from the experimental works summarized here that the design requirements of a high recovery probe are well understood and easily practiced. However, for extreme temperature measurements approaching or even exceeding the probe material temperature limitations, high sensor recoveries become undesirable since the immersed probes will begin to fail. This problem was foreseen as early as the 1960's by Gaylord et al. (1969), who considered the future measurement of a jet engine hot section designed with maximum temperatures reaching 3000°F. While these temperatures are high, the use of noble and refractory metals such as platinum, rhodium, tungsten, rhenium, and tantalum and high temperature ceramics such as alumina for electric insulation allowed for enough temperature and oxidation resistance for operation in this range. Recently, the Department of Energy's Advanced Turbines Program aims to achieve turbine inlet temperatures of 3100°F for combined cycle applications, further complicating the use of these materials in this environment (www.netl.doe.gov (2019)). Von Moll et al. (2014) provide an excellent presentation of the expected engine operating conditions for future engines based on historical engine performance growth aided by technological advancements as shown in Figure 2.8, and these engines are expected to operate well beyond the physical limitations of currently available materials. For the continued use of currently available immersed temperature sensors at these extreme temperature ranges, one must deliberately reduce sensor recovery in a known fashion to allow for prolonged probe survivability. This can be achieved by the deliberate cooling of various probe components, ultimately impacting the sensor indicated temperature via combined heat transfer modes (Anderson et al. (2008); Moeller et al. (2012)). For a low-recovery sensor to be useful, understanding these heat transfer modes and developing models that can accurately predict the impact of probe cooling on sensor recovery is critical.

2.2 Total Temperature Measurement Errors

Errors are inherent to the measurement of temperature in high speed and/or high temperature flows using any stationary immersed probe. These errors arise due to compressible/viscous aerodynamic effects due to sensor interaction with oncoming fluid, as well as various heat transfer methods due to inevitable thermal gradients present in the flow, probe, and surroundings. In most total temperature probe applications, four main error sources must be considered: velocity error, conduction error, radiation error, and transient error. In this chapter, each error source is physically described, available error quantification models are summarized from the literature, and known error mitigation techniques are introduced.

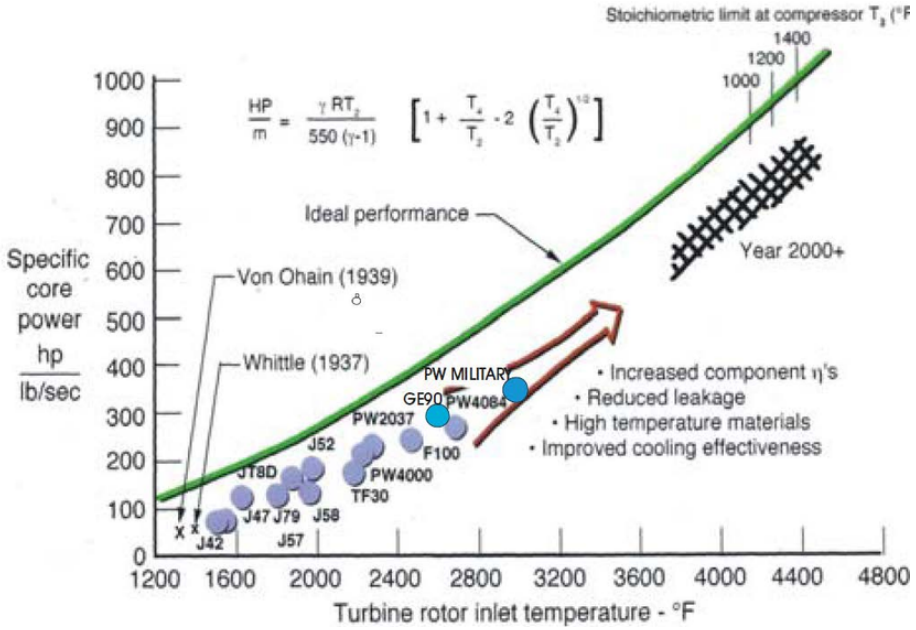

Figure 2.8: Trend of jet engine specific core power versus turbine rotor inlet temperature for past and future engines (Von Moll et al. (2014)).

2.2.1 Velocity Error

For a moving fluid, the total enthalpy is defined as the sum of the static enthalpy and the fluid kinetic energy as:

$$h_t = h_s + \frac{V^2}{2} \tag{2.3}$$

For a perfect gas, $h = c_p T$, thus Equation 2.3 can be rewritten to give the total temperature as:

$$T_t = T_s + \frac{V^2}{2c_p} = T_s(1 + \frac{\gamma - 1}{2} M^2) \tag{2.4}$$

During the process of fluid stagnation, the fluid kinetic energy is converted to internal energy. This energy conversion physically presents itself as a fluid temperature rise towards the stagnation temperature. During ideal stagnation, the kinetic energy of the fluid is perfectly converted to internal energy, and the resulting fluid temperature would assume the fluid total temperature. A sensor placed in this ideally stagnated region, excluding other heat transfer effects, would be expected to exactly measure the flow total temperature.

For most immersed temperature sensors, complete stagnation is unrealistic and often undesirable. Most real sensors will experience some degree of fluid motion, resulting in boundary layer development on the sensor surface. It is well known that the velocity of the fluid along a solid wall in a boundary layer is zero, thus it is tempting to assume that the fluid temperature at the wall should be equal to the free stream total temperature due to complete stagnation. However, this assumption is incorrect, and one must further consider thermal dissipation of heat throughout the boundary layer. For the estimation of the fluid temperature at an adiabatic wall (i.e. no heat exchange is allowed between the fluid and wall boundary), one may use (Schetz and Bowersox (2011)):

$$T_{aw} = T_s + r\frac{V^2}{2c_p} \tag{2.5}$$

Similar to total temperature, the adiabatic wall temperature is represented as a sum of the static and free stream kinetic energy. However, unlike total temperature, the kinetic energy term is scaled by a recovery factor, r. This recovery factor represents the portion of kinetic energy that is converted or, more accurately, recovered as internal energy at the wall surface. Perfect kinetic energy recovery would be represented as a recovery factor of unity, however, thermal dissipation throughout the boundary layer results in $r < 1$. For a laminar flow over a flat plate, this recovery factor can be approximated as the square root of the Prandtl number (Pohlhausen (1921); Emmons and Brainerd (1941)). Hottel and Kalitinsky (1945) observed $r \approx \sqrt{Pr}$ to be true even for small, bare wire thermocouples where $d\sqrt{V} > 0.01$, although this result was not definitive due to lack of experimentation. For a turbulent boundary layer on a flat plate, $r \approx \sqrt[3]{Pr}$ (Schetz and Bowersox (2011)).

Assuming that conduction and radiation heat transfer effects are negligible, the indicated sensor temperature T_j would be expected to equal the adiabatic wall temperature. Substituting T_j for T_{aw} and including isentropic compressibility relations to define the relationship between static and total temperatures, Equation 2.6 can be rewritten (Moffat (1962)):

$$T_j = T_t\left[1 - (1-r)\frac{\frac{\gamma-1}{2}M^2}{1+\frac{\gamma-1}{2}M^2}\right] \tag{2.6}$$

Using experimentally measured recovery results (Hottel and Kalitinsky (1945); Glawe et al. (1956); Simmons (1954)) for bare wire thermocouples with flow aligned normal and parallel to the wires, Moffat (1962) recommended the following values for bare wire probe design for Mach number

from 0.1 to 1.0 and Reynolds number (based on sensor diameter) from 100 to 10,000 (Equations 2.7 and 2.8):

$$r = 0.68 \pm 0.07 \text{ (wires normal to flow)} \tag{2.7}$$

$$r = 0.86 \pm 0.09 \text{ (wires parallel to flow)} \tag{2.8}$$

As can be observed by Equation 2.6, velocity error is entirely dependent on flow Mach number and velocity recovery factor. Therefore, velocity error can be decreased by decreasing flow Mach number (by decreasing velocity over the sensor) or by increasing the velocity recovery factor by directing the flow parallel to the wires. To date, there is no proven analytic technique to accurately predict velocity recovery factor. Instead, velocity recovery determination requires precise experimentation that is valid only for the given sensor geometry and flow alignment.

2.2.2 Conduction Error

For most immersed temperature probes, the sensing element is physically held by a fixture or mount. If the mount temperature is different than the sensing element, conduction heat transfer will impact the sensing element temperature. One dimensional heat conduction in its basic form can be described using Fourier's Law of Conduction (Equation 2.9) (Incropera (2007)) :

$$q_{cond} = -kA_c \frac{dT}{dx} \tag{2.9}$$

From Fourier's Law, conduction heat transfer is decreased if the thermal conductivity, cross sectional area, or temperature gradient are decreased, independently or in combination. Thus Fourier's Law alone provides a thorough set of design guidelines for the minimization of conduction error. However, it is common to consider the influence of fluid convection heat transfer simultaneously with conduction, since most sensors will be subjected to a moving fluid. Heat transfer due to convection is most commonly defined using Newton's Law of Cooling (Equation 2.10), stating that the heat transfer between a fluid and solid body is proportional to the temperature difference between the fluid and solid, scaled by a convective heat transfer coefficient times the heat transfer area, written as (Incropera (2007)):

$$q_{conv} = hA_s(T - T_f) \tag{2.10}$$

Consider now a long, slender, circular cylinder with length L and diameter d, mounted at one end to a body with temperature T_b and subjected to a moving fluid with temperature T_f as is illustrated in Figure 2.9. This geometry is intended to represent a temperature sensor with a sensing junction temperature T_j that is impacted by the combined axial conduction heat transfer within the sensor body and fluid convection into the tip and sides of the sensor body. The steady-state energy balance for a cylindrical differential element shows that the change in axial conduction heat transfer rate is equal to the convection heat transfer rate into the sides of the cylindrical element. This can be represented in differential form (Equation 2.11):

$$\frac{dq_{cond}}{dx} A_c \delta x = q_{conv} dA_s \tag{2.11}$$

Further substitution of Fourier's Law (Equation 2.9) and Newton's Law of Cooling (Equation 2.10) for the conduction and convection heat fluxes gives (Equation 2.12):

$$kA_c \frac{d^2T}{dx^2} = hP(T - T_f) \tag{2.12}$$

Equation 2.12 is a second-order ordinary differential equation (ODE) with temperature cylinder body temperature as the solution variable. This ODE represents a simplified form of the temperature distribution for a classical 1-D conducting pin fin with convection (Incropera (2007)); historically has been the foundation for low-order conduction error models. Two boundary conditions (BCs) are required to solve this ODE. The first BC sets the fin temperature at the base equal to the mount temperature (i.e. $T(x = 0) = T_b$). The second BC must be applied at the fin tip. Given an adiabatic tip boundary condition (i.e. $dT(x = L)/dx = 0$), one finds the temperature solution at x=L to be (Equation 2.13):

$$T(x = L) = T_j = T_f + \frac{T_b - T_f}{\cosh\left(L\sqrt{\frac{4h}{kd}}\right)} \tag{2.13}$$

The temperature solution presented in Equation 2.13 was used by Moffat (1962) to model sensor conduction error in bare wire thermocouples. A bare wire thermocouple is comprised of

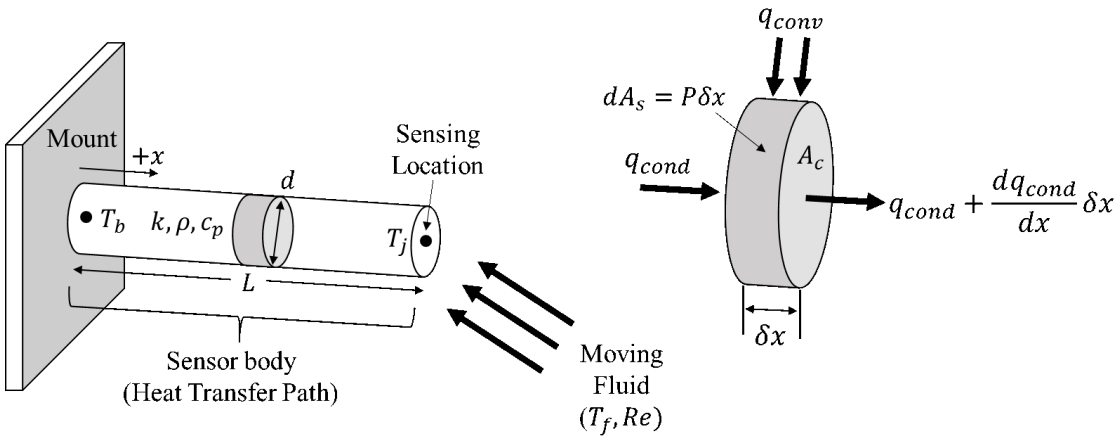

Figure 2.9: Energy balance on a differential element of a long, slender circular cylinder indicative of a fluid immersed temperature sensor mounted to a body with known temperature.

two wires of dissimilar materials in series, with the measurement location being at their junction. In most configurations, the wires are the same length and the non-junction ends of the wires are fixed to a mount of similar temperature. The use of the adiabatic tip boundary condition for a bare wire thermocouple is based on the assumption that the relative impact of the convection heat transfer at the sensor tip is small compared to the convection heat transfer along the sides of the sensor due to the tip's smaller surface area.

For a sheathed-type thermocouple, the cylindrical fin analogy can also be used. Unlike a bare wire thermocouple where the conduction heat transfer at the junction is assumed to be zero, forced convection is possible on the sensor tip, thus modifying the tip boundary condition (Equation 2.14):

$$-k\frac{dT(x=L)}{dx} = h(T - T_f) \tag{2.14}$$

The new sensor junction temperature solution, accounting for tip convection now becomes (Equation 2.15):

$$T(x=L) = T_j = T_f + \frac{T_b - T_f}{\cosh\left(L\sqrt{\frac{4h}{kd}}\right) + \frac{h_{tip}}{k}\sqrt{\frac{kd}{4h}}\sinh\left(L\sqrt{\frac{4h}{kd}}\right)} \tag{2.15}$$

Inspection of the bare wire and sheathed sensor conduction models (Equations 2.13 and 2.15, respectively) reveals that conduction errors can be decreased by increasing sensor length, decreas-

ing sensor diameter, decreasing sensor thermal conductivity, increasing the convective heat transfer to the sensor, and/or decreasing the temperature difference between the fluid and mount. Sensor length and diameter are simple changes that can heavily impact probe conduction performance. These geometric modifications are constrained by structural/durability requirements, as longer, more slender probes tend to have shorter lifetimes. Thermal conductivity is simply a function of the sensor materials, therefore sensor material selection is critical for controlling conduction error. The convective heat transfer rate scales with the square root of the velocity, thus increasing the flow velocity around the sensor is expected to decrease conduction error. Of course, conduction error can be eliminated if there is no temperature difference between the sensor base and the measured fluid, since conduction acts through temperature gradients. In idealized cases, the mount temperature can be directly controlled to achieve $T_b = T_f$ (Guenette et al. (1989); Wood (1959)). However, due to similar heat transfer phenomenon governing the sensor temperature, the mount temperature naturally deviates from the fluid temperature. This can sometimes be difficult to quantify, but for accurate conduction error predictions, knowledge of the sensor base temperature is critical (Albertson and Bauserman Jr. (1993)). For highly specialized applications involving extreme temperatures, various probe components must be deliberately cooled in order to improve probe durability, resulting in large discrepancies between sensor base and fluid temperatures (Anderson et al. (2008); Moeller et al. (2012)). Figure 2.10 shows a water-cooled, total temperature rake design used by Moeller et al. (2012) for the measurement of the exhaust of an afterburning jet engine with maximum total temperatures of 1900K (2960°F). These extreme cooling cases further necessitate the accurate knowledge of convective heat transfer coefficients, thermal conductivity, and sensor geometry for improved conduction error predictions using the available conduction error models.

2.2.3 Radiation Error

Radiation error for temperature probes is defined as the sensor-indicated temperature deviation from true total temperature, resulting from radiation heat transfer between the sensor and its surroundings. All objects with non-zero temperature emit Radiation. The magnitude of the radiation emitted is a function of several factors. Of these factors, object temperature and material emissivity are of high importance. Emissivity, ε, is defined as an object's propensity to radiate energy as thermal heat, and it quantitatively assumes a non-dimensional value between zero and unity, with zero indicating no heat emission and unity being a perfect emitter. A body with an emissivity of unity is called a "black body", since a body with an ideal black surface is expected to emit the maximum

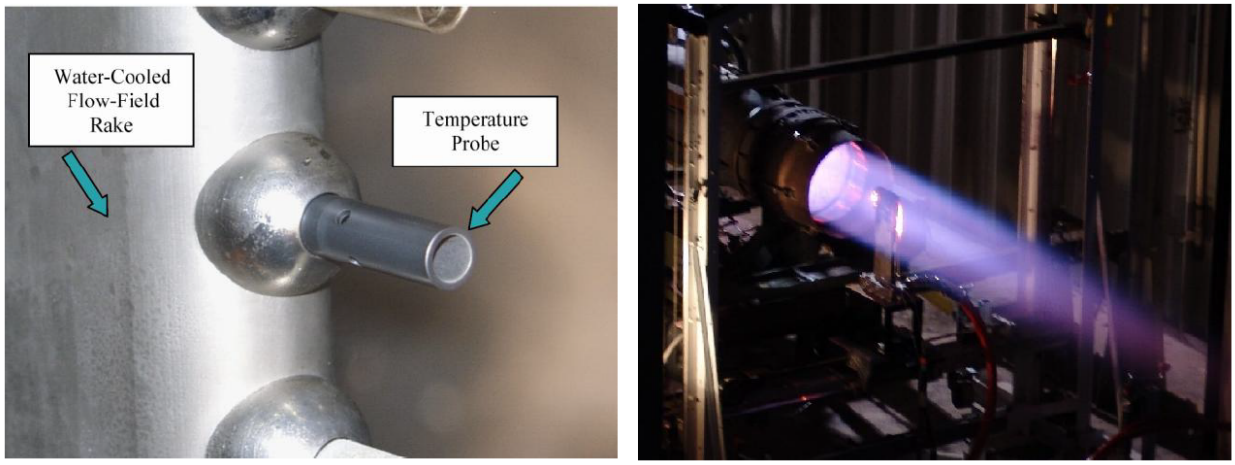

Figure 2.10: Water-cooled, carbide total temperature probe designed for total temperature measurements of the exhaust temperature of an afterburning jet engine (Moeller et al. (2012)).

thermal energy via radiation for its given temperature. The emitted thermal power per unit area of a black body is defined by the Stefan-Boltzmann law as (Equation 2.16)(Incropera (2007)):

$$E_b = \sigma T^4 \tag{2.16}$$

where $\sigma = 5.67 \times 10^{-8}\, Wm^{-2}K^{-4}$, a constant and T is the body temperature in absolute units. This law states that as an object increases in temperature, it emits more thermal radiation. Important to note is that temperature is raised to the fourth power, thus radiation energy exponentially increases with increased temperature, revealing that radiation error will be more significant to address at higher temperatures. All real bodies have an emissivity less than unity, and the emissivity can be used to directly scale the black body emissions to get the true emitted power (Equation 2.17) (Incropera (2007)):

$$E = \varepsilon \sigma T^4 \tag{2.17}$$

A second property of an ideal black body emitter is that the surface is diffuse, meaning that energy is uniformly radiated away from the surface in all directions, and this greatly simplifies thermal analyses involving radiation. In order for radiation to exchange between two surfaces, the surfaces must be in a direct line of sight since radiated energy travels in straight paths. Radiation "view factors" are used to define the ability of one surface to 'see' another, and they physically

represent the ratio of energy radiated from one surface that reaches another. Consider the two differential surfaces shown in Fig. 10. The ratio of energy radiated from surface dA_1 that reaches dA_2 is (Equation 2.18) (derived from Incropera (2007)):

$$dF_{dA_1-dA_2} = \frac{\cos\theta_1 \cos\theta_2}{\pi S^2} dA_2 \tag{2.18}$$

This view factor is given in differential form, representing the view factor between differential surface elements. In order to calculate the total heat transferred between finite surfaces, one must compute the finite area view factors given by the following double area integral (Equation 2.19)(Incropera (2007)):

$$F_{1-2} = \frac{1}{A_1} \int_{A_1} \int_{A_2} \frac{\cos\theta_1 \cos\theta_2}{\pi S^2} dA_1 dA_2 \tag{2.19}$$

It follows then that the thermal power radiated from surface 1 that reaches surface 2 is equal to (Equation 2.20):

$$q_{1-2} = A_1 F_{1-2} \varepsilon_1 \sigma T_1^4 \tag{2.20}$$

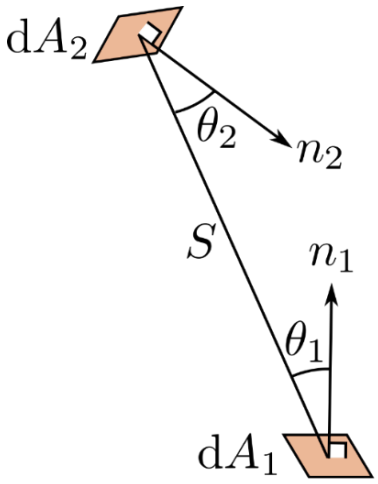

Figure 2.11: Definition of parameters necessary for the determination of the differential view factor between differential surfaces dA_1 and dA_2.

Once the energy from surface 1 reaches surface 2, multiple possibilities can occur. The energy can be reflected, absorbed, or transmitted. In this work, we are primarily concerned with

the absorbed energy. Similarly to an object's emissive potential represented by its emissivity, an object also has a propensity to absorb radiative energy, which is represented by its absorptivity, α. Physically, the absorptivity is the portion of the incoming radiation energy (irradiation) that is absorbed by the object, thus taking on a non-dimensional value between zero and unity. The final property of a black body is that its absorptivity is unity. For a so-called "gray body", the emissivity and absorptivity are equal and not required to be unity, making it more general than a black body, but that requires more consideration of the radiating surface properties.

Creating a radiative energy balance between two black body surfaces in an enclosed configuration using the Stefan-Boltzmann law gives results in an expression for the net radiative power that leaves surface 1 due to its interaction with surface 2 (Equation 2.21):

$$q_{12} = q_{1-2} - q_{2-1} = A_1 F_{1-2} \sigma (T_1^4 - T_2^4) \tag{2.21}$$

For a gray body, this equation becomes slightly more complex as the non-unity emissivity and variable radiating surface areas must be considered. Allowing for gray body radiation and generalizing to N surfaces forming an enclosure, the net radiative power expected to leave surface 1 due to interaction with all other surfaces in an enclosure can be written (Equation 2.22) (derived from Incropera (2007)):

$$q_1 = \sum_{j=1}^{N} \frac{\sigma (T_1^4 - T_j^4)}{\frac{1-\varepsilon_1}{\varepsilon_1 A_1} + \frac{1}{F_{1-j} A_1} + \frac{1-\varepsilon_j}{\varepsilon_j A_j}} \tag{2.22}$$

For the specific case of a small convex object in a large cavity, as is common for a small thermocouple sensor in a large shield, the surface of the large cavity behaves as though it were a black body, independently of the cavity's emissivity (Incropera (2007)). This fact can be used to greatly simplify the net radiation between two gray, diffuse surfaces, allowing Equation 2.21 to be scaled by the emissivity of the small convex object (Equation 2.23):

$$q_{12} = q_{1-2} - q_{2-1} = \varepsilon A_1 F_{1-2} \sigma (T_1^4 - T_2^4) \tag{2.23}$$

Consider now that surface 1 is represented by a temperature sensor at temperature T_j and surface 2 is represented by the surrounding environment at temperature T_{surr}. Assuming conduction errors are negligible, one may assume the fin to be at a uniform temperature T_j, requiring the mount

temperature equal T_j. With conduction effects eliminated, the steady state energy balance requires that the rate of convection into the sensor must equal the rate of radiation heat transfer out of the sensor to a large surrounding (Equation 2.24):

$$hA_s(T_f - T_j) = \varepsilon A_s F_{j-surr}\sigma(T_j^4 - T_{surr}^4) \tag{2.24}$$

Solving Equation 2.24 for the flow temperature based on sensor indicated temperature yields:

$$T_f = T_j + \frac{\sigma\varepsilon F_{j-surr}}{h}(T_j^4 - T_{surr}^4) \tag{2.25}$$

Moffat (1962) used Equation 2.25 to define sensor error due to radiation Δ_r with the sensor surroundings in the absence of conduction, however slightly generalized to account for the possibility of different surface areas due to convection and radiation, A_{conv} and A_{rad}, respectively (Equation 2.26):

$$\Delta_r = T_t - T_j = \frac{\sigma\varepsilon F_{j-surr}A_{rad}}{hA_{conv}}(T_j^4 - T_{surr}^4) \tag{2.26}$$

Per Equation 2.26, one can expect to decrease radiation error by lowering the sensor emissivity, increasing fluid convection, or increasing surrounding temperature towards T_t. Sensor emissivity can be lowered by using a sensor with a highly reflective surface finish, however the positive effects of such surfaces will likely be degraded due to surface tarnish and oxidation (Dahl and Fiock (1949); King (1943)). Convection heat transfer is increased by simply increasing the velocity of the flow around the sensor, however this may lead to undesirable velocity error effects if velocities become large. The last radiation error mitigation technique involves increasing the surrounding temperatures towards T_t. In most applications, it is highly impractical to change the wall temperatures of the device containing the flow. Radiation shielding is a common technique used to achieve closer agreement between the sensor and its surrounding temperatures. Excluding any conduction or convection heat transfer, the amount of heat radiated from the sensor to the surroundings is expected to be reduced by a factor of to $1/(n+1)$, where n is the number of radiation shields (assuming the sensor and all shields have equal emissivity) (Incropera (2007); King (1943)). If convection effects are included, the radiation error is expected to further decrease since the shield temperatures will be brought even closer to T_t (Moffat (1962)).

While radiation shields significantly reduce errors due to radiation, they do not eliminate it.

In most shielded probe configurations, the temperature sensor is capable of seeing both the shield area and the surrounding surfaces as is illustrated in Figure 2.12 (Bontrager (1969)). While it is possible to compute a view factor for each the sensor-to-shield and sensor-to-wall for simplified probe geometries, this may not be practical for more complex designs. This difficulty led some researchers to estimate radiation errors using models based on experimentally obtained radiation coefficients with each probe requiring its own coefficient. Glawe et al. (1956) used an empirically based radiation correction model (Equation 2.27) to estimate K^*_{rad} for a wide variety of shielded and unshielded probe configurations.

$$\Delta_r = \frac{K^*_{rad}}{\sqrt{M_p}} \left(\frac{T_j}{1000} \right)^{-0.18} \left[\left(\frac{T_j}{1000} \right)^4 - \left(\frac{T_{surr}}{1000} \right)^4 \right] \tag{2.27}$$

where M is the flow Mach number, p is flow static pressure in atmospheres, and all temperatures are in Rankine. This modeling technique is advantageous if K^*_{rad} is available for a given probe design, since it only requires knowledge of surrounding temperatures aside from flow Mach number and pressure. However, this technique is not practical for the estimation of radiation error for new probe designs, since K^*_{rad} must first be determined experimentally for each proposed design.

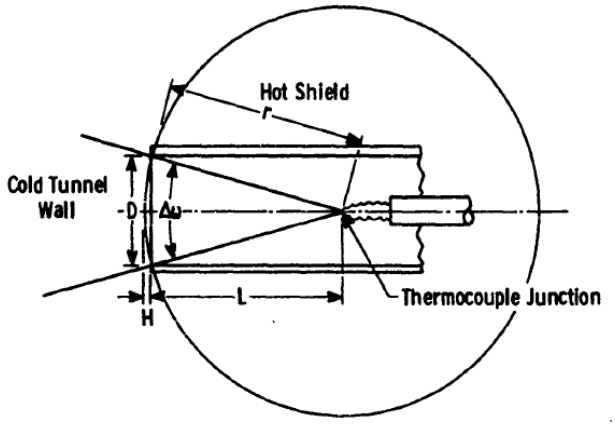

Figure 2.12: A thermocouple junction's view of the radiation shield and surrounding tunnel walls for a typical shielded probe (Bontrager (1969)).

2.2.4 Transient Error

In a real system, the temperature of the fluid being measured may be changing with time. If a sensor is able to instantaneously detect the current conditions of a time dependent flow, it would be

said to have a transient error of zero. However, any sensing element with finite mass will always lag behind a change in flow temperature. For a temperature sensor such as a thermocouple, this lag is caused by its thermal inertia, which is a function of its mass and specific heat capacity.

Neglecting conduction and radiation heat transfer, a small temperature sensor can be treated as a 'lumped' body with a uniform temperature T_j. Consider a 'lumped' mass with volume V, density ρ, and specific heat c_p as shown in Figure 2.13. The mass is initially at a temperature T_i before being immersed in a flow with temperature T_f that differs from T_i. The flow imparts a convective heat transfer over the entire surface area A_s. The resulting energy balance on the body gives (Equation 2.28):

$$\rho V c_p \frac{dT_j}{dt} = hA_s\big(T_f(t) - T_j(t)\big) \tag{2.28}$$

The solution for the time dependent temperature $T_j(t)$ with $T_j(t=0) = T_i$ as the initial condition is (Equation 2.29):

$$T_j(t) = T_f + (T_i - T_f)e^{-t/\tau} \tag{2.29}$$

where τ is the thermal time constant and equals:

$$\tau = \frac{\rho V c_p}{hA_s} \tag{2.30}$$

By rearranging Equation 2.30 and setting $t = \tau$, one gets:

$$\frac{T_j(t) - T_i}{T_f - T_i} = 0.632 \tag{2.31}$$

Equation 2.31 shows the time constant is equal to the time the body takes to cover 63.2% of the temperature difference between the initial body temperature and the free stream fluid temperature. It is this time constant that is commonly used to report the response time of a thermocouple sensor to a changing flow temperature. Transient error is defined (Equation 2.32) (Moffat (1962)):

$$\Delta_t = T_t - T_j = \tau \frac{dT_j}{dt} \tag{2.32}$$

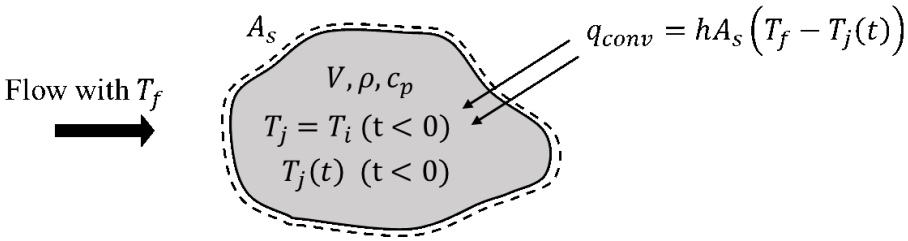

Figure 2.13: Lumped thermal mass subjected to an instantaneous change in flow temperature resulting in a time dependent temperature driven by convection heat transfer on its surface.

To decrease transient error, one must aim to minimize the time constant. By inspection of Equation 2.30, one can expect to decrease the time constant by decreasing the overall mass of the sensor ($m = \rho V$), decreasing the specific heat of the sensor material, or increasing fluid convection heat transfer. Scadron and Warshasky (1952) outlined the derivation of the time constant for bare wire sensors with various complicating factors including radiation heat transfer, convection heat transfer, wires of different diameters, and wires with different thermal properties. However, these are significantly more complex, and most experiments involving time constant determination attempt to eliminate these effects. While the time constant is used to describe the expected transient errors, it can also be used to experimentally infer convective heat transfer coefficients. This procedure will be explained below in more detail.

2.3 Quantification of Convection Heat Transfer Coefficient

The quantification of convection heat transfer is critical for the accurate estimation of conduction and radiation errors impacting total temperature probe performance. Convection heat transfer, unlike radiation and conduction, results from the interaction of the working fluid and probe solid surfaces. Thus, the nature of the flow surrounding the sensor is directly responsible for scaling the convection heat transfer, and this flow behavior is primarily driven by the probe design and free stream operating conditions. Historically, there have been many efforts dedicated to quantifying the expected convection heat transfer as a function of sensor size and flow condition. Early efforts relied heavily on experimental techniques with limited applicability outside the configurations tested. More recently, the use of computational techniques have further aided analysis of total temperature probe performance, providing a surge in the level of detailed information available to designers. In this chapter, both experimental and computational convection heat transfer quantification techniques and available results is summarized.

2.3.1 Experimental Techniques

Due to the small physical size of most common temperature sensors, experimental techniques for the determination of sensor local convective heat transfer coefficient is limited. An early, but common method developed to "measure" the film coefficients of small, bare-wire thermocouples was the time-constant technique. This technique relates the thermal time-constant to the heat transfer coefficient via simplified heat transfer relations and is mathematically analogous to the example from the "Transient Error" section above.

In the time-constant technique, the entire sensor is subjected to a steady flow with free stream temperature T_f, developing a uniform convective heat transfer coefficient along the sensor with negligible conduction and radiation heat transfer effects. Initially, the sensor is uniformly heated internally as to maintain a steady initial temperature T_i that is different from the free stream temperature. The internal heat supply is then instantaneously turned off, and the wire temperature begins to change and approach the fluid free stream temperature. The temperature of the sensor T_j is expected to behave following Equation 2.29. The thermal time constant (Equation 2.30) can also be written (Scadron and Warshasky (1952)):

$$\tau = \frac{(d\rho c)_{sensor}}{4(Nu)k_f} \tag{2.33}$$

In Equation 2.33, one is expected to reasonably know the wire and fluid material properties leaving the Nusselt number and time constant as the only unknowns. Time constant, thus Nusselt number, is therefore easy to determine if an adequate time history of temperature is measured following a step change in thermal boundary condition using Equation 2.31.

This procedure was used by several groups for the estimation of film coefficient on bare wire sensors. Scadron and Warshasky (1952) performed this experiment for bare wire sensors aligned in crossflow with Mach number ranging from 0.1-0.9 and Reynolds numbers between 250 and 30,000, measuring time constant for each and computing Nusselt Number. Correlating the time constant derived Nusselt Number with free stream Reynolds number Re^* evaluated at total conditions revealed that heat transfer is proportional to the square root of the Reynolds number (Equation 2.34):

$$Nu = (0.479 \pm 0.002)\sqrt{Re^*}Pr^{0.3} \tag{2.34}$$

Equation 2.34 was observed to behave extremely well for Mach numbers up to 0.5, with slight deviations appearing with further increases in Mach number. Carbon et al. (1950) conducted similar time-response experiments, recording time constants for sensors with air velocities ranging from 11.1 to 124.8fps (Mach numbers approximately 0.07 and 0.36, respectively) and Reynolds numbers between 3 and 340. Instead of creating a new heat transfer correlation from measured data, they calculated a theoretical time constant based on a correlation given by McAdams (1942) (Equation 2.35):

$$Nu = 0.32 + 0.43Re^{0.52} \tag{2.35}$$

These theoretical time constants showed good agreement with measured results, supporting the correlation previously given by McAdams (1942), and comparing well with the square root of Reynolds number relationship later measured by Scadron and Warshasky (1952).

Perhaps the most definitive experimental quantification of convection heat transfer coefficients on bare wire themocouples was by Moffat (1962). Synthesizing an impressive array of experimental results for measured Nusselt Numbers for bare wire thermocouples in parallel and perpendicular alignment to the flow (see Figure 2.14), Moffat (1962) defined two separate Nusselt-Reynolds number correlations for each sensor alignment for Reynolds numbers (based on sensor diameter) from 100 to 30,000 (Equations 2.36 and 2.37):

$$Nu = (0.44 \pm 0.06)Re^{0.5} \text{ (wires perpendicular to flow)} \tag{2.36}$$

$$Nu = (0.085 \pm 0.009)Re^{0.674} \text{ (wires parallel to flow)} \tag{2.37}$$

Even today, the Moffat (1962) correlations are used for estimations of heat transfer coefficients for evaluation of total temperature probe thermal performance (Villafañe and Paniagua (2013)). In some cases, these correlations remain appropriate (i.e. for simple bare wire probes with flow directed nearly perpendicular or parallel to the sensor and sensor local flow is well known). However, these correlations become less applicable when the influence of probe geometry on sensor local flow becomes more complex. While the literature contains performance calibrations of many different total temperature probe variations, they are only useful for specific geometries in limited operating environments (for instance, see Glawe et al. (1956)). Therefore, there exists a need for a

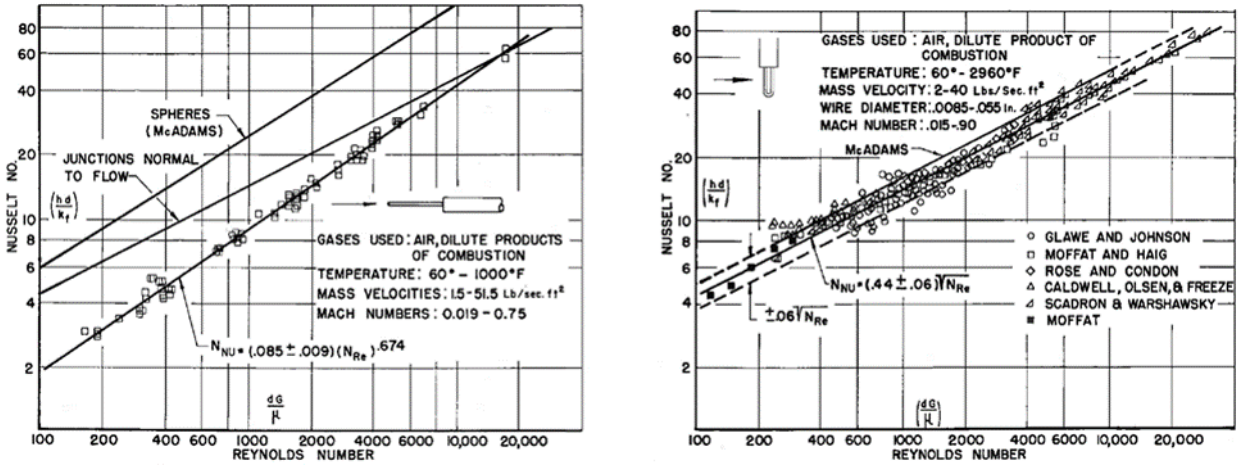

Figure 2.14: Nusselt number versus free stream Reynolds number for bare wire sensors aligned both normal (left) and parallel (right) to the flow (Moffat (1962)).

more generalized model, capable of handling a wider range of total temperature probe designs. To accomplish this, a deeper understanding of how probe geometry and operating conditions affect probe performance is necessary for development of these models. While experimental methods exist, they only provide limited information about heat transfer behavior and almost no information about flow behavior caused by the probe geometry. The next section discusses the use of Computational Fluid Dynamics to accomplish heat transfer quantification, while simultaneously benefiting from the detailed flow visualization produced with high-fidelity modeling.

2.3.2 Computational Techniques

In more recent years, improvements in computational capabilities has greatly enabled the accessibility of high-fidelity computational modeling to solve complex problems. Of particular interest is the prediction of fluid flow behavior using Computational Fluid Dynamics (CFD), which works by satisfying a system of conservation equations (mass, momentum, and/or energy) for many discretized elements that constitute the fluid domain of interest. The level of fidelity of CFD simulations is based on the type of simplifying assumptions applied to the generalized conservation equations (i.e. Reynolds-Averaged Navier-Stokes (RANS), Large Eddy Simulation (LES), Direct Numerical Simulation (DNS), etc.) and discretization (both spatial and temporal). For most practical CFD investigations, RANS computations provide a reasonable balance of detail and accuracy with computational expense. In problems where heat transfer is of importance, Conjugate Heat Transfer (CHT) techniques exist, which can directly solve for heat transfer between solid and fluid

boundaries in a given domain. The ability to simultaneously perform CFD simulations with CHT has allowed for the detailed analysis of total temperature probe performance using computational techniques, instead of relying entirely on experiments with limited insight.

Many recent research efforts successfully utilized RANS CFD/CHT for the evaluation of total temperature probes for a wide range of applications. Villafañe and Paniagua (2013) performed computations on shielded fine-wire thermocouples to optimize thermocouple wire size and composition for velocity, conduction, and transient errors. Wilson et al. (2012) used CFD/CHT computations to compare the performance of two-water cooled temperature traverse probes (inspired by Anderson et al. (2008)), successfully quantifying conduction error improvements between the original and modified designs. Zou et al. (2018) used unsteady RANS computations to provide a detailed flow and heat transfer analysis of steady thermal performance of a shielded thermocouple probe experiencing conduction, convection, and radiation heat transfer effects, as well as comparing these results quantitatively with available analytic probe performance models from the literature. Braun et al. (2017) performed simulations on bare wire thermocouples, using the computed transient response of two differently sized thermocouples to create a third virtual probe with improved temporal response. While the objectives of these studies differed, all benefitted with a more fundamental understanding of flow behavior causing the heat transfer into these different sensors because of the highly detailed solutions these CFD/CHT simulations provide.

As explained above, Moffat (1962) created an empirical set correlations based on experimental results to be used for quantification of the convection heat transfer coefficient (also known as film coefficient) over thermocouple sensor in different flow conditions. These correlations are powerful because they allow for readily estimating the film coefficient using a simple analytic model without the need for additional physical testing or computational modeling. However, these correlations are limited to the idealized arrangement of bare wires in a well behaved free-stream flow. For more practical probe designs, there is very limited information available for directly quantifying probe errors using analytic models. Furthermore, experimental capabilities for the evaluation of more complex probe designs is limited. Reardon et al. (2017) addressed this by performing a series of CFD/CHT computations on a typical vented-shield style total temperature probe (see Figure 2.15), with a sheathed thermocouple as the sensing element, over a range of flow Mach numbers (0.1-0.8), total temperatures (550-850°F) and mount temperatures (mount temperature set lower than free stream total temperature to generate significant conduction error). Detailed solutions revealed flow behavior both internal and external to the shield, as well as the distribution of convection heat transfer coefficient over the length of the sensor (see Figure 2.16). Reardon et al. (2017) further

used the results to create a new Nusselt/Reynolds number correlation to describe the heat transfer coefficient on the sensor tip (stagnation point) as a function of free stream Reynolds number (see Equation 2.38 and Figure 2.17).

$$Nu = 0.5897 Re^{0.4857} \tag{2.38}$$

This new correlation much more adequately describes the behavior of a typical vented-shield style thermocouple compared to the correlations of Moffat (1962).

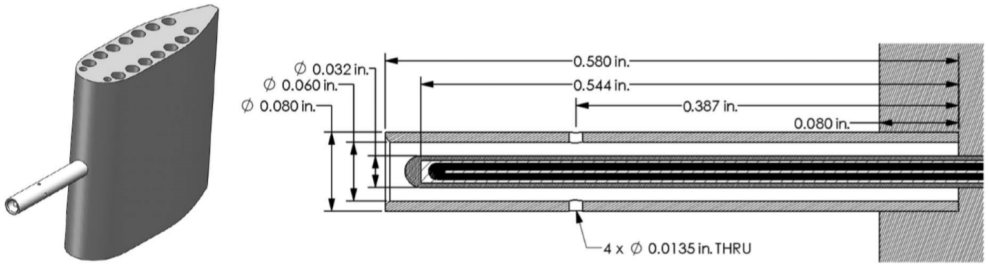

Figure 2.15: Shielded probe developed at Virginia Tech (VT) for conduction error studies (Reardon et al. (2017)). From "Computational Modeling of Total-Temperature Probes" by Reardon et al. (2017); reprinted by permission of the American Institute of Aeronautics and Astronautics, Inc.

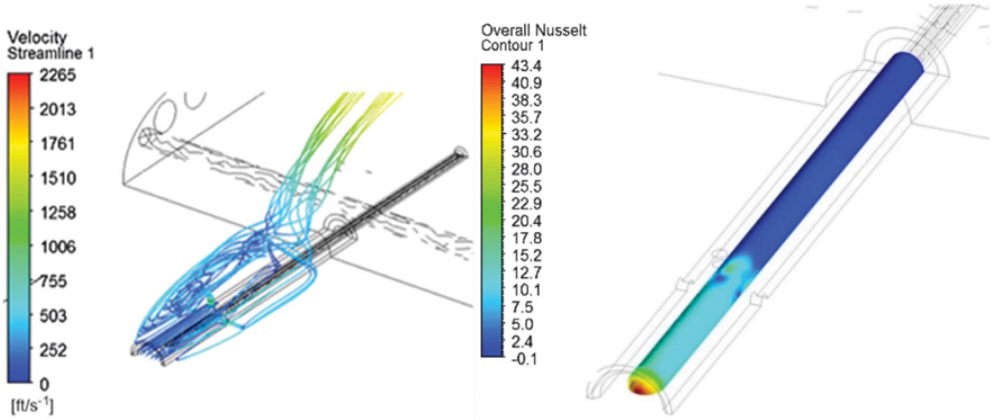

Figure 2.16: Streamlines entering and exiting shield of the VT probe, showing vortical flow outside of shield (left). Example Nusselt number contour on thermocouple sheath of the VT probe (right) (Reardon et al. (2017)). From "Computational Modeling of Total-Temperature Probes" by Reardon et al. (2017); reprinted by permission of the American Institute of Aeronautics and Astronautics, Inc.

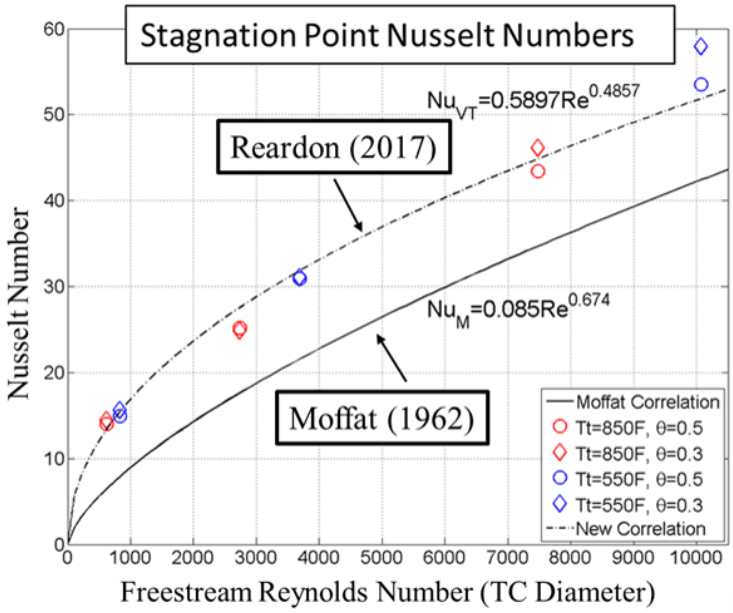

Figure 2.17: Nusselt number versus Free stream Reynolds number at the tip of a sensor inside a typical strut-mounted vented-shield style total temperature probe (Reardon et al. (2017)). From "Computational Modeling of Total-Temperature Probes" by Reardon et al. (2017); reprinted by permission of the American Institute of Aeronautics and Astronautics, Inc.

Summary

This chapter began with a historical perspective of total temperature probe development, pointing out how probe designs have evolved resulting from years of measurement experience in various applications to account for common sources of measurement error using this technique. These error sources were then explained in more detail, providing relevant error models and known mitigation techniques available from the literature. Of necessity for accurate estimation of conduction, radiation and transient error is the convection heat transfer coefficient on the sensor surface. The final section of this chapter presented techniques for both experimentally and computationally estimating this film coefficient, suggesting that the computational approach provides many benefits over experimentation.

Nomenclature

α	Absorbtivity
Δ_r	Radiation error
Δ_t	Transient Error
γ	Ratio of specific heats
ρ	Density
σ	Stefan-Boltzmann constant ($5.67 \times 10^{-8}\, Wm^{-2}K^{-4}$)
τ	Time constant
θ	View angle between differential surface elements
ε	Emissivity
A_c	Cross-section area
A_s	Surface area
c_p	Specific heat capacity at contant pressure
d	Diameter
E	Emitted thermal power
E_b	Emitted thermal power per unit area of a black body
F	Radiation view factor
h	Convective heat transfer (film) coefficient
h_s	Static enthalpy
h_t	Total enthalpy
h_{side}	Convective heat transfer (film) coefficient along side of sensor

h_{tip} Convective heat transfer (film) coefficient at tip of sensor

k Thermal conductivity of sensor

k_f Thermal conductivity of fluid

K^*_{rad} Radiation correction factor (Glawe et al. (1956))

L Length

M Mach number

m Mass

Nu Nusselt number

P Perimeter

p Pressure

Pr Prandtl number

q_{cond} Conduction heat transfer

q_{conv} Convection heat transfer

r Sensor temperature recovery factor

Re^* Reynolds number evaluated at total conditions

T Temperature

T_b Temperature at sensor base

T_f Temperature of fluid

T_j Sensor indicated junction temperature

T_s Static temperature

T_t Total or stagnation temperature

T_{aw} Adiabatic wall temperature

V Velocity

x Position

1-D One-dimensional

CFD Computational fluid dynamics

CHT Conjugate heat transfer

DNS Direct numerical simulation

EGT Exhaust gas temperature

LES Large eddy simulation

ODE Ordinary differential equation

RANS Reynolds-Averaged Navier-Stokes

RTD Resistance temperature detector

TC Thermocouple

References

C. W. Albertson and W. A. Bauserman Jr. Total temperature probes for high-temperature hypersonic boundary-layer measurements. 1993.

S. J. Anderson, K. S. Chaha, and A. J. W. Wilson. Design, development and testing of an in-engine radial traverse system for the trent engine. In *ASME Turbo Expo 2008: Power for Land, Sea, and Air*, pages 215–223. American Society of Mechanical Engineers, 2008.

C. Batho. The Temperature Gradient in De Laval Stream-Nozzles. *Min. Proc. Instn. Civ. Engrs. 174*, page 317, 1908.

C. Bentz, W. Platz, and J. Batka. *Development of a Turbine Inlet Temperature Sensor*. American Institute of Aeronautics and Astronautics, 1969.

P. J. Bontrager. Development of thermocouple-type total temperature probes in the hypersonic flow regime. Technical report, Arnold Engineering Development Center Arnold AFB TN, 1969.

J. Braun, S. Lu, and G. Paniagua. Development of high frequency virtual thermocouples. In *ASME Turbo Expo 2017: Turbomachinery Technical Conference and Exposition*, pages V006T05A026–V006T05A026. American Society of Mechanical Engineers, 2017.

M. W. Carbon, H. Kutsch, and G. A. Hawkins. *The response of thermocouples to rapid gas-temperature changes*. American Society of Mechanical Engineers, 1950.

A. Dahl and E. Fiock. Shielded thermocouples for gas turbines. *Trans. ASME*, 71(2):153, 1949.

H. Emmons and J. Brainerd. Temperature Effects in a Laminar Compressible-Fluid Boundary Layer Along a Flat Plate. In *Trans. ASME, vol. 63*, pages A105–A110, 1941.

A. Franz. Pressure and temperature measurement in supercharger investigations. 1940.

A. M. Gaylord, W. Compton, and R. Furgurson. High temperature sensors for gas turbines. In *ASME 1969 Gas Turbine Conference and Products Show*, pages V001T01A030–V001T01A030. American Society of Mechanical Engineers, 1969.

G. E. Glawe, F. S. Simmons, and T. M. Stickney. Radiation and recovery corrections and time constants of several chromel-alumel thermocouple probes in high-temperature, high-velocity gas streams. 1956.

G. Guenette, A. Epstein, and E. Ito. Turbine aerodynamic performance measurements in short duration facilities. In *25th Joint Propulsion Conference*, page 2690, 1989.

H. Hottel and A. Kalitinsky. Temperature measurements in high-velocity air streams. *JOURNAL OF APPLIED MECHANICS-TRANSACTIONS OF THE ASME*, 12(1):A25–A31, 1945.

F. Incropera. *Fundamentals of heat and mass transfer*. Number v. 1 in Fundamentals of Heat and Mass Transfer. John Wiley, 2007. ISBN 9780471457282. URL `https://books.google.com/books?id=_P9QAAAAMAAJ`.

W. King. Measurement of high temperatures in high-velocity gas streams. *Trans. ASME*, 65(5): 421, 1943.

W. Lindsey. Calibration of three temperature probes and a pressure probe at high speeds. 1942.

W. McAdams. Heat transmission. *McGraw-Hill Book Co., New York*, 214, 1942.

T. Moeller, R. Rhodes, G. Beitel, and M. May. Prediction and experimental measurement of total temperature in an afterburning turbojet exhaust. In *50th AIAA Aerospace Sciences Meeting including the New Horizons Forum and Aerospace Exposition*, page 811, 2012.

R. J. Moffat. Gas temperature measurement. *Temperature, its measurement and control in science and industry*, 2:553–571, 1962.

F. Müller. Die Ermittlung des Temperaturverlaufes von schnellströmenden Gasen und Dämpfen bei Expansion in einer Laval-Düse. *Z. ges. Turbinenwes. 17*, page 61, 1920.

W. Nusselt. Die Entropie Vermehrung in der Gasmaschine durch die nicht umkehrbare Ausführung der Verbrennung. *Z. ges. Turbinenwes. 13*, page 172, 1916.

E. Pohlhausen. Wärme. *ZAMM - Journal of Applied Mathematics and Mechanics / Zeitschrift für Angewandte Mathematik und Mechanik*, 1(5):410–412, 1921. doi: 10.1002/zamm.19210010506. URL `https://onlinelibrary.wiley.com/doi/abs/10.1002/zamm.19210010506`.

J. Reardon, J. A. Schetz, and K. T. Lowe. Computational modeling of total-temperature probes. *Journal of Thermophysics and Heat Transfer*, 31(3):609–620, 2017.

M. D. Scadron and I. Warshasky. Experimental determination of time constants and nusselt numbers for bare-wire thermocouples in high-velocity air streams and analytic approximation of conduction and radiation errors. 1952.

J. A. Schetz and R. D. W. Bowersox. *Boundary layer analysis*. American Institute of Aeronautics and Astronautics, 2011.

F. S. Simmons. Recovery corrections for butt-welded, straight-wire thermocouples in high-velocity, high-temperature gas streams. 1954.

A. Stodola. Flow of Gases and Vapours Through Tubes of Variable Section. *Z. VDI 47*, pages 1787–1788, 1903.

L. Villafañe and G. Paniagua. Aero-thermal analysis of shielded fine wire thermocouple probes. *International Journal of Thermal Sciences*, 65:214–223, 2013.

A. Von Moll, A. R. Behbahani, G. C. Fralick, J. D. Wrbanek, and G. W. Hunter. A review of exhaust gas temperature sensing techniques for modern turbine engine controls. In *50th AIAA/ASME/SAE/ASEE Joint Propulsion Conference*, page 3977, 2014.

A. J. W. Wilson, P. T. Ireland, R. Stevenson, S. J. Thorpe, and D. Martin. A robust radial traverse temperature probe for application to a gas turbine hp/ip stage. In *ASME Turbo Expo 2012: Turbine Technical Conference and Exposition*, pages 63–71. American Society of Mechanical Engineers, 2012.

W. Wimmer. Stagnation temperature recording. *National Advisory Committee for Aeronautics – Technical Memorandums*, 1941.

E. M. Winkler. Stagnation temperature probes for use at high supersonic speeds and elevated temperatures. Technical report, NAVAL ORDNANCE LAB WHITE OAK MD, 1954.

R. D. Wood. An experimental investigation of hypersonic stagnation temperature problems. 1959.

www.netl.doe.gov. Advanced Turbines. `https://www.netl.doe.gov/sites/default/files/2017-11/Program-108.pdf`, 2019. Accessed: 3/20/2019.

Z. Zou, W. Yang, W. Zhang, X. Wang, and J. Zhao. Numerical modeling of steady state errors for shielded thermocouples based on conjugate heat transfer analysis. *International Journal of Heat and Mass Transfer*, 119:624–639, 2018.

3. Aerodynamic Analysis of Total Temperature Probe Thermal Performance using Conjugate Heat Transfer

The contents of this chapter have been accepted in the *Journal of Thermophysics and Heat Transfer* (Tyler G. Vincent, Joseph A. Schetz, and K. Todd Lowe. “Aerodynamic Analysis of Total Temperature Probe Thermal Performance using Conjugate Heat Transfer”).

Significant portions were previously discussed in Eric Nicholas Rolfe. “Impact of Total Temperature Probe Geometry on Sensor Flow and Heat Transfer,” MS Thesis, 2017.

Aerodynamic Analysis of Total Temperature Probe Thermal Performance Using Conjugate Heat Transfer

Tyler G. Vincent,* Eric N. Rolfe,† Kevin T. Lowe,‡ and Joseph A. Schetz§
Virginia Polytechnic Institute and State University, Blacksburg, Virginia 24061

DOI: 10.2514/1.T5635

Understanding the behavior and design of total temperature probes used in gas turbine engines and other hot high-speed flows remains an active area of work, given the demands set by extreme operating conditions and ever-decreasing sensor size requirements. Where probe strut/mount cooling is necessary for probe survivability, conduction effects can be significant. The most effective mitigation of conduction errors results from convective heat transfer over the sensor. The goal of this paper is to provide a deeper understanding of the flow physics responsible for establishing the convective heat transfer on the sensor surface of vented-shield total temperature probes. This was accomplished by using high-fidelity computational fluid dynamics with conjugate heat transfer to examine the details of the aerodynamic environment establishing the heat transfer on the sensor surface. Probe geometric parameters varied and include the axial vent location, sensor diameter, and shield outer diameter. These parameters are cast into a set of nondimensional parameters that are used to build a set of correlations for local Reynolds numbers over regions of the sensor and Stanton number correlations for film coefficients. These film coefficients can be directly used in the new and existing low-order analytic thermal conduction probe performance models presented here and in the literature.

Nomenclature

A_{hyd}	=	flow area bounded by inner diameter of the shield and thermocouple sheath diameter
A_{inlet}	=	inlet area of the shield
A_{vent}	=	net area of the vent holes
D_{shield}	=	shield outer diameter
D^*_{shield}	=	normalized shield diameter; $D_{\text{shield}}/t_{\text{strut}}$
d_{shield}	=	shield inner diameter
d_{TC}	=	sheath diameter of the thermocouple sensor
d^*_{TC}	=	normalized sheath diameter; $d_{\text{TC}}/d_{\text{shield}}$
h	=	convective film coefficient
h_{rear}	=	sensor rear average convective film coefficient (downstream of vents)
h_{side}	=	sensor side average convective film coefficient (upstream of vents)
h_{tip}	=	sensor tip average convective film coefficient
k_{eff}	=	effective thermal conductivity
L_{shield}	=	length of the shield
$\dot{m}$	=	actual mass flow through the shield
$\dot{m}_{\text{ideal}}$	=	idealized mass flow through shield
$\dot{m}/\dot{m}_{\text{ideal}}$	=	sensor mass flow ratio
p	=	flow pressure
Re	=	Reynolds number
Re_{ideal}	=	ideal Reynolds number inside the shield
Re_{local}	=	local Reynolds number inside the shield
T	=	temperature
t_{strut}	=	maximum thickness of strut
u	=	velocity
x_{vent}	=	distance from tip of probe to vent hole
x^*_{vent}	=	normalized vent location; $x_{\text{vent}}/L_{\text{shield}}$
θ	=	driving temperature potential for conduction; $(T_t - T_b)/T_t$
μ	=	fluid viscosity
ρ	=	fluid density

Subscripts

ave	=	average
b	=	sensor base location
j	=	sensor junction/tip location
s	=	static conditions
T	=	total conditions
0	=	parameter for nominal baseline sensor
∞	=	freestream condition

Received 18 September 2018; revision received 13 January 2019; accepted for publication 13 March 2019

*Doctoral Candidate, Department of Mechanical Engineering.
†Graduate Research Assistant, Kevin T. Crofton Department of Aerospace and Ocean Engineering.
‡Associate Professor, Kevin T. Crofton Department of Aerospace and Ocean Engineering. Associate Fellow.
§Holder of the Durham Chair, Kevin T. Crofton Department of Aerospace and Ocean Engineering. Lifetime Fellow AIAA.

I. Introduction

THE measurement of temperature in hot high-speed gases is important in many engineering applications. Such measurements can be used to understand loss mechanisms and determine the efficiency in turbomachinery applications [1–4]. Absolute temperatures within an engine also impact the structural integrity of exposed engine components [5,6].

Because temperature measurements of hot gases are required in many engineering applications, total temperature sensors are used in a wide range of environments, from low-temperature low subsonic flows up through high-temperature high-Mach-number flows. In standard practice, a well-designed total temperature sensor aims to record a temperature as close to the true total temperature of the flow as possible [7–10]. However, there are "errors" that will cause the recorded temperature to deviate from the true total temperature. These errors come from multiple sources: 1) aerodynamic errors from nonideal diffusion of the oncoming flow, 2) conduction errors from heat transfer along the sensor to the mount, 3) radiation errors, and 4) transient errors. Thus, the design of each sensor needs to be tailored for its specified use [11]. This requires a fundamental understanding of the sources of error and how sensor geometry/configuration can be used to create an environment for mitigating anticipated errors. See Fig. 1 for a schematic of the typical vented-shield probe design considered in this paper. In this configuration, the sensor is externally mounted to the leading edge (LE) of a streamlined strut/support with the sensor junction, which is responsible for the probe indicated temperature and located upstream and normal to the strut leading edge at a distance equal to the sensor length L_{TC}. The sensor base temperature T_b, can be controlled by cooling the probe strut/support,

leading to conduction heat transfer within the sensor in the direction from the sensor junction to the base. The magnitude of this conduction error is governed by the forced convection heat transfer into the sensor due to fluid movement around the sensor. The addition of a vented shield provides several advantages. First, the shield mitigates radiation heat transfer in conditions in which the surrounding environment temperatures are significantly different from the sensor temperatures by eliminating the direct line of sight between the sensor and surroundings. Second, the shield acts as a stagnation tube, significantly reducing the velocity of the oncoming fluid and bringing the fluid closer to total temperature conditions. Third, a well-designed shield has been shown to significantly reduce probe thermal performance sensitivity to oncoming flow incidence angles as compared to unshielded probes [12].

This paper will focus specifically on probes with significant conduction errors resulting from cooling the probe strut/rake body. Furthermore, it is assumed that radiation errors are well mitigated by the shield and have a negligible impact on the overall heat transfer for the Cases studied in this paper [13]. In the absence of radiation, heat transfer from the fluid to the sensor via forced convection is combined with conduction within the sensor to establish the sensor indicated temperature. Most current probes employ a thermocouple (TC) as the sensor, and this work deals with such designs. But, much of what we present here applies to other sensors, such as those based on fiber optics. Probe aerodynamics plays an important role in establishing the amount of convection heat transfer acting over the TC sensor surface, especially over the TC surfaces upstream of the shield vents. Past correlations [7] showed that the equivalent average Nusselt number over an unshielded thermocouple sensor is primarily a function of the freestream flow Reynolds number and Mach number. In contrast to the unshielded tests reported by Moffatt, the use of a vented shield (or stagnation tube) around a thermocouple sensor diffuses the flow to create local sensor Mach and Reynolds numbers. Intuitively, it is this local sensor Reynolds number that drives the magnitude of the convective heat transfer encountered by the sensor, and not the freestream. By understanding how geometry affects the flow local to the sensor inside a vented shield, we can better quantify the effect of geometric modifications on sensor thermal performance. In the past, this knowledge was gained experimentally, and sensor performance was related back to freestream conditions. Most of these experiments were conducted as parametric studies in which thermal performance was measured using the TC sensor indicated temperature for probes of various geometries in multiple flow conditions. Although this method of experimentation was useful to quantify the impact of probe variations on the sensor indicated temperature, it lacks the ability to directly relate performance to probe aerodynamics.

Although experimental flow visualization and quantification techniques exist, attaining high-resolution flowfield information around a TC sensor is difficult, especially as the sensors become smaller or are contained within a shield. Thus, it has become more common to use high-fidelity computational fluid dynamics (CFD) Reynolds-averaged Navier–Stokes (RANS) modeling techniques to the analyze performances of such small sensors. Previous research at the Virginia Polytechnic Institute and State University (Virginia Tech) conducted by Schneider [14] and Reardon et al. [13] leveraged numerical simulations and experimental validation tests to gain a deeper physical understanding of the aerodynamic features influencing the thermal performance of a nominal vented-shield-style total temperature probe over various flow conditions [13,14]. These studies were critical because they effectively developed a validated procedure for the evaluation of total temperature probes using CFD modeling, including conjugate heat transfer (CHT).

Before work conducted at Virginia Tech, Villafañe and Paniagua [15] used CFD/CHT techniques to assess both steady and transient response of shielded fine-wire thermocouples with different wire and junction bead diameters, stressing the advantages of computations for evaluation of sensor errors over experiments. Later, Braun et al. [16] effectively used unsteady RANS simulations with CHT to quantify the simultaneous transient thermal response of two different-sized bare-wire thermocouples with base conduction in a strong crossflow for the prediction of an enhanced temporal response expected from a third smaller virtual probe. Zou et al. [17] used unsteady RANS computations to provide a detailed analysis of steady thermal performance of a shielded thermocouple probe experiencing conduction, convection, and radiation heat transfer effects. Each of these works illustrated how numerical modeling of total temperature sensors allows for a superior description of the physics-governing probe performance as compared to current experimental techniques.

The primary goal of this paper is to better explain how sensor geometry impacts the flow aerodynamics governing the heat transfer to the sensor. The second goal is to present a new set of correlations providing a quantitative description of the impact that geometry has on the sensor local convective heat transfer to the sensor. These developed correlations allow for a rapid estimation of the heat transfer that exists on the sensor upstream of the vents, which is vital to quantifying thermal performance with conduction effects resulting from base cooling.

II. Conduction Errors

There has been a great deal of work in understanding the basic physics of errors in total temperature probes. One of the most influential works in this area was produced by Moffat [7]. Moffat characterized and quantified the main sources of error in unshielded total temperature probes (with a simple correction for shielded sensors) and identified design considerations to mitigate these errors. In his discussion on conduction error, Moffat modeled the TC sensor as a cooling fin, subject to convective heat transfer along the surface of the TC. The solution of the one-dimensional heat conduction equation with convection is a two-point boundary value problem, requiring knowledge of either the temperature or the heat transfer conditions at both the base and the tip of the fin. Additionally, one must know the convective heat transfer coefficient h, along the surface of the TC and the effective thermal conductivity of the TC materials k_{eff}. For most real total temperature probe assemblies, a temperature measurement is made at or near the base of the TC sensor, thus providing the base temperature boundary condition, denoted as T_b in Fig. 1. Because the tip/junction temperature T_j, of the fin/TC is the output of the model, the tip boundary condition is commonly defined by the expected tip heat flux. Moffat enforced an adiabatic tip boundary condition in his conduction model given by Eq. (1), having assumed a small relative importance of the tip heat flux as compared to the heat flux along the TC length:

$$T_j = T_t - \frac{T_t - T_b}{\cosh(L\sqrt{(4h/k_{\text{eff}}d_{\text{wire}})})} \tag{1}$$

For closure of this conduction model, Moffat provided a Nusselt number correlation for flow parallel to the axis of the bare TC wires

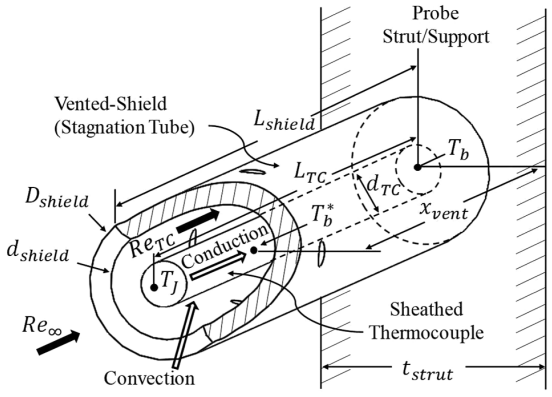

Fig. 1 Components of representative shielded T_t probe, labeled flow parameters, significant known temperature locations, and heat transfer paths.

based on the freestream Reynolds number to estimate the film coefficient h, over the TC surface [7]:

$$Nu_{\text{Moffat}} = \frac{hd}{k_f} = 0.085Re^{0.674} \tag{2}$$

where d is the junction bead diameter.

A shortcoming of Moffat's model for application to vented-shield sensors is the assumption of a probe averaged, uniformly distributed Nusselt number along the entire sensor [7]. It has been more recently shown that the TC surface heat transfer in a vented-shield-style probe is best divided into three regions: tip, side, and rear, as depicted in Fig. 2 [13]. The impingement of the flow ingested by the shield on the TC tip surface governs the enhance heat transfer experienced by the tip region. The acceleration of flow around the tip and passing over the side of the TC sensor establishes the side heat transfer region. The length of the side region is dictated by the vent location. Past results have shown that a surface averaged film coefficient is a good approximation in this region due to a nearly uniform film coefficient distribution upstream of the vents [13]. Due to the discharge of shield internal flow through the vents, fluid downstream of the vents is essentially stagnant. Although reduced heat transfer does exist in this region, its behavior is beyond the scope of this paper.

Two modifications to Moffat's conduction model can be made to account for the multiple sensor regions [7]. The first modification relaxes the adiabatic tip assumption. As observed in previous studies, the tip heat transfer coefficient is approximately three to five times that of the side ($h_{\text{tip}}/h_{\text{side}} \approx 3$–$5$) [13], which can have a significant impact on the model-predicted junction temperature. Allowing for tip heat transfer produces the following probe conduction model, based again on a one-dimensional conducting pin fin with convection:

$$T_j = T_t - \frac{T_t - T_b}{\cosh(L\sqrt{(4h_{\text{side}}/k_{\text{eff}}d_{\text{TC}})}) + h_{\text{tip}}\sqrt{(d_{\text{TC}}/4h_{\text{side}}k_{\text{eff}})}\sinh(L\sqrt{(4h_{\text{side}}/k_{\text{eff}}d_{\text{TC}})})} \tag{3}$$

The more generalized tip heat transfer is included by the addition of the second term in the denominator. However, this model still assumes that h_{side} is applied over the entire sensor length when, in reality, it should only affect the side region upstream of the vents. Thus, the second necessary modification is to split the influence of the side and rear heat transfer coefficients. This is possible by creating a "stacked" conducting fin model based on two separate fins labeled as 1 and 2 in Fig. 2. Fin 1 comprises the rear portion of the TC with length x_{vent}, and fin 2 comprises the rest of the TC upstream of the vents with length L_{side}. The stacked solution is created by equating the conduction heat transfer rates into the tip of fin 1 and out of the base of fin 2. The resulting conduction model shown in Eq. (4) more adequately describes the influence of the multiple sensor regions expected in a typical vented-shield-style probe:

$$T_j = T_t - \frac{T_t - T_b^*}{\cosh(L_{\text{side}}m_2) + (h_{\text{tip}}/m_2k_{\text{eff}})\sinh(L_{\text{side}}m_2)} \tag{4}$$

where an intermediate determination of the fin interface temperature T_b^*, is necessary using Eqs. (5a) and (5b):

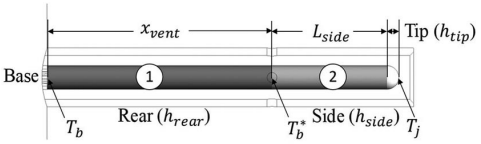

Fig. 2 Identification of TC sheath tip, side, and rear regions for typical vented-shield-style probes.

$$T_b^* = T_t + \frac{(T_b - T_t)m_1(\cosh(m_1x_{\text{vent}})/\tanh(m_1x_{\text{vent}})) - \sinh(m_1x_{\text{vent}})}{(m_1/\tanh(m_1x_{\text{vent}})) + \gamma} \tag{5a}$$

$$\gamma = m_2\frac{\sinh(m_2L_{\text{side}}) + (h_{\text{tip}}/m_2k_{\text{eff}})\cosh(m_2L_{\text{side}})}{\cosh(m_2L_{\text{side}}) + (h_{\text{tip}}/m_2k_{\text{eff}})\sinh(m_2L_{\text{side}})} \tag{5b}$$

and m_1 and m_2 are fin model coefficients defined as follows:

$$m_1 = \sqrt{\frac{4h_{\text{rear}}}{k_{\text{eff}}d_{\text{TC}}}} \tag{5c}$$

$$m_2 = \sqrt{\frac{4h_{\text{side}}}{k_{\text{eff}}d_{\text{TC}}}} \tag{5d}$$

To use any of the available fin-based thermal conduction models presented here or in previous works, one must have a good understanding of how to quantify the heat transfer coefficients along the entire surface of the TC sheath. For this paper, we conducted an extensive CFD/CHT analysis on vented-shield-style probes of varying probe geometries to understand the flow physics governing the convective heat transfer over the tip and sides of the TC, upstream of the vent holes. The results of the analysis were synthesized to create new correlations for the rapid evaluation of h_{tip} and h_{side}, requiring only a priori knowledge of the freestream flow conditions and probe geometry. For problems further considering radiation effects, these new convective heat transfer correlations can be used together with the methods of Refs. [18,19] to yield precise predictions of thermal performance.

III. Sensor Flow Analysis

Historically, empirically based models have correlated the sensor heat transfer coefficient directly to freestream conditions for use in low-order analytic conduction models. These models tend to perform well for the single probe geometry used to generate the model, but they are generally unable to estimate the impact of significant geometric variations on thermal performance. Consider a typical vented-shield probe. The probe is designed so that the shield and strut/rake body diffuse the oncoming freestream flow, establishing a more ideal flow internal to the shield around the sensor. Because this local flow is what will dictate the heat transfer coefficient along the sensor, the empirical models should be based on the sensor local flow, and not the freestream flow. Thus, for a model to appropriately include geometric effects, one must first consider how probe geometry will impact the local flow over the sensor.

In this section, a new method is introduced providing the framework for relating sensor local flow to freestream flow via key geometric parameters. This is accomplished by the quantification of a mass flow ratio defined by the actual mass flow rate internal to the shield and normalized by a reference, idealized mass flow rate, which assumes no viscous losses. This mass flow ratio is heavily driven by both sensor geometry and freestream conditions. Next, this sensor mass flow ratio can be directly used to deduce the local Reynolds number based on knowledge of the freestream flow conditions. This local Reynolds number can then be used with empirical models relating local flow to sensor convective heat transfer coefficients.

The first step is to identify an appropriate reference, ideal mass flow internal to the shield. Imagine a TC sensor aligned axially to

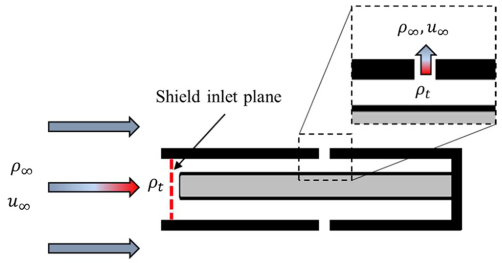

Fig. 3 Schematic of ideal flow conditions governing the reference, ideal mass flow rate through the shield inlet plane.

the flow and placed inside a surrounding shield with the inlet perpendicular to the flow and downstream vents allowing for captured fluid to exit as illustrated in Fig. 3. In the idealized case, viscous effects are ignored. Without viscous effects, the flow will experience no losses. This idealization includes flow both internal and external to the shield. Allowing the flow to isentropically expand from total conditions inside the vents to freestream conditions at the vent discharge [20], the ideal mass flow rate simplifies to Eq. (6) based on total vent discharge area A_{vent}:

$$\dot{m}_{\text{ideal}} = \rho_\infty u_\infty A_{\text{vent}} \tag{6}$$

High-fidelity CHT/CFD simulations were used to give an accurate quantitative measure of the actual mass flow rate $\dot{m}$, internal to the sensor. This mass flow rate, together with the ideal mass flow rate, forms the sensor mass flow ratio parameter $\dot{m}/\dot{m}_{\text{ideal}}$. We chose to quantify the mass flow rate as a performance parameter for a shielded design due to the ability to quickly deduce the Reynolds number using the mass flux:

$$Re = \frac{(\rho u)_{\text{ave}} d_{\text{TC}}}{\mu} = \frac{\dot{m} d_{\text{TC}}}{A\mu} \tag{7}$$

where A is the characteristic flow area. Because $\dot{m} \equiv (\rho u)_{\text{ave}} A$, the mass flux for a given mass flow rate is set by the flow area. Using $A = A_{\text{hyd}}$ (where A_{hyd} is the hydraulic area bounded by the inside of the shield and the TC sheath) gives a Reynolds number based on the mass flux around the TC length, allowing for a better calculation of h_{side}. Using $A = A_{\text{in}}$ (where A_{in} is the shield inlet area) gives a Reynolds number based on the mass flux experienced at the TC tip, allowing for a better calculation of h_{tip}. Furthermore, viscosity is evaluated as a function of total temperature due to the low Mach number of the flow within the vented shield.

Creating an equivalent expression for a reference, ideal Reynolds number (also calculated based on freestream flow conditions) and forming a ratio with the true local Reynolds number Re, and simplifying, we get Eq. (8):

$$\frac{Re}{Re_{\text{ideal}}} = \frac{(\dot{m} d_{\text{TC}}/A_{\text{hyd}}\mu)}{(\dot{m}_{\text{ideal}} d_{\text{TC}}/A_{\text{hyd}}\mu)} = \frac{\dot{m}}{\dot{m}_{\text{ideal}}} \tag{8}$$

Further rearranging Eq. (8) gives Eq. (9):

$$Re = Re_{\text{ideal}} \frac{\dot{m}}{\dot{m}_{\text{ideal}}} \tag{9}$$

This is a powerful relationship that allows the local Reynolds number over the sensor to be calculated, given the sensor mass flow ratio and knowledge of the freestream conditions. The next step is predicting the sensor mass flow ratio based on a few key geometric parameters.

Although there are many geometric parameters that influence the sensor mass flow parameter, three nondimensional geometric parameters were chosen here to cover most of the major effects (dimensions are labeled in Fig. 1):

1) Normalized vent location:

$$x^*_{\text{vent}} = x_{\text{vent}}/L_{\text{shield}}$$

2) Normalized sheath diameter:

$$d^*_{\text{TC}} = d_{\text{TC}}/d_{\text{shield}}$$

3) Normalized shield diameter:

$$D^*_{\text{shield}} = D_{\text{shield}}/t_{\text{strut}}$$

The normalized vent location x^*_{vent}, captures the adverse pressure gradient created by the presence of the strut support. It is expected that, as the vent location moves closer to the strut leading edge (x^*_{vent} decreases), the vent discharge pressure will increase, thus decreasing $\dot{m}/\dot{m}_{\text{ideal}}$ and the local Reynolds number Re. The normalized sheath diameter d^*_{TC}, governs the hydraulic area for flow internal to the sensor. Smaller d^*_{TC} ideally (assuming no viscous losses) increases the velocity in the sensor due to decreased A_{hyd} resulting in an increase in the local Reynolds number Re, helping to increase h_{side}. However, there is expected to be a point where further decreasing d^*_{TC} will result in a viscous boundary-layer-dominated internal flow, reducing the $\dot{m}/\dot{m}_{\text{ideal}}$ and local Reynolds number Re, and effectively reducing probe performance. Finally, the normalized shield diameter D^*_{shield}, is expected to reduce the impact of the strut adverse pressure gradient near the vent discharge by moving the vents closer to a freestream dominated flow region.

IV. CFD/CHT Procedures

In the previous section, the local Reynolds number is calculated based on the freestream conditions and the sensor mass flow ratio. Due to the complexity of the shielded sensor geometry on flow aerodynamics in and around the shield, determination of the internal mass flow can be difficult. By use of an experimentally validated high-fidelity CFD/CHT method, simulations can be readily setup, run, and postprocessed to obtain detailed information about the flow, including the shield internal flow rate $\dot{m}$, and heat transfer coefficients along the TC sensor, h_{side} and h_{tip}. In this section, the parameter space for strut-mounted vented-shield sensors is defined based on the key geometric parameters. The CFD/CHT methodology is introduced, and specifics of the computational domain are discussed. Validation of the current method for predicting the performance of vented probes against experimental data has been reported previously for conduction, velocity, and radiation errors [13]. The reader is referred to that work for more details.

A. Defining the Geometric Parameter Space

To achieve the desired level of understanding for this work, the effects of each geometric parameter identified should be studied independently. Recall, the main parameters of interest are the normalized vent location x^*_{vent}), the normalized sheath diameter d^*_{TC}), and the normalized shield diameter D^*_{shield}). It is understood that the effects of these parameters on performance are not entirely independent; however, each parameter is hypothesized to have a dominant effect on a specific region of the flow around the sensor, and these effects can be combined to make predictions about probes with multiple varying geometric parameters.

The parameter space generated is centered around a nominal sensor design given by $x^*_{\text{vent}} = 0.614$, $d^*_{\text{TC}} = 0.538$, $D^*_{\text{shield}} = 0.286$, and $A_{\text{vent}}/A_{\text{inlet}} = 0.206$. As illustrated in Fig. 4 and tabulated in Table 1, changes in sensor geometry were made by nearly independent variations of the three dimensional parameters (x_{vent}, d_{TC}, and d_{shield}) relative to this nominal design while holding L_{shield} and t_{strut} constant.

Resulting from the desire to keep the parameter space indicative of reasonable sensor designs, true independence was not achieved. This is a result of the shield inner diameter and outer diameter being related via the relation $D_{\text{shield}} = d_{\text{shield}} + 2t_{\text{shield}}$, where t_{shield} is the shield wall thickness. Although d_{shield} and D_{shield} can be independent

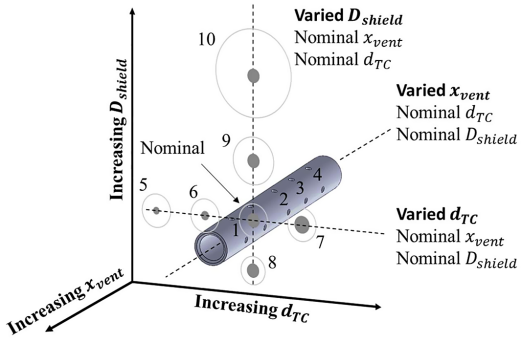

Fig. 4 Parameter space used for the key geometry parameters (case numbers labeled).

parameters, the only way to independently vary them is to change shield thickness. Because we wish to have a large variation in D_{shield}, it was unreasonable to keep d_{shield} constant due to the large shield tube thickness that would be required. Therefore, shield thickness was kept a constant for all computed designs. This decision to hold shield thickness constant resulted in both d^*_{TC} and D^*_{shield} varying when the shield diameter was changed. However, it will be shown later that this is acceptable due to d^*_{TC} largely governing the shield internal flow and D^*_{shield} governing the shield external flow. In all, the design space consisted of five vent locations (cases 1–4), four TC diameters (cases 5–7), and five shield diameters (cases 8–11), with the nominal case being shared between all geometric parameters.

Not studied in this design space was the impact of the vent discharge area. It is well understood that, by increasing the vent diameter, the mass flow rate $\dot{m}$) will increase into the shield. However the ideal mass flow rate $\dot{m}_{\text{ideal}}$ is also a function of vent area; thus, the mass flow ratio ($\dot{m}/\dot{m}_{\text{ideal}}$) is hypothesized to be insensitive to reasonable variations in the vent area. For this study, the vent discharge to shield inlet area ratio was held constant for all cases. This was chosen because the ideal flow velocity inside the shield will match between two designs of similar $A_{\text{vent}}/A_{\text{inlet}}$ based on the ideal mass flow rate calculation described previously. Furthermore, the impact of the TC recessed distance (distance junction is recessed relative to shield inlet) was not studied; thus, the shield to TC length ratio ($L_{\text{shield}}/L_{\text{TC}}$) was held constant by holding L_{TC} constant.

B. Conjugate Heat Transfer Approach

Conjugate heat transfer computations allow for the simultaneous evaluation of the flow solution and heat transfer phenomenon between interacting fluid and solid material domains. ANSYS Fluent [21] was the chosen code for this study. The two quantifiable objectives of performing the CHT/CFD simulations are to first determine the actual mass flow rate internal to the shield for each design and, second, to determine the average tip and side heat transfer coefficients, h_{tip} and h_{sheath}, respectively. Qualitative investigation of the resulting flow behavior is used to help build a physical understanding of the influence geometry has on probe performance.

Table 1 Geometric parameter space

Case	x^*_{vent}	d^*_{TC}	D^*_{shield}
Nominal	0.614	0.538	0.286
1	0.806	0.538	0.286
2	0.376	0.538	0.286
3	0.2	0.538	0.286
4	0.029	0.538	0.286
5	0.614	0.252	0.286
6	0.614	0.336	0.286
7	0.614	0.672	0.286
8	0.614	0.667	0.245
9	0.614	0.342	0.407
10	0.614	0.25	0.53
11	0.614	0.167	0.759

The solutions presented in this paper are based on a steady Reynolds-averaged Navier–Stokes formulation of the flow equations solved using a density-based solver, which is well suited for compressible flows. The conjugate heat transfer requirement is achieved by equating the heat transfer between adjacent solid and fluid domains at the interface; thus, the heat transfer out of the fluid is entirely absorbed by the solid. Radiation was not considered in these computations due to its small impact at these modest flow temperatures considered and inclusion of a shield designed to mitigate radiation effects [13].

For the cases performed in this study, the shear-stress transport (SST) $k-\varepsilon$ model was used, given the blended $k-\omega/k-\varepsilon$ formulation with optimized performance for near-wall ($k-\omega$) and free shear flows ($k-\varepsilon$). The flow around the sensor/mounting strut configuration contains both separated free shear layers and attached boundary layers with strong adverse pressure gradients, motivating the use of this model [22]. We have obtained good comparisons with experiments using this method [13]. One shortcoming of turbulent viscosity-based models is in their difficulty to handle flows with significant mean streamline curvature, strong swirling, or stress-induced secondary flows in ducts: all of which are expected features of the flow around the blunt shield and flow discharge from the shield vents. It has been shown that Reynolds-stress models can more accurately capture these effects, however, with an expected increase in computational expense due to directly solving the Reynolds-stress transport and dissipation rate equations [21,22]. Calculations with these two turbulence "closure" models were performed on the nominal sensor case, and the comparison shows that the difference is not significant enough to justify use of the more expensive Reynolds-stress model over the versatile SST $k-\omega$ model.

Lastly, an unsteady RANS (URANS) simulation with the SST $k-\omega$ model was also conducted on the nominal probe; however, no global or local instabilities were revealed, even when attempts to trigger unsteadiness via freestream flow angle perturbations were made. Because URANS turbulence models tend to have inherent numeric dissipation, often preventing global or local unsteadiness to occur, the absence of unsteadiness in this model is not conclusive. Large-eddy simulations or other resolved eddy techniques may be necessary to detect less prominent local flow instabilities, but these methods were not applied here due to practical limitations.

C. Computational Domain and Boundary Conditions

Because full three-dimensional (3-D) conjugate heat transfer solutions were desired, both solid and fluid domains were included in each model. The solid components included the TC assembly, shield, and strut/mount. The solid probe geometry was surrounded by a large fluid domain, which was sized to prevent flow communication between the probe solid boundaries and the far-field fluid boundaries. Finalized probe/fluid model assemblies were imported into ANSYS, in which unstructured meshes were created using the built-in meshing capabilities, and boundary conditions were applied. Temperature-dependent solid and fluid material properties were also considered for improved accuracy of results.

The TC comprised an outer sheath (Inconel), inner insulation/potting material (magnesium oxide), and the TC leads (chromel–alumel) modeled with perfect contact between solids, as shown in Fig. 5. Figure 5 shows a representative surface mesh of both the solid and fluid regions used for computations in this study. Hollow channels, representative of a cooled strut, were created within the strut body to allow for application of a constant temperature boundary condition (see Fig. 6). The temperature boundary condition for the cooling channel walls was set based on desired nondimensional conduction driver values [$\theta \equiv (T_t - T_b)/T_t$], where T_b is the temperature at the base of the TC, where the sensor enters the mount (see Fig. 1). The fluid domain surrounded the entirety of the probe assembly with the boundary conditions shown in Fig. 6.

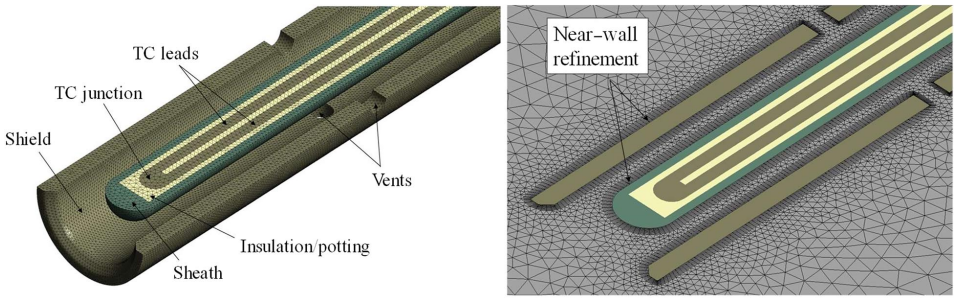

a) Solid surface mesh **b) Fluid surface mesh**

Fig. 5 Typical mesh used for current geometric study.

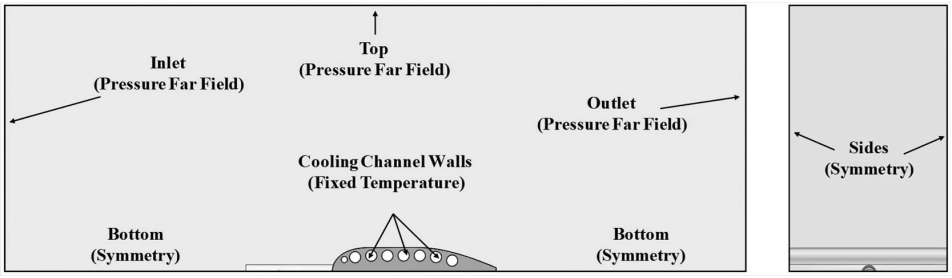

Fig. 6 Side and front view schematics of 3-D computational domain with labeled fluid and solid boundary conditions.

The fluid was modeled as ideal air with viscosity based on Sutherland's law. The use of pressure far-field boundary conditions requires the fluid domain boundaries to be placed far enough from the solid bodies to ensure near-zero gradients in the flow near the far-field boundaries. The actual fluid domain used for simulations is shown in Fig. 7. The overall flow solution was assumed to be symmetric about the strut chord plane; thus, a symmetry boundary condition was applied at the bottom of the domain to reduce computational costs. Depicted in Fig. 6 are the out-of-plane symmetry boundary conditions. Because this is a full 3-D simulation, the entire domain was given a thickness approximately equal to one strut chord length. It can be assumed that, at a large enough strut spanwise distance relative to the shield, the flow will become two-dimensional; thus, symmetry boundary conditions can be applied in the out-of-plane boundaries.

Each geometric case was run at a total temperature of 850°F (727 K) and a static pressure of 1.0 atm, which are indicative of conditions achievable in the experimental work at Virginia Tech [13]. Because the conduction error is expected to decrease at higher-speed flows due to increased forced convection, a moderate Mach number of 0.4 was chosen to accentuate conduction error effects. For a selected number of cases, two additional flow conditions were tested, including a "cold" total temperature of 70°F (294 K) at 1.0 atm and a "hot" total temperature of 2500°F (1644 K) at 10 atm: both with a Mach number of 0.4. Running these additional cases allowed for comparisons of probe performance predictions in multiple freestream Reynolds number regimes, yielding additional insights. The resulting Reynolds numbers per unit length based upon the freestream velocity and viscosity were $Re/l \approx 1.2 \times 10^7$ m^{-1}, 3×10^6 m^{-1} and 9×10^6 m^{-1} for the 2500, 850, and 70°F cases, respectively. The mounting strut temperature boundary condition for the 850°F cases was set to approximately 457°F. Due to practical limitations of further cooling the probes in the 70°F cases in an experimental facility, the mounting strut temperature was set to 17°F. Finally, the mounting strut temperature boundary condition for the 2500°F cases was set to approximately 895°F.

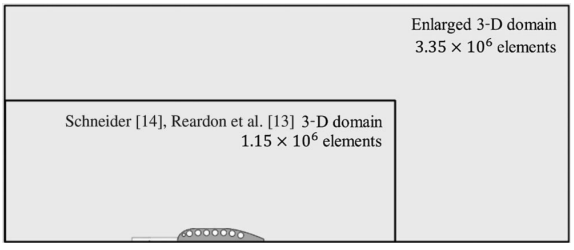

Fig. 7 Enlarged fluid domain used in current work compared to fluid domain used by Schneider [14] and Reardon et al. [13].

D. Grid and Solution Method Selections

A grid independence study was conducted using the solutions from two different grids for the nominal sensor evaluated at the hot operating condition ($T_t = 850$°F). The first grid, developed by Schneider [14] and used by Reardon et al. [13], consisted of approximately 1.15 million elements [13,14]. The second grid, used for all later results presented in this paper, features an enlarged domain with approximately 3.35 million elements. The enlargement of the second domain accounted for only a small percentage of the increased element count, with the majority of the additional elements resulting from fluid and solid surface refinement on and around the TC sensor and shield. A scaled comparison of the computational domains can be found in Fig. 7. A quantitative comparison of extracted heat transfer and probe performance quantities between the two mesh solutions can be found in Table 2. The small differences seen in the two sets of results provide confidence in the results of both simulations, supporting the use of the enlarged domain for further predictions. Of course, as the probe geometry changes between cases, the grids used between cases will also differ. As the shield diameter grew, the number of elements required to achieve similar element refinement around the TC sensor and shield also grew. Therefore, the element count for all cases tested in this paper was not constant, ranging from 2.8 to 6.0 million elements. For all simulations performed in this study, the maximum local y^+ values on the sensor surface were found to be less than 2.5, with an average y^+ over the entire sensor remaining below 1.0.

Table 2 Comparison of results using the Schneider [14]/Reardon et al. [13] domain and the enlarged domain used in the current work

Quantity	Reardon et al. [13]/ Schneider [14] mesh	Enlarged mesh	Difference, %
Element count	1,147,495	3,346,815	— —
h_{tip}, W/(m^2 · K)	1,113	1,090	2.1
h_{side}, W/(m^2 · K)	485	509	4.9
$\dot{m}/\dot{m}_{ideal}$	0.614	0.647	5.3

Table 3 Comparison of results using turbulence SST $k-\omega$ model and RSM

Quantity	SST $k-\omega$	RSM	Difference, %
h_{tip}, W/(m^2 · K)	1090	978	10.2
h_{side}, W/(m^2 · K)	509	479	5.9
$\dot{m}/\dot{m}_{ideal}$	0.647	0.634	2.00

Next, we wanted to evaluate the use of the SST $k-\omega$ turbulence model by comparing the nominal case solution to one using a Reynolds-stress model (RSM). Due to complications in achieving desired convergence using the enlarged domain mesh, another more refined mesh was used for the RSM simulation. Acceptable agreement between the SST $k-\omega$ and RSM simulations (see Table 3) shows that the SST $k-\omega$ turbulence model is adequately predicting the more complicated flows resulting from significant mean streamline curvature, strong swirling, or stress-induced secondary flows in ducts: features that the RSM does well.

V. Results

The simulation results provide the details necessary to link the sensor-local (shield-internal) flowfield to the freestream flow conditions and probe geometry, namely, TC, shield, and strut dimensions. First, the CFD/CHT solution for the nominal sensor is investigated, revealing several prominent flow features controlling the heat transfer behavior on the TC surface. Next, the CFD/CHT solutions for each of the geometric parameter space cases were analyzed, carefully identifying each parameters impact on the local TC flow relative to the nominal sensor geometry.

The CHT/CFD results are then combined to produce a physics-based empirical correlation to relate the probe geometry and operating condition to the internal mass flow rate that can be used to directly estimate the appropriate local sensor Reynolds numbers describing the flow over the TC tip and side. Finally, the data will be combined to generate a new set of local Stanton–Reynolds number correlations to determine h_{tip} and h_{side}, which are needed for rapid low-order analytic model predictions.

A. Nominal Sensor Flowfield Features

In this section, the nominal probe case will be investigated to identify the major flow features governing probe thermal performance. Immediately, one can note several significant characteristics of the flow, both internal and external to the shield, using streamlines as shown in Fig. 8. The first set of streamlines illustrates the flow behavior of the fluid ingested by the shield inlet. As expected from a well-designed shield/stagnation tube, the internal flow is well controlled and appears to be uniform and axial to the sensor. The shield internal flow is entirely discharged from the vents, preventing any significant flow over the sheath downstream from the vents near the strut. The movement of flow directly over the length of the sensor will develop a forced convection heat transfer. It is this convection heat transfer that is exploited to reduce the impact of conduction due to the reduced strut temperatures on the sensor indicated temperature. The magnitude of the convective heat transfer is known to be a function of the flow velocity and, more specifically, the sensor local Reynolds number; and, it only acts over the length of the sensor with significant flow. This length will be denoted as the sensors heated length, and it is expected to be the length of the sensor upstream of the vents. In the earlier Sensor Flow Analysis section of this paper (Sec. III), a method was created, allowing for a direct comparison of a sensor mass flow ratio to a local sensor Reynolds number ratio, based on flow information extracted from the CFD solutions and freestream flow conditions. In the ideal scenario, the mass flow ratio $\dot{m}/\dot{m}_{ideal}$ would equal 1.0, indicating the absence of any viscous losses in the entire process of flow passing over the probe. However, a quick inspection of the streamlines external to the shield reveals the presence of multiple complex, viscous, external flow features, surely expected to adversely affect the mass flow rate internal to the shield by directly altering the vent discharge condition.

An inspection of the flow Mach number, static pressure, and total pressure field contours in Fig. 9 provides a more detailed description of the specific flow features affecting probe performance. The vented shield acts as a diffuser, with flow inlet boundary conditions set by the total conditions of the approach flow at the inlet and the outlet set by the external flow static pressure at vent discharge. The static pressure contour shows that the pressure environment at the vent discharge will be significantly impacted by the vent location parameter x^*_{vent}. Increasing x^*_{vent} by moving the vents forward toward the shield inlet will place the vents in a reduced-pressure region. This low-pressure region can be attributed to flow acceleration around the shield leading edge outside the shear layer and total pressure losses due to shield leading-edge separation. The anticipated effect will be an increased $\dot{m}/\dot{m}_{ideal}$. The opposite can be expected if x^*_{vent} is decreased by moving the vents further into the strut adverse-pressure-gradient-dominated region. This adverse-pressure-gradient region can be lessened by increasing D^*_{shield}.

Internal to the shield, the sides of the sensor have convective heat transfer due to a growing (usually low Reynolds number) nearly axisymmetric boundary layer. The hemispherical front of the sheath

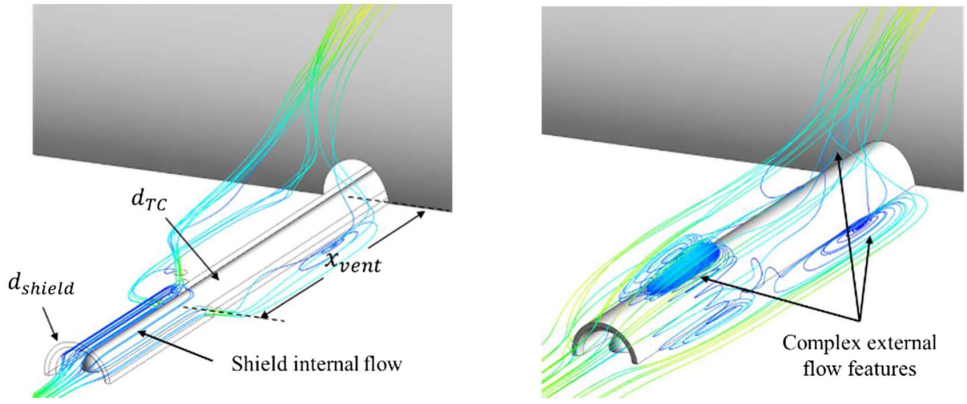

Fig. 8 Streamline visualizations of flow internal (left) and external (right) to the shield, revealing the presence of viscous flow features that directly alter the flow experienced by the sensor.

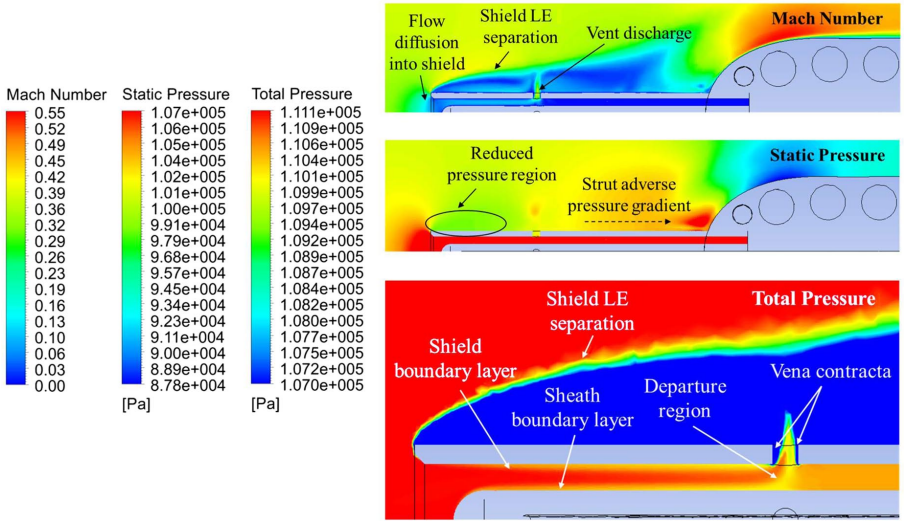

Fig. 9 Visualization of significant shield external and internal flow features for a nominal sensor using Mach number, static pressure, and total pressure contours (unclipped scale).

is subjected to an enhanced convection coefficient due to the stagnation of shield ingested flow. This coefficient has been shown to correlate with the diffused velocity approaching the sensor [13]. Near the bleed hole, the departure region separation phenomena cause more complexity in the film coefficient values, but these lead to relatively small contributions to the total heat transfer in the sensor due to the small sheath area impacted by this departure region. As flow progresses through the shield, total pressure losses occur primarily due to the boundary layers formed on the sheath and the shield internal wall. Further losses occur due to the separation mechanisms when the flow departs from the sheath and turns toward the vent holes and the vena contracta through the holes. These total pressure losses contribute to a reduction in $\dot{m}/\dot{m}_{\text{ideal}}$.

B. Impact of Normalized Vent Location x^*_{vent}

The first geometric parameter varied was the axial vent discharge location. As anticipated, moving the vent location will greatly alter the vent discharge pressure conditions, as shown in Fig. 10. The near-strut vent location ($x^*_{\text{vent}} = 0.029$) experiences a higher pressure due to the adverse-pressure-gradient region, whereas the near-shield leading-edge vent location ($x^*_{\text{vent}} = 0.806$) experiences a lower pressure due to the shield tip separation region.

Because mass flow through the shield is governed by vent discharge pressure, we expect these varied vent locations to have significantly different internal mass flow ratios, $\dot{m}/\dot{m}_{\text{ideal}}$. It will be shown later that the mass flow is less than 50% of the ideal value for the extreme case of $x_{\text{vent}}/L_{\text{shield}} = 0.029$. As may be reasoned

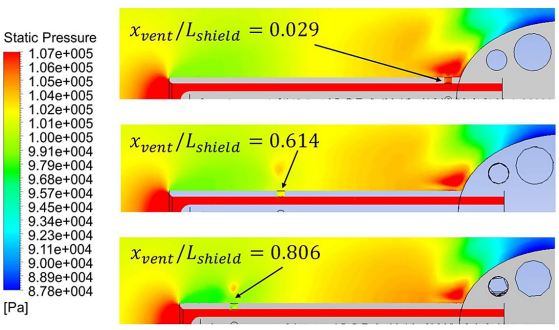

Fig. 10 Comparison of vent external pressures for various x^*_{vent} locations (static pressure contours).

from the general structure of the static pressure field in Fig. 10, there is also a region of slowly varying mass flow within the range $0.2 \leq x_{\text{vent}}/L_{\text{shield}} \leq 0.6$. Finally, the low-pressure region near the inlet of the shield leads to increased mass flow rates with the vents moved forward.

Although the increased mass flow rate through the sensor is likely to increase the forced convection coefficient over the sensor, it is important to further consider the impact of vent location on the "heated length" of the sensor. The heated length of a vented-shield total temperature probe is the length of the sheath exposed to moving flow upstream of the vents. As vent location is moved forward toward the shield leading edge, the mass flow rate is increased, resulting in a higher h_{side}, shown in Fig. 11. But, there is a tradeoff with sensor heated length and, in some cases, an optimal vent location exists to minimize conduction error effects.

C. Impact of Normalized TC Diameter d^*_{TC}

The second geometric modification of interest is a change in the nondimensional TC diameter ($d_{\text{TC}}/d_{\text{shield}}$) via changes in d_{TC} while holding d_{shield} constant. The clear motivation for changing d_{TC} from an aerodynamic perspective is to directly change the hydraulic diameter, d_{hyd}, and thus A_{hyd}, which is the area governing shield internal flow. Ideally, neglecting viscous effects, changes in A_{hyd} will directly scale shield internal flow velocity via $\dot{m} \equiv \rho V A_{\text{hyd}}$, assuming the mass flow rate is fixed based on the shield vent discharge area. Recall here, for all simulations, $A_{\text{vent}}/A_{\text{inlet}}$ was held constant to remove the vent area as a geometric parameter. Shown in Fig. 12 is a comparison of the flow behavior within the shield for varying d_{TC}, holding d_{shield} constant.

As observed in the nominal case in the bottom of Fig. 9, boundary layers form along the shield inner wall and the sheath, resulting in total pressure losses. It is evident that decreasing A_{hyd} by increasing d_{TC} results in a larger portion of the flow being dominated by both aerodynamic and thermal boundary layers, decreasing total pressure at the vent discharge inside the shield. Although the loss of total pressure will effectively reduce the mass flow ratio, this effect was observed to be small for the range of sensors investigated, with only a 3% decrease in $\dot{m}/\dot{m}_{\text{ideal}}$ when d^*_{TC} was increased from 0.252 to 0.674 (more than doubling d_{TC} inside same shield). Because the mass flow ratio does not vary much over the tested sensors with varying d_{TC}, the flow velocity along the side of the sensor is forced to increase with reduced A_{hyd} (increased d_{TC}), and thus a larger d_{TC} in a nominal shield results in a higher local Reynolds number. An upper threshold for d^*_{TC} is expected in which further increases in d_{TC} in a fixed diameter shield will result in a boundary-layer-dominated flow, significantly impacting

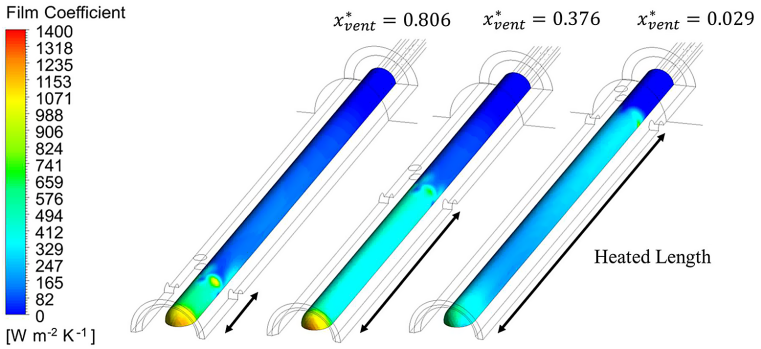

Fig. 11 Film coefficient contours versus sensor heated length tradeoff as a result of varied vent location: $x^*_{\mathrm{vent}} = 0.376$ has the highest sensor-indicated temperature.

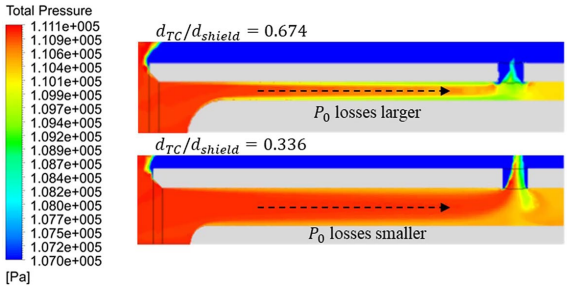

Fig. 12 Total pressure contour comparison of $d^*_{\mathrm{TC}} = 0.674$ (top) and 0.336 (bottom) showing larger losses as d^*_{TC} increases.

the total pressure and worsening performance. Keeping a hydraulic diameter-based Reynolds number, $Re_{d_{\mathrm{hyd}}}$ above 500 is recommended for avoiding this boundary-layer-dominated regime based on these results.

D. Impact of Normalized Shield Outer Diameter D^*_{shield}

As stated earlier, the design space defined did not support variation of D^*_{shield} without also altering d^*_{TC}, because shield thickness was held constant across all cases. However, the previous analysis of d^*_{TC} results suggests that this effect should have a minimal impact on $\dot{m}/\dot{m}_{\mathrm{ideal}}$; thus, any significant change in $\dot{m}/\dot{m}_{\mathrm{ideal}}$ due to changing D_{shield} should be primarily attributed to the influence of D^*_{shield} and not d^*_{TC}. This assumption is supported in Fig. 13, which shows a comparison of how $d_{\mathrm{TC}}/d_{\mathrm{shield}}$ impacts the internal flow by varying

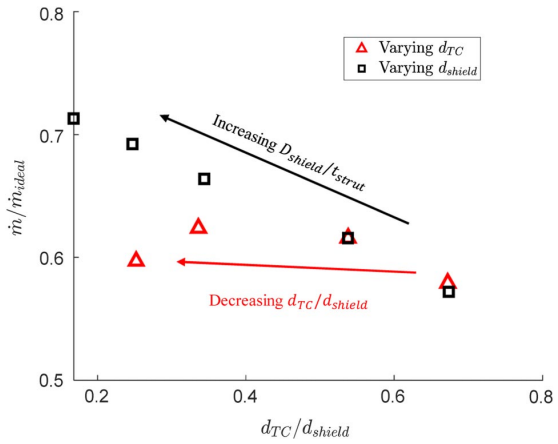

Fig. 13 Mass flow ratio for varied d_{TC} and d_{shield} plotted versus $d_{\mathrm{TC}}/d_{\mathrm{shield}}$.

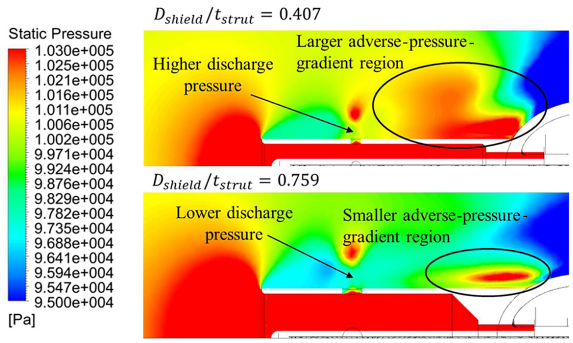

Fig. 14 Static pressure contour comparison of $D^*_{\mathrm{shield}} = 0.407$ (top) and 0.759 (bottom) showing lower discharge pressure as D^*_{shield} increases.

either d_{TC} or d_{shield}. There is a significantly larger effect of changing d_{shield} as compared to d_{TC}.

These results can be explained by splitting the influence of d_{TC} and d_{shield} (directly related to D_{shield}) on the aerodynamics of the shield internal and external flowfields, respectively. The static pressure contours in Fig. 14 show that, by raising the height of the vent above the strut mount centerline (increasing D_{shield}), the vent is moved into a location less affected by the strut adverse-pressure-gradient region. This creates a more favorable discharge environment, increasing $\dot{m}/\dot{m}_{\mathrm{ideal}}$. Therefore, the apparent strong dependence of $d_{\mathrm{TC}}/d_{\mathrm{shield}}$ on the mass flow ratio in Fig. 13 for the varying d_{shield} cases is better explained by the shield external flow effects governed by $D_{\mathrm{shield}}/t_{\mathrm{strut}}$.

E. Impact of Freestream Reynolds Number on Mass Flow Ratio

For all TC diameter and shield diameter cases, simulations performed using total temperatures of 70, 850, and 2500°F allow for a comparison of the mass flow ratios in different freestream Reynolds number conditions. Figure 15 shows the comparison of the mass flow ratio data using geometry from cases 5–11 (see Table 1) at the three flow total temperature conditions. Small variations (maximum variation less than 10%) in the mass flow rate ratio exist for each geometry; however, there is no clear trend in its behavior as flow temperatures are increased. This strongly suggests that the mass flow ratio is strongly insensitive to freestream total temperature conditions. More significantly, the mass flow ratio appears independent of the freestream Reynolds number.

F. Summary of Geometric Impacts on Mass Flow Ratio

Synthesizing all the mentioned effects due to the primary geometric parameters provides a clear description of influence each parameter has on the mass flow ratio expected for a given design (see Fig. 16).

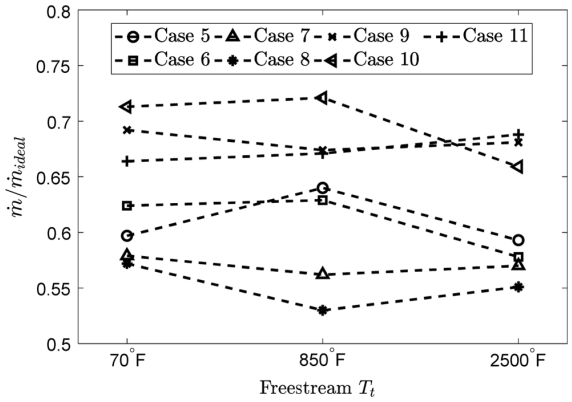

Fig. 15 Comparison of mass flow ratios at various freestream conditions.

In summary, the following hold true:

1) Varying x_{vent}/L_{shield} by changing x_{vent} directly impacts the external vent discharge environment dominated by two distinct regions: the adverse-pressure-gradient region near the strut leading edge and the reduced pressure region near the shield inlet. Increasing x_{vent} increases $\dot{m}/\dot{m}_{ideal}$.

2) Varying d_{TC}/d_{shield} by changing d_{TC} impacts the internal flow characteristics by allowing more or less of the flow passage to be dominated by boundary-layer formations on the shield inner walls and sheath. Increasing d_{TC} decreases $\dot{m}/\dot{m}_{ideal}$.

3) Varying D_{shield}/t_{strut} by changing D_{shield} impacts the external flowfield near the vent discharge by altering the influence of the strut adverse-pressure-gradient region. Increasing D_{shield} increases $\dot{m}/\dot{m}_{ideal}$.

G. Correlating Geometric Parameters on Mass Flow Ratio

Given the phenomenological understanding just discussed, a physics-motivated correlation of the nondimensional geometric design parameters can be provided. The parameters x_{vent}/L_{shield}, d_{TC}/d_{shield}, and D_{shield}/t_{strut} have been chosen for a multiple linear regression model of the following form:

$$\frac{\dot{m}}{\dot{m}_{ideal}} = \sum_{i=1}^{N_i} a_i \left(\frac{x_{vent}}{L_{shield}}\right)^i + \sum_{j=1}^{N_j} b_j \left(\frac{d_{TC}}{d_{shield}}\right)^j + \sum_{k=1}^{N_k} c_k \left(\frac{D_{shield}}{t_{strut}}\right)^k + C \tag{10}$$

where a_i, b_j, and c_k are model coefficients/slopes, and C is the model intercept. Each parameter's polynomial order in the regression model (i.e., N_i, N_j, and N_k) was determined by visual inspection of the mass flow ratio responses due to each geometric parameter. From Fig. 16, both d_{TC}/d_{shield} and D_{shield}/t_{strut} each appear to be well described by a linear first-order model. To accurately capture the inflection point visible in the x_{vent}/L_{shield} between 0.2 and 0.6, a minimum of a third-order polynomial is required. Regression model coefficients were determined using a least-squares approach [23]. Inserting model coefficients, we arrive at an expression for the mass flow ratio as a function of freestream flow conditions and the nondimensional geometric parameters:

$$\frac{\dot{m}}{\dot{m}_{ideal}} = 2.41\left(\frac{x_{vent}}{L_{shield}}\right) - 4.62\left(\frac{x_{vent}}{L_{shield}}\right)^2 + 3.02\left(\frac{x_{vent}}{L_{shield}}\right)^3 - 0.09\left(\frac{d_{TC}}{d_{shield}}\right) + 0.21\left(\frac{D_{shield}}{t_{strut}}\right) + 0.15 \pm 0.037 \tag{11}$$

A comparison of this multiple linear regression model with the CFD evaluated points (see Fig. 16) shows the model well captures the

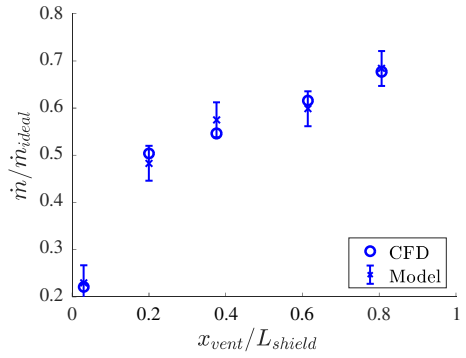

a) Varied vent position x_{vent}

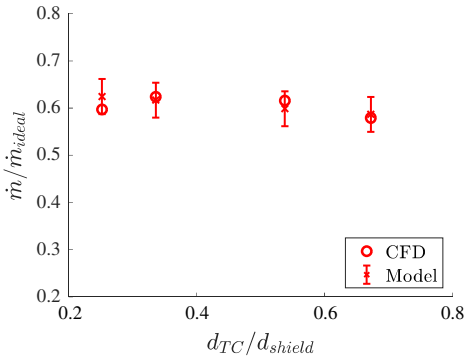

b) Varied TC sheath diameter d_{TC}

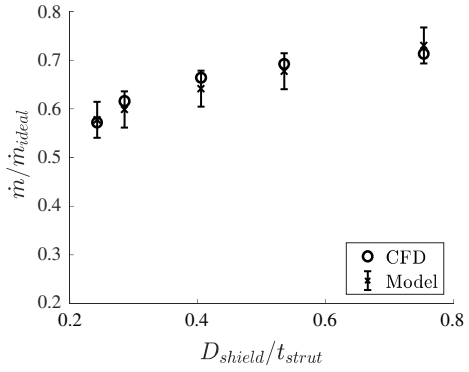

c) Varied shield outer diameter D_{shield}

Fig. 16 Mass flow ratio dependence on geometry in which circles show CFD results and crosses show correlation model results. All error bands represent 95% confidence interval for model fit.

influence of each parameter on the mass flow ratio. This model has a coefficient of determination R^2) value of 0.994, indicating that 99.4% of the data are explained by the model. Further included in both Fig. 16 and Eq. (11) is a 95% confidence interval of the model fit based on the spread of the data around the model. The percent differences listed in Tables 2 and 3 resulting from computational gridding and turbulence model selection can be additionally applied for an even more conservative estimate of mass flow ratio model uncertainty. We investigated additional higher-order terms; however, only marginal improvements to the model were observed, which were outweighed by the added model complexity.

H. Correlating Sensor Convective Film Coefficients with Local Reynolds Numbers

For the evaluation of total temperature sensor thermal performance with large conduction using the low-order analytic conduction model presented in Eq. (4), it is necessary to know the film coefficient values along the tip and sides of the TC sheath. It is well known that the film coefficient is highly dependent on the local flow Reynolds number. The model presented in the previous section allows one to rapidly evaluate the sensor local Reynolds number based on sensor geometry and freestream flow conditions, providing the necessary information for estimations of the film coefficients. In this section, we investigate the response of the TC surface convective heat flux on mass flow ratio data to develop an empirical correlation for the convective heat transfer coefficient.

For each computation performed, sensor sheath surface heat flux information is readily available. Due to the assumed absence of radiation, all surface heat flux from the fluid to the sheath surface is a result of convective heat transfer. The film coefficient profile along the sheath surface can be evaluated using the following:

$$h = \frac{Q''}{T_f - T_s} \tag{12}$$

where Q'' is the surface heat flux (from fluid into sheath), T_f is the local fluid temperature, and T_s is the local sheath surface temperature. Motivated by the intention of this model to be used with a priori freestream flow information, T_f is assumed equal to the freestream total temperature. This assumption will have adverse effects for limited cases in which the conjugate heat transfer of the fluid in the shield results in a significant decrease in local fluid temperature, especially as flow progresses through the shield. However, no significant loss in T_t was observed in most cases. Figure 17 shows a representative heat flux, sheath surface temperature, and resulting film coefficient distribution along the sheath of the nominal sensor at $T_t = 850$°F.

A visual inspection of these contours reveals several insights. First, as previously discussed with Fig. 11, is the heated length of the sensor due to convection, which is clearly visible in the film coefficient distribution. Second, the film coefficient is quite uniformly distributed over the heated length, despite a nonuniform heat flux profile along the same length. Third, there is an enhanced, nonuniform, film coefficient region along the domed tip of the sensor due to axial flow impingement and subsequent flow acceleration around the sensor tip. For the correlation analysis presented in this work, we will consider the area-averaged film coefficient contours over the tip and side regions of the TC sheath as depicted in Fig. 2.

Observed but not considered in this correlation analysis are the circular, high heat flux regions located near the vents, which are visible in both the heat flux and film coefficient contours. These features are a result of the flow inertial overshoot and recirculation that occur immediately before flow discharge from the four vents, which are discretely located in 90 deg circumferential increments. Despite the large heat flux values, the overall impact of these high heat flux regions on junction TC readings is minimal due to their small area of influence and remote location away from the junction. Lastly, the heat transfer coefficients focused on in this paper are based on the forced convection heat transfer into the sensor from the moving fluid passing through the vented-shield. This flow only impacts the tip and side regions of the sensor. As observed in this and past works, the flow is nearly stagnated in the rear portion of the shield. As a result, heat transfer in this region is not the result of forced convection; rather, it more closely resembles natural convection. Natural convection is heavily dependent on the fluid temperature distribution in the rear portion of the shield. Because the flow is stagnated in this region, the cooled mount has a large influence on this fluid temperature as energy is pulled away from this fluid with no way to escape the shield. Because the fluid passing over the tip and sides of the sensor is constantly moving, it is always nearly at fluid total temperature, making the convection heat transfer correlations in this region independent of mount temperature, providing a very powerful result. However, this level of generality is not immediately obvious at this time for the rear portion and remains a further topic for investigation. Table 4 lists the surface averaged film heat transfer coefficients from each case along the tip and side regions separately.

In previous work by Moffat [7] and others, the heat transfer correlation used to determine the heat transfer over a thermocouple was based on a correlation of the Nusselt number on the Reynolds number (Re–Nu). Here, a Re–Nu correlation was again considered, but the Stanton number St), which includes a mass flux term in the denominator, is more intimately connected to the hypotheses and findings of the current study, and all results will be presented in Re–St form. The Stanton number can be calculated based on a local mass flux $(\rho u)_{\text{ave}}$ and fluid specific heat capacity c_p using the following:

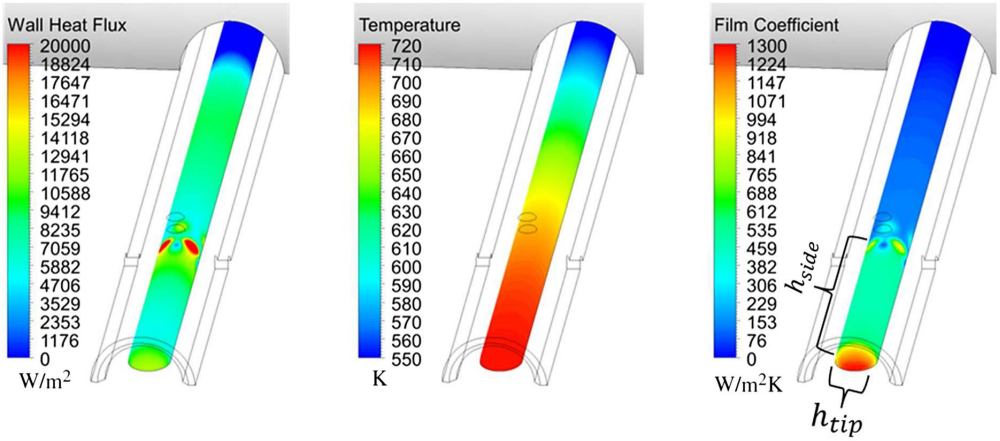

Fig. 17 Contours of sensor sheath heat flux (left), temperature (middle), and film coefficient (right) at $T_t = 850$°F.

Table 4 Tip and side film coefficient results for each simulation

Case	T_t, °F	p_s, atm	$\dot{m}/\dot{m}_{\text{ideal}}$	h_{tip}, W/(m^2 · K)	h_{side}, W/(m^2 · K)
Nominal	850	1	0.616	1269	563
1	850	1	0.677	1125	607
2	850	1	0.546	1113	457
3	850	1	0.506	1148	484
4	850	1	0.221	571	236
5	2500	10	0.593	3945	1101
5	850	1	0.640	1600	565
5	70	1	0.597	1256	386
6	2500	10	0.578	3742	1748
6	850	1	0.629	1456	533
6	70	1	0.624	1172	387
7	2500	10	0.570	3755	2048
7	850	1	0.562	1185	581
7	70	1	0.579	982	420
8	2500	10	0.551	3321	2021
8	850	1	0.53	1273	599
8	70	1	0.572	1044	448
9	2500	10	0.681	4224	1433
9	850	1	0.671	1173	415
9	70	1	0.664	963	318
10	2500	10	0.659	3765	1303
10	850	1	0.674	1181	345
10	70	1	0.692	906	268
11	2500	10	0.688	4209	350
11	850	1	0.721	1186	187
11	70	1	0.713	953	255

$$St = \frac{h}{(\rho u)_{\text{ave}} c_p} = \frac{h}{(\dot{m}/\dot{m}_{\text{ideal}})(\dot{m}_{\text{ideal}}/A)c_p} \tag{13}$$

where A is the area over which the mass flux is applied (see Fig. 18 for definition of relevant areas). Intuitively, one should expect the film coefficient to scale with the fluid velocity along the side of the sensor, which is established by the hydraulic area A_{hyd}, that exists between the TC and inner shield walls. For the tip region, the flow velocity is expected to be established by the shield inlet area A_{in}. Based on these assumptions, one can define the Reynolds and Stanton numbers for the side and tip regions as follows:

$$\begin{aligned} Re_{\text{side}} &= \frac{(\dot{m}/\dot{m}_{\text{ideal}})\dot{m}_{\text{ideal}} d_{\text{TC}}}{A_{\text{hyd}}\mu} \\ St_{\text{side}} &= \frac{h_{\text{side}}}{(\dot{m}/\dot{m}_{\text{ideal}})(\dot{m}_{\text{ideal}}/A_{\text{hyd}})c_p} \\ Re_{\text{tip}} &= \frac{(\dot{m}/\dot{m}_{\text{ideal}})\dot{m}_{\text{ideal}} d_{\text{TC}}}{A_{\text{in}}\mu} \\ St_{\text{tip}} &= \frac{h_{\text{tip}}}{(\dot{m}/\dot{m}_{\text{ideal}})(\dot{m}_{\text{ideal}}/A_{\text{in}})c_p} \end{aligned} \tag{14}$$

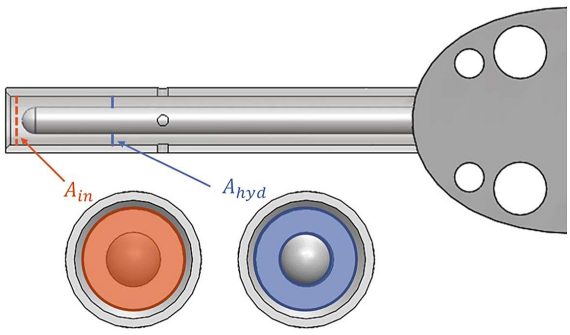

Fig. 18 Visualization of inlet and hydraulic areas (A_{in} and A_{hyd}) for Reynolds number and Stanton number definitions.

For most practical heat transfer applications, the laminar convective film coefficient is estimated using a correlation relating Reynolds and Prandtl numbers to the Nusselt number of the following form:

$$Nu_L = \frac{hL}{k_f} = aRe_L^b Pr^c \tag{15}$$

where a, b, and c are model constants; and L is the characteristic length scale [24]. Moffat [7] presented a correlation of this form in Eq. (2) for estimating the film coefficient for an unshielded bare-wire thermocouple in parallel flow, assuming a Prandtl number of 0.7 and a length scale based on TC diameter. Reardon et al. presented an improved correlation [Eq. (16)] for the performance of the nominal sensor geometry presented in this paper [13]. Rather than correlating on the sensor local Reynolds number, Reardon et al. used the freestream Reynolds number, which limits the applicability of this correlation to probes of a single fixed geometry:

$$Nu_{\text{Reardon}} = 0.52Re^{0.5} \tag{16}$$

In this paper, we use the sensor local Reynolds number, which is now readily available using Eqs. (11) and (14), to create a universal heat transfer correlation applicable for a wide range of probe geometries.

Previously unconsidered in performance correlations of shielded sensors is the impact of the annular ratio, $d_{\text{TC}}/d_{\text{shield}}$, on local heat transfer performance. Barrow [25] showed that the inclusion of an annular ratio multiplier in the heat transfer correlation yielded an improved description of the convective heat transfer coefficient on the inner wall of a turbulent annular flow. An additional annular diameter ratio term only improves the side heat transfer correlation for our shielded probe arrangement, where annular flow exists. Thus, the correlations for the side and tip are in the following forms:

$$\begin{aligned} St_{\text{side}} &= a_1(Re_{\text{side}})^{b_1}\left(\frac{d_{\text{TC}}}{d_{\text{shield}}}\right)^{c_1} \\ St_{\text{tip}} &= a_2 Re_{\text{tip}}^{b_2} \end{aligned} \tag{17}$$

Model coefficients were determined by fitting the CFD/CHT to the power models defined in Eq. (17) using a least-squares approach resulting in the final models in Eq. (18):

$$\begin{aligned} St_{\text{side}} &= 1.25(Re_{\text{side}})^{-0.59}\left(\frac{d_{\text{TC}}}{d_{\text{shield}}}\right)^{0.41} \pm 0.0025 \\ St_{\text{tip}} &= 1.68Re_{\text{tip}}^{-0.52} \pm 0.017 \end{aligned} \tag{18}$$

Figure 19 shows the model fit over the CFD/CHT points used for model generation. Note that, for presentation of the St_{side} model, the local Re_{side} is plotted versus $St_{\text{side}} \times (d_{\text{TC}}/d_{\text{shield}})^{-0.41}$, better showing the influence of the diameter ratio on side heat transfer performance. Also included in both Fig. 19 and Eq. (18) are the 95% confidence intervals of the Stanton number models, providing error estimates based on the spread of the data around the models. For an even more conservative estimate of model error due to computational gridding and turbulence model selection, percent differences in Tables 2 and 3 can be additionally applied.

For the generation of the correlations in Eq. (18), all data were used except for cases 4 (850°F), 5 (2500°F, and 11 (all conditions). The probe geometry in case 4 placed the vent holes nearest to the strut leading edge. This had the effect of significantly decreasing the mass flow rate ratio into the sensor as well as increasing the sensor heated length (see Fig. 11). This combination resulted in an increased latency of fluid within the shield, leading to significant losses in the total temperature of the fluid passing over the shield. This violates our key assumption that the fluid temperature is equal to the freestream total temperature within the shield, which is necessary for estimating probe performance using a priori information. The probe geometry in case 5 placed the smallest diameter sensor within the nominal shield.

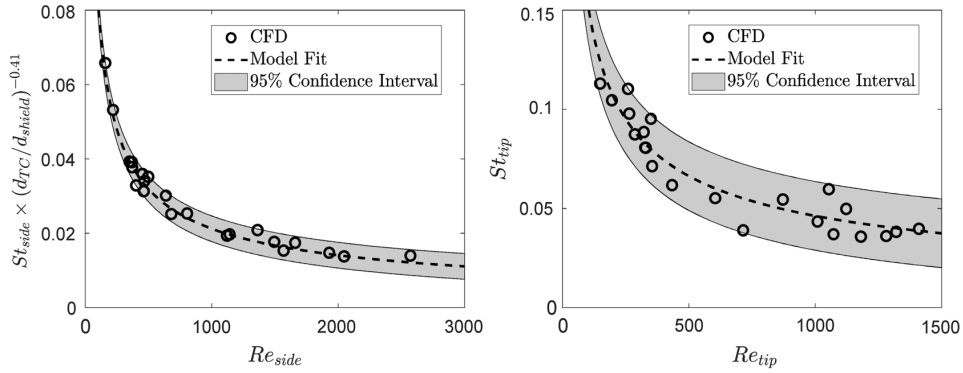

Fig. 19 Stanton number variation along TC side and tip with local flow Reynolds numbers. Each graph contains both CFD extracted points and empirical model fit with root-mean-squared error band.

It is well known that conduction errors can be mitigated by decreasing the diameter of the sensor [7]. For this particular case, the reduction in diameter combined with the increased freestream Reynolds number using the 2500°F freestream total temperature resulted in a sensor indicated temperature extremely close to the actual temperature of the flow. Based on how our local film coefficient is calculated [see Eq. (12)], this small difference in temperatures leads to a denominator approaching zero, making the film coefficient values highly sensitive. Therefore, the removal of this data point is warranted to avoid this sensitivity from heavily influencing the correlations. Finally, the probe geometry in case 11 placed the nominal diameter sensor into the largest shield (see bottom of Fig. 14). For all three freestream conditions, immediate flow separation from the tip of the sensor was observed without flow reattachment to the sides of the sensor. This separation is undesirable because it prevents the formation of a well-behaved boundary layer along the side of the sensor observed for all other cases, significantly reducing the convection heat transfer on the side of the sensor.

Two key observations of the Stanton number correlations presented here should be noted. First, the sensor tip heat transfer dependency on the flow Reynolds number is seen to be consistent with the *Nu–Re* correlation observed by Reardon et al. [13], based upon comparison of the Reynolds number exponents (both approximately $-1/2$). Conversion of Reardon's correlation using the relationship between Stanton and Nusselt numbers better illustrates the agreement:

$$St = \frac{Nu}{RePr} \;\; \therefore \;\; St_{\text{Reardon}} = \frac{0.52}{0.7} Re^{-0.5} \tag{19}$$

Second, the Stanton number dependence on $d_{\text{TC}}/d_{\text{shield}}$ agrees well with the correlations referenced by Barrow [25], who reported exponents for $d_{\text{TC}}/d_{\text{shield}}$ ranging from 0.15 to 0.45, supporting our exponent of 0.41. These comparisons provide confidence in the presented models, having been physically realized in past works.

These new Stanton number correlations have been created using an extensive range of probe geometric variations and freestream flow conditions, rendering them highly applicable to a wide range of practical problems. For the best use of these correlations, it is recommended that sensor-based local Reynolds numbers along the tip and sides of the sensor fall within the range of values tested in this study (see Fig. 19).

VI. Conclusions

A computational study has been conducted to examine the influence of sensor geometry on the convection heat transfer into the sensor of a strut-mounted vented-shield-style total temperature probe for an improved understanding of probe thermal performance with significant base cooling. The current investigations focused on the quantification of the film coefficients along the sensor upstream of the shield vents, due to the enhanced convection resulting from shield internal flow. High-fidelity computational fluid dynamics/conjugate heat transfer simulations were performed over a wide range of probe geometries with varying shield vent positions, sensor diameters, and shield outer diameters, providing detailed flowfield and heat transfer information, which is unattainable via available experimental techniques.

For characterization of the convective heat transfer over these sensor regions, it is shown that the convective heat transfer into a sheathed sensor in a vented shield is predominately governed by two local flow Reynolds numbers, which are defined over the sensor side and tip separately. These Reynolds numbers are directly proportional to the ratio of the mass flow rate through the sensor to an idealized mass flow rate based upon freestream conditions and the total vent discharge area. The response of this mass flow ratio to varying sensor geometric parameters can be readily explained via sensor aerodynamics. The pressure field set by interactions between the shield leading-edge separation and the strut stagnation region with the vent hole exit are dominant mechanisms. Internal viscous flow effects are small as compared to external effects over the range of cases studied.

A correlation relating mass flow ratio based on the vent hole location to shield length ratio, the sensor to shield inlet diameter ratio, and the ratio of the shield outer diameter to the mounting strut thickness was exhibited to collapse the data with $R^2 = 0.994$. Furthermore, two new local Reynolds to Stanton number correlations were created to provide a rapid estimation for the film coefficient over the side and tip regions of the sensor. Together, these physical insights and newly developed correlations provide a framework for better understanding the sensor thermal response to geometric changes. It is noteworthy that these normalized results were shown to be insensitive to the level of the approach flow total temperature.

Using the new, more generalized, empirical correlations for local sensor flow ($\dot{m}/\dot{m}_{\text{ideal}}$) and convective heat transfer behavior (St_{side} and St_{tip}), one may more readily and accurately predict the probe thermal performance in the presence of conduction using the low-order methods presented in the Conduction Errors section of this paper (Sec. II). This capability not only facilitates the evaluation of current and new sensor geometries for design studies, it importantly provides a deeper understanding of the flow physics governing probe thermal performance.

Although not in the scope of this paper, radiation can play a large role in the thermal performance of sensors in extreme temperature conditions. Given the new understanding of the convective heat transfer environment established by these sensors, the methods of Refs. [18,19] can yield precise predictions of thermal performance by further considering radiation.

Acknowledgments

The authors gratefully acknowledge the support for this work, in addition to many helpful technical discussions, provided by Pratt and Whitney through the Center of Excellence at the Virginia Polytechnic Institute and State University.

References

[1] Arenz, M. C., Weigel, B., Habermann, J., Staudacher, S., Rose, M. G., Lutum, E., and Berns, W., "Development and Application of a Fast-Response Total Temperature Probe for Turbomachinery," *ASME Journal of Turbomachinery*, Vol. 139, No. 5, 2017. doi:10.1115/1.4035278

[2] Hill, P. G., and Peterson, C. R., *Mechanics and Thermodynamics of Propulsion*, Addison-Wesley, Reading, MA, 1992.

[3] Moran, M. J., Moran, M. J., and Shapiro, H. N., *Fundamentals of Engineering Thermodynamics*, Wiley, Hoboken, NJ, 2005.

[4] Wertz, J. R., and Larson, W. J., *Space Mission Analysis and Design*, Microcosm, Hawthorne, CA, 2010.

[5] Skelton, R., Webster, G., De Mestral, B., and Wang, C., "Modelling Thermo-Mechanical Fatigue Hysteresis Loops from Isothermal Cyclic Data," *Thermo-Mechanical Fatigue Behavior of Materials*, Vol. 3, edited by H. Sehitoglu, and H. Maier, ASTM International, West Conshohocken, PA, 2000, pp. 69–84.

[6] Engler-Pinto, C., Sehitoglu, H., and Maier, H., "Cyclic Behavior of A1319-T7B Under Isothermal and Non-Isothermal Conditions," *Thermomechanical Fatigue Behavior of Materials*, Vol. 4, edited by M. McGaw, S. Kalluri, J. Bressers, and S. Peteves, ASTM International, West Conshohocken, PA, 2003, pp. 45–64.

[7] Moffat, R. J., "Gas Temperature Measurement," *Temperature: Its Measurement and Control in Science and Industry*, Vol. 3, 1962, pp. 553–571.

[8] Albertson, C. W., and Bauserman, W. A., "Total Temperature Probes for High-Temperature Hypersonic Boundary-Layer Measurements," NASA TM-4407, 1993.

[9] Bontrager, P. J., "Development of Thermocouple-Type Total Temperature Probes in the Hypersonic Flow Regime," Arnold Engineering Development Center, AEDC TR-69-25, Arnold AFB, TN, 1969.

[10] Warren, R. C., "Design of Thermocouple Probes for Measurement of Rocket Exhaust Plume Temperatures," Australia Dept. of Defense DSTO TR-0006, Melbourne, Australia, 1994.

[11] Eber, G. R., "Shielded Thermocouples," *Physical Measurements in Gas Dynamics and Combustion*, Princeton Univ. Press, 1954, pp. 186–197.

[12] Glawe, G. E., and Krause, L. N., "Miniature Probes for Use in Gas Turbine Testing," NASA TM X-71638.

[13] Reardon, J., Schetz, J. A., and Lowe, K. T., "Computational Modeling of Total-Temperature Probes," *Journal of Thermophysics and Heat Transfer*, Vol. 31, No. 3, 2017, pp. 609–620. doi:10.2514/1.T4991

[14] Schneider, A. J., "Computational Modeling of Total Temperature Probes," M.S. Thesis, Virginia Polytechnic Inst. and State Univ., Blacksburg, VA, 2015.

[15] Villafañe, L., and Paniagua, G., "Aero-Thermal Analysis of Shielded Fine Wire Thermocouple Probes," *International Journal of Thermal Sciences*, Vol. 65, March 2013, pp. 214–223. doi:10.1016/j.ijthermalsci.2012.10.025

[16] Braun, J., Lu, S., and Paniagua, G., "Development of High Frequency Virtual Thermocouples," *ASME. Turbo Expo: Power for Land, Sea and Air*, Vol. 6, ASME, Fairfield, NJ, June 2017, p. V006T05A026. doi:10.1115/GT2017-64669

[17] Zou, Z., Yang, W., Zhang, W., Wang, X., and Zhao, J., "Numerical Modeling of Steady State Errors for Shielded Thermocouples Based on Conjugate Heat Transfer Analysis," *International Journal of Heat and Mass Transfer*, Vol. 119, April 2017, pp. 624–639. doi:10.1016/j.ijheatmasstransfer.2017.11.034

[18] Vincent, T., Schetz, J. A., and Lowe, K. T., "Analysis of Pin Fins with Radiation," *Proceedings of 13th HEFAT Intlernational Conference*, HEFAT, Portoroz, Solvenia, July 2017.

[19] Schetz, J. A., Vincent, T., and Lowe, K. T., "Analysis of Base-Cooled Total Temperature Probes with Radiation," American Soc. of Mechanical Engineers Paper IMECE2016-65130, Fairfield, NJ, 2016.

[20] Saravanamuttoo, H. I., "Recommended Practices for Measurement of Gas Path Pressures and Temperatures for Performance Assessment of Aircraft Turbine Engines and Components," AGARD Rept. AR-245, Neuilly-Sur-Seine, France, 1990.

[21] ANSYS Fluent, Software Package, Release 16.0, Help System, ANSYS, Inc., Canonsburg, PA, Jan. 2015.

[22] Pope, S. B., *Turbulent Flows*, Cambridge Univ. Press, Cambridge, England, U.K., 2000, pp. 373–385, 461.

[23] Montgomery, D. C., Peck, E. A., and Vining, G. G., *Introduction to Linear Regression Analysis*, Wiley-Blackwell, Oxford, England, U.K., 2013.

[24] Icropera, F. P., Dewitt, D. P., Bergman, T. L., and Lavine, AgIve, *Fundamentals of Heat and Mass Transfer*, Wiley, Hoboken, NJ, 2007, pp. 401–456.

[25] Barrow, H., "Fluid Flow and Heat Transfer in an Annulus with a Heated Core Tube," *Proceedings of the Institution of Mechanical Engineers*, Vol. 169, No. 1, 2006, pp. 1113–1124. doi:10.1243/PIME_PROC_1955_169_109_02

4. Enhanced Low-Order Model with Radiation for Total Temperature Probe Analysis and Design

The contents of this chapter have been published in *SAE International Journal of Aerospace* (Tyler G. Vincent, Joseph A. Schetz, and K. Todd Lowe. "Enhanced Low-Order Model with Radiation for Total Temperature Probe Analysis and Design," *SAE Int. J. of Aerospace*. doi: 10.4271/01-11-01-0003).

Significant portions were previously presented as Tyler G. Vincent, Joseph A. Schetz, and K. Todd Lowe. "Enhanced Low-Order Model with Radiation for Total Temperature Probe Analysis and Design." In *AeroTech Congress and Exhibition*. doi: 10.4271/2017-01-2047.

Enhanced Low-Order Model with Radiation for Total Temperature Probe Analysis and Design

Tyler Vincent, *Virginia Tech*
Joseph Schetz, *Virginia Polytechnic Institute and State University*
K. Todd Lowe, *Virginia Tech*

Abstract

Analysis and design of total temperature probes for accurate measurements in hot, high-speed flows remains a topic of great interest in aerospace propulsion and a number of other engineering areas. One can apply detailed computational methods for simultaneous convection, conduction and radiation heat transfer, but such approaches are not suitable for rapid, routine analysis and design studies. For these studies, there is still a place for low-order approximate methods, and that is the subject of this paper. Here, an enhanced, low-order model is presented that includes conduction with variable thermal conductivity, convection with varying convection coefficient, varying diameter (and thus area) along the length of the sensor and radiation, all implemented in a convenient *MATLAB* code. We have also developed a new novel procedure to integrate the enhanced low-order model with computational fluid dynamics/conjugate heat transfer (CHT/CFD) simulations to accurately predict the important influences of radiation under different conditions in a very efficient manner.

History

Received: 01 Dec 2017
Revised: 19 Jan 2018
Accepted: 10 Feb 2018
e-Available: 16 May 2018

Keywords

Total temperature probe,
Gas turbine instrumentation

Citation

Vincent, T., Schetz, J., and Lowe, K.T., "Enhanced Low-Order Model with Radiation for Total Temperature Probe Analysis and Design," *SAE Int. J. Aerosp.* 11(1):2018, doi:10.4271/01-11-01-0003.

ISSN: 1946-3855
e-ISSN: 1946-3901

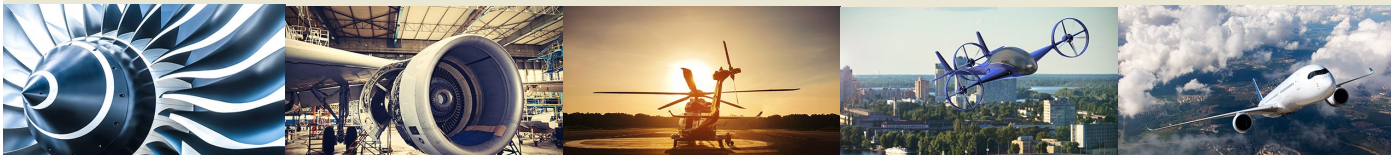

Introduction

The analysis, design, development and proper utilization of total temperature probes for accurate measurements in hot, high-speed flows remains a topic of great interest in a number of engineering topic areas, even though there exists a long, broad and deep prior literature on the subject (e.g. Refs. [1-10]). Prediction of error sources from convection, conduction and radiation is still an area of concern. For hot-flow conditions, the probe is normally mounted in a cooled support, leading to substantial axial conduction. Also, radiation plays a very important role in most hot, high-speed conditions. Of course, one can apply detailed computational methods for simultaneous convection, conduction and radiation heat transfer [11], but such approaches are not suitable for rapid, routine design studies. Consequently, there remains a useful role for low-order approximate analytic methods, and that is the focus of this paper.

Some useful, early analytical analyses of total temperature probes used an analogy to a so-called "pin fin" (see Figure 1) with combined convection and conduction [4, 5] from heat transfer enhancement applications. This approach has been applied to the total temperature probe situation [4, 5], but it is important to recognize some important differences in the two applications. First, the fluid flow direction of interest for the probe case is directed at the probe tip, not parallel to the wall. Second, a total temperature probe is usually mounted in a strut that is likely streamlined to some extent, not a flat wall. Third, most total temperature probes employ a thermocouple as the sensor, and none of the various thermocouple arrangements can be rigorously represented as a homogeneous rod. See Figure 2. Sometimes the exposed junction thermocouples have long wires extending out of a sheath or other mount.

The usual assumption is to represent the thermocouple as a homogeneous rod with an "effective" thermal conductivity determined by area weighting the properties of the wires and insulator and sheath. Fourth, most total temperature probes, especially for high-speed flows, have an outer vented shield to diffuse the flow over the sensor to a low velocity to minimize aerodynamic errors. In such cases, the convective heat transfer coefficient, h, must be modeled using the flow conditions inside the shield. Nonetheless, it is useful to review the treatments of the pin fin case.

Assuming 1-D conduction along a metallic fin with constant h and neglecting radiation, the analysis is simple, especially when one makes additional assumptions. Reference [12] provides a very thorough review of the literature. While useful, these treatments were quite restricted in a number of ways. Some, but not all, of the restrictions are covered in the Murray-Gardner-Kern Assumptions [12]: (1) The heat flow and temperature distribution are steady in time, (2) The fin material is homogeneous and isotropic, (3) There are no heat sources in the fin, (4) The heat flow to or from the fin surface is proportional to the temperature difference between the surface and the surrounding fluid, (5) The thermal conductivity of the fin is constant, (6) The heat transfer coefficient is the same over the fin surface, (7) The temperature of the surrounding fluid is uniform, (8) The temperature of the base of the fin is uniform, (9) Temperature gradients normal to the surface may be neglected (1-D assumption), (10) The heat transferred through the tip of the fin is negligible compared to that passing through the sides, (11) The joint between the fin and the prime surface offers no bond or contact resistance. One can add an additional common assumption: (12) Radiation is neglected, or radiation is treated without convection.

FIGURE 1 Schematic of the classical pin fin problem.

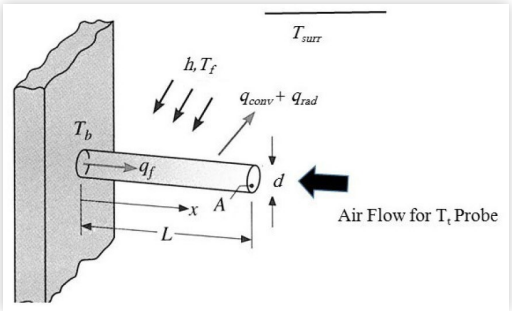

While useful, these treatments were very restrictive. In particular, the treatment of the tip of the fin either assumed an adiabatic condition or a film coefficient with the same value as on the sides of the fin. Both are very unrealistic for a flow directed at the tip of the probe. It is a simple matter to allow the film coefficient on the tip to be 3-5 times higher than on the side in accordance with empirical information and simulations, and that has been done in our earlier work [13]. In addition, one can expect the film coefficient to vary along the side of the probe, especially in the axially aligned flow depicted in Figure 1. Also, when the temperature

variation along the probe is substantial, as is common for total temperature measurements, the thermal conductivity cannot be assumed constant without introducing serious errors. Next, some probe configurations involve varying diameter and area along the length. See the right-hand side of Figure 2. Finally, it is very difficult to treat radiation from/to the fin (probe) within a purely analytical method. The only available solutions in the literature are limited to very restricted cases. Here, we will present an enhanced, low-order model that includes conduction with variable thermal conductivity, convection with varying convection coefficient, varying diameter (and thus area) along the length and radiation, all implemented in a convenient *MATLAB* code.

FIGURE 2 Typical thermocouple configurations used in total temperature probes (from www.capco.com).

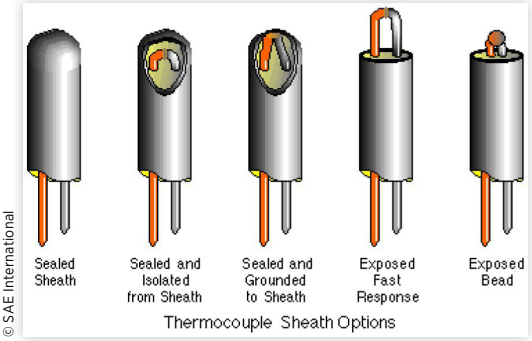

Review of Prior Pin Fin Analyses

Assuming 1-D conduction along a pin fin, the nonlinear ordinary differential equation (ODE) to be treated with radiation included can be written [14]:

$$\frac{d}{dx}\left[k(T)A(x)\frac{dT}{dx}\right]=h(x)P(x)\left[T(x)-T_f\right]+\sigma P(x)\left[\varepsilon T^4(x)-\alpha T_{surr}^4\right] \quad \text{Eq. (1)}$$

The term on the left-hand-side represents axial conduction, the first term on the right-hand-side represents convection, and the second term on the right-hand-side represents radiation.

Assuming, for the moment, a constant cross-section area (and hence perimeter) and h and k constant and $\varepsilon = \alpha$, the governing equation reduces to:

$$\frac{d^2T}{dx^2}=\frac{hP}{kA}\left[T(x)-T_f\right]+\frac{\sigma\varepsilon P}{kA}\left[T^4(x)-T_{surr}^4\right] \quad \text{Eq. (1a)}$$

The simplest cases neglect radiation, and the equation above reduces to a linear ODE with a well-known solution [3], but, the assumption of constant h is unrealistic. It is an easy matter to extend the solution to have $h_{tip} \neq h$ by modifying the boundary condition at $x = L$. The result is [13]:

$$\frac{T(L)-T_f}{T_b-T_f}=\frac{1}{\cosh(mL)+\frac{h_{tip}}{mk}\sinh(mL)} \quad \text{Eq. (2)}$$

For the total temperature probe application under consideration here, the "recovery temperature" on the probe tip, $T(L)$, is the result of primary interest.

Consider next prior treatments of the pin fin problem including radiation using Equation 1a. The BC at $x = L$ is now

$$h_{tip}\left[T(L)-T_f\right]+\sigma\varepsilon\left[T(L)^4-T_{surr}^4\right]=-k\left[\frac{dT}{dx}\right]_{x=L} \quad \text{Eq. (3)}$$

Since Equation 1a is a non-linear ODE, analytical solutions are only obtainable for limited cases. If $T_{surr} = T_f$, multiply Equation 1a by dT/dx and integrate once to get [14]:

$$\frac{1}{2}\left(\frac{dT}{dx}\right)^2=\frac{hP}{kA}\left[\frac{1}{2}T^2-TT_f\right]+\frac{\sigma\varepsilon P}{kA}\left[\frac{1}{5}T^5-TT_f^4\right]+C \quad \text{Eq. (4)}$$

Consider now a purely hypothetical scenario intended to make the governing equations solvable. For the very restrictive case where $T_f = 0$ and a very long fin so that both $T(L)$ and $(dT/dx)_x = L \to 0$, $C = 0$

$$\frac{dT}{dx} = \pm\sqrt{\frac{2}{5}\frac{\sigma\varepsilon P}{kA}T^5 + \frac{hP}{kA}T^2} \qquad \text{Eq. (5)}$$

One selects the appropriate sign for the expected behavior of dT/dx. For example, if $T(x)$ is decreasing along the fin, the minus sign is appropriate. Using $T(0) = T_b$ one can integrate to obtain:

$$\int_0^x dx = -\int_{T_b}^{T} \frac{dT}{T\left[\frac{2}{5}\left(\frac{\sigma\varepsilon P}{kA}\right)T^3 + \frac{hP}{kA}\right]} \qquad \text{Eq. (6)}$$

Further integration yields the closed form solution [14]:

$$x = \frac{1}{3m}\left[\ln\frac{\sqrt{GT_b^3 + m^2} - m}{\sqrt{GT_b^3 + m^2} + m} - \ln\frac{\sqrt{GT^3 + m^2} - m}{\sqrt{GT^3 + m^2} + m}\right] \qquad \text{Eq. (7)}$$

where $G = 2/5(\sigma\varepsilon P/kA)$. Even though this solution is only obtained through the application of very limiting assumptions, it is still useful by displaying the key lumped parameters, G and m.

One can find interesting solutions for other restricted cases in the literature, all for $h_{tip} = h$ or an insulated tip where $(dT/dx)_x = L \to 0$. See for example Refs. [15, 16]. Generally, numerical evaluation of complex integrals is required even for such restricted cases. Cases with variable cross-section area, $A(x)$, and variable heat transfer coefficient, $h(x)$, (except for the simplest case of $h_{tip} \neq h$) are much more complicated. See Ref. [12] for a thorough exposition of available results. Reference [17] considered variable $k(T)$ and simplified $h(x)$ variations. There is much less work in the literature for cases with varying $A(x)$ and $h(x)$ in the presence of radiation.

Based on the discussions above, we conclude that there is no suitable analytic solution for general application to the pin fin case. That conclusion motivates to the work described in the following sections.

Numerical Methods and Validation

The goal of this work was to develop and implement a numerical solution that generalizes the thermal behavior of a 1-D, conducting, pin fin representation of a total temperature probe with radiation. This means allowing for variable heat transfer coefficient and area along the length, $h(x)$ and $A(x)$ respectively. For cases with large thermal gradients, model accuracy can be further improved by replacing the constant solid conductivity assumption with a local temperature dependent conductivity, $k(T)$. Assuming $\varepsilon = \alpha$, the governing differential equation takes the form:

$$\frac{d}{dx}\left[k(T)A(x)\frac{dT}{dx}\right] = h(x)P(x)\left(T(x) - T_f\right) + \varepsilon\sigma P(x)\left(T(x)^4 - T_{surr}^4\right) \qquad \text{Eq. (8)}$$

The problem further requires two boundary conditions. At $x = 0$, $T(0) = T_b$ and at $x = L$:

$$\left.\frac{dT}{dx}\right|_{x=L} = \frac{-h_{tip}}{k\left(T(L)\right)}\left(T(L) - T_f\right) - \frac{\varepsilon\sigma}{k\left(T(L)\right)}\left(T(L)^4 - T_{surr}^4\right) \qquad \text{Eq. (9)}$$

This is a "two-point boundary value problem" since the two required boundary conditions are applied at two values of the independent variable, x. There are three main ways to treat such problems [18]: *Shooting, Finite Differences* and *Projections*. In the *Shooting* method, one estimates the value of the slope at $x = 0$, and then iterates until the desired boundary condition at the other point is matched. In the *Finite Difference* approach, a mesh is introduced over the domain, and derivatives in the ODE are replaced by finite differences. This leads to an algebraic system that may be solved to produce a discrete approximation to the problem. In the *Projections* method, the solution is approximated by simpler functions, *e.g.* polynomials, and the differential equation and boundary conditions are satisfied approximately. Collocation or finite element methods can furnish these approximations. In our previous low-order model work with constant h, k and A [13], the *Shooting* method was employed. As the boundary condition to match becomes more complicated, as in Equation 9, the method of "shooting" to match the condition becomes problematic. Here, we have selected an implicit *Finite Difference* approach because it was found to be more robust.

The local first and second spatial derivatives of temperature and geometry are approximated using a second-order accurate, 5-point central-differencing scheme, derived to allow for non-uniform element lengths. Non-uniform gridding can help improve accuracy with a reduction in computational cost by allowing for finer grids near regions of large spatial gradients (thermal, geometric, or film coefficient) without the need to refine regions of small gradients where coarser grids are adequate. Since we wish to solve for the temperature at each node along the fin, the implicit *Finite Difference* method requires n equations for n node temperatures. At nodes $i = 1$ and $i = n$, the two boundary conditions described above are applied ($x(i = 1) = 0$ and $x(i = n) = L$).For each of the nodes $2 \le i \le (n - 1)$, the discrete form of Equation 8 is used. Due to the non-linearity of the governing equation with radiation, an iterative approach is required to solve the system of equations. *MATLAB*'s *fsolve* function is built to solve such a system of non-linear equations. To use *fsolve*, one must provide an initial guess for the temperature solution along the length of the fin. While a good initial guess is not critical for convergence, it can reduce computational cost. A simple, yet effective initial guess for *fsolve* is a linear temperature profile along the length, where the base is equal to the known base temperature and the tip is equal to the surrounding fluid temperature.

Due to the unavoidable truncation errors arising from necessarily neglecting higher-order terms in the estimation of local derivatives, one must check the final temperature solution for grid independence. For solutions presented in this paper, a 1000-node grid with a refinement bias towards the base (finest elements near the fin base) produced converged results, although 500 and 100-node grids also produce adequately accurate results for most applications while greatly reducing computational cost.

There are a few limiting examples where exact solutions are available that can be used to validate our numerical method. They are considered in the next subsections.

Constant Cross-Section Area Sensor with Constant Thermal Conductivity, *k*, and Heat Transfer Coefficient, *h*

A simple model for the performance of a sheathed thermocouple sensor may be obtained by considering a pin fin with constant cross-section area, A, and heat transfer coefficient, h, (except for the simplest case of $h_{tip} \neq h$). The first validation case has the solution in Equation 2 where radiation is neglected. The second is the very restricted radiation situation with the solution given here as Equation 7. We selected a test case for a probe representative of a Type K thermocouple in an Inconel sheath: $d = 1.0$ mm, $L = 10$ mm, $k = 16$ W/mK, $\varepsilon = 0$ and 1.0, $T_b = 300$ K, $T_f = 1000$ K, $T_{surr} = 300$ K, $h = 1000$ W/m^2 K and $h_{tip}/h = 1.0$.

Using Equation 2 with the above test case conditions, one finds that the tip temperature is 991.6 K for this simulated probe with a cooled base in a high convection environment. The result from the current numerical solution with $\varepsilon = 0$ using 1000 nodes

yields a tip temperature that matches the analytical value of 991.6 K, as it should. The corresponding solution including radiation with $\varepsilon = 1.0$ yields a tip temperature of 948.5 K. Radiation reduces the sensor performance in this example.

The second restricted case for which an exact solution exists (Equation 7) allows radiation, but requires assuming $T_f = T_{surr} = 0$ and a very long fin so that both $T(L)$ and $(dT/dx)_x = L \rightarrow 0$. It is obvious that these are severe restrictions, but we can still use the predictions to compare with our numerical solution as a validation case. Radiation can be enhanced by choosing $T_b = 1500$ K and reducing convection with $h = 50$ W/m^2 K and an adiabatic tip ($h_{tip}/h = 0$). The temperature decay is also likely slower, so L was increased to 100 mm to better simulate the infinite length required for the analytic solution. The analytical solution in Equation 7 for this case gives $x = 8.37$ mm for $T(x) = 500$ K, and the numerical result agrees very well with that. Neglecting radiation would lead to an error of more than 100 K at that location.

Constant Cross-Section Area Sensor with Variable Heat Transfer Coefficients over the Surface

A more realistic model for sheathed thermocouple performance includes the possibility of varying heat transfer coefficient along the length of the sensor, $h(x)$. Pin fin analyses have included this possibility; see for example Ref. [19] and the extensive review of older work in Ref. [12]. Unfortunately, there is no simple, analytic solution with variable heat transfer coefficient even without radiation available that can be used to validate the current numerical procedure. We can, however, show predictions for a few cases and then compare the trends observed with those found in the literature with more elaborate analyses. The cases selected for these comparisons had: $k = 16$ W/mK, $h_{ave} = 500$ W/m^2 K, $h_{tip} = 0$ (for better comparison with elaborate analysis from the literature [19]), $L = 10$ mm, $d = 1.0$ mm, $T_f = 1000$ K, $T_b = 300$ K, and $T_{surr} = 300$ K.

In Figure 3, we show the current results for this case excluding radiation, but with both h = constant = $h_{ave} = 500$ W/m^2 K and also a linear $h(x)$ starting from 0 at the fin base $x/L = 0$ and having the same $h_{ave} = 500$ W/m^2 K. A low value of the film coefficient near the base and a high value near the tip can be expected in practical total temperature probe situations. One can easily see that a varying $h(x)$ has a large effect on the temperature distribution along the fin. Here, we found a tip temperature of 959.2 K for the constant h assumption and 968.6 K for the linear $h(x)$. Furthermore, we found a fin efficiency (the ratio of the actual fin heat transfer rate to the "ideal" fin heat transfer rate calculated assuming the entire fin is maintained at the base temperature) of 0.2824 for the constant h assumption and 0.1703 for the linear $h(x)$. This behavior of a constant h assumption over-predicting fin efficiency is in agreement with the literature [19] for other assumed $h(x)$ cases. We take this as at least partial validation of the current numerical method.

FIGURE 3 Numerical solution results for Validation Case no. 3: $d = 1.0$ mm, $L = 10$ mm, $k = 16$ W/mK, $\varepsilon = 0$, $T_b = 300$ K, $T_f = 1000$ K, $h_{ave} = 500$ W/m^2 K and $h_{tip}/h = 0.0$. h = constant (top/blue curve) and linear $h(x)$ (bottom/red curve), both with $h_{ave} = 500$ W/m^2 K.

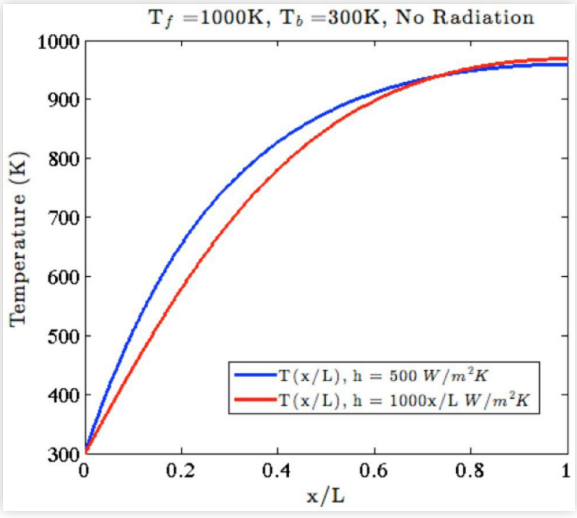

Variable Cross-Section Area Fins with Constant Heat Transfer Coefficients over the Surface

In many heat transfer enhancement applications, it is desirable to design a pin fin with a variable cross sectional area along its length, $A(x)$. This may be motivated by several factors including the fin's structural capabilities, volumetric constraints, or

various heat transfer requirements. An area varying along the length of a total temperature probe can also be of interest.

For the case of constant heat transfer coefficient without radiation, several analytical solutions exist in the literature [20]. For validation of variable area incorporation into the current numerical method, we computed the temperature solution for a conical fin with a base diameter d = 1.0 mm, L = 10 mm, k = 16 W/mK, ε = 0, T_b = 300 K, T_f = 1000 K, h = 1000 W/m^2 K and h_{tip}/h = 0.0. Evaluation of the analytic fin efficiency for the input parameters described above yields 0.3417. Our numerical calculations show excellent agreement, thus validating the numerical approach for variable area fins (and/or probes).

Example Cases

Constant Cross-Section Area with Constant Heat Transfer Coefficient

In specifying a total temperature sensor design, sensor length-to-diameter ratio becomes a primary variable. We can investigate that variable with the tools developed here. Consider a range of cylindrical fins with length to diameter ratio, L/d, ranging from 1.0 to 10.0 under the conditions presented in Figure 4, with diameter fixed at d = 1 mm. To emphasize the impact of radiation, we used a side film coefficient of h = 500 W/m^2 K. Results for the sensor tip temperature for each length are given in Figure 4.

The influence of conduction to the cooled base reduces the sensor tip temperature as the sensor becomes shorter. Also, it can be observed that there is a region beyond which further increasing the sensor length shows a diminishing improvement of the agreement between the gas and tip temperature. Beyond roughly L/d = 20, further increases in length are not helpful. Lastly, it can be seen that the effects of radiation are diminished as the sensor becomes shorter.

Variable Cross-Section Area Sensors with Constant Heat Transfer Coefficient over the Surface

Complex sensor geometries may be chosen for manufacturing, structural or performance reasons. For instance, changing the sensor diameter as a function of the sensor length allows the designer to control the behavior of the axial temperature profile. A method for modeling axial changes in the sensor cross-section area must also allow for changes in heat transfer coefficient which will be driven by the changing geometry. The current method allows for such modeling, but we chose to hold heat transfer constant in this set of cases. To investigate the effect of axial area variation, we can consider the temperature solution for three sensors all with a base diameter d = 1 mm and L = 10 mm with differing profiles-cylindrical, conical, and convex parabolic-as large variations for comparison. Setting T_b = 300 K, T_f = 1000 K, T_{surr} = 300 K, h = 100 W/m^2 K and h_{tip}/h = 0.0, we can compare the sensor thermal response as a function of position as shown in Figure 5.

It is apparent that as the tip becomes more slender due to the profile shape definition, the tip temperature reaches closer

FIGURE 4 Numerical solution results for: d = 1.0 mm, k = 16 W/mK, ε = 0 (top/blue curve) and ε = 1.0 (bottom/red curve), T_b = 300 K, T_f = 1000 K, T_{surr} = 300 K, h = 500 W/m^2 K and h_{tip}/h = 0.0.

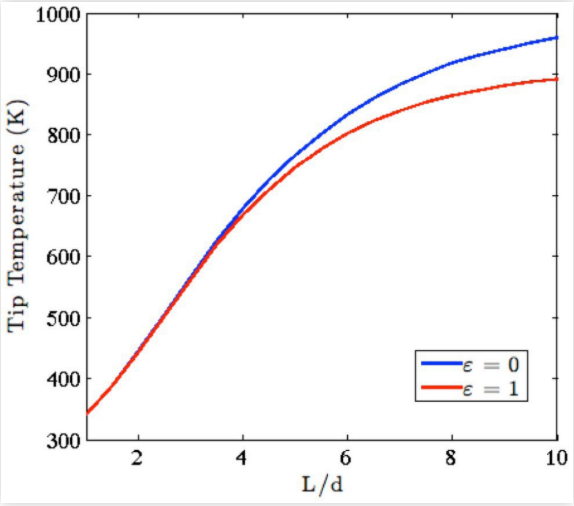

FIGURE 5 Numerical solution results for varying fin profiles with: d_{base} = 1.0 mm, L = 10 mm, k = 16 W/mK, ε = 0 (solid curves) and ε = 1.0 (dotted curves), T_b = 300 K, T_f = 1000 K, T_{surr} = 300 K, h = 100 W/m² K and h_{tip}/h = 0.0.

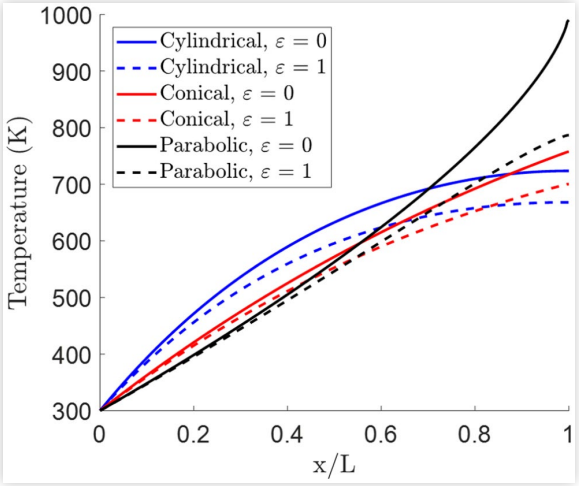

FIGURE 6 Numerical solution results cylindrical platinum thermocouple with: d_{base} = 0.5 mm, L = 5 mm, k = 80 W/mK (blue curves) and $k(T)$ = 70 + 0.0167(T-300) W/mK (red curves), ε = 0 (solid curves) and ε = 1.0 (dotted curves), T_b = 500 K, T_f = 1500 K, T_{surr} = 1500 K, $h(x/L)$ = 100x/L W/m² K and $h_{tip}/h(L)$ = 3.0.

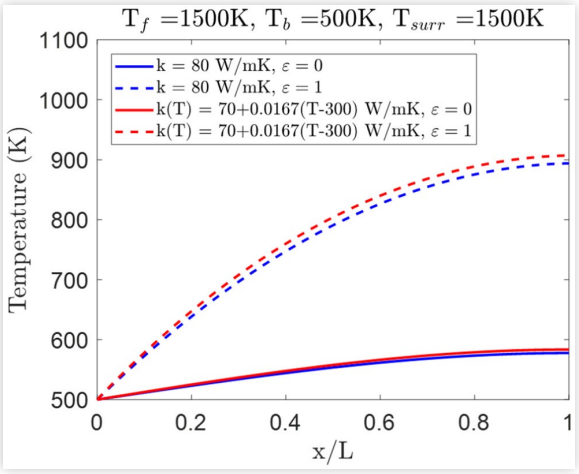

to the surrounding fluid temperature ($T(L)$ = 723 K, 757 K and 990 K for the cylindrical, conical and parabolic fins without radiation respectively). By accounting for radiation to the cooler surroundings, the sensor temperatures can be seen to drop as expected. Most notable is a 203 K reduction in the recovery temperature at the tip of the parabolic cross-section sensor when compared with the solution without radiation.

Constant Cross-Section Area Sensors with Variable Heat Transfer Coefficient over the Surface and Temperature Dependent Thermal Conductivity

A prior literature review of 1-D pin fin solutions revealed very little consideration with regard to varying thermal conductivity based on local temperature. A constant thermal conductivity assumption can prove reasonably accurate if the temperature gradients along the fin are small. However, in cases where the fin base is significantly cooler than the surrounding fluid, large thermal gradients can exist along the fin's length. In extreme cases, temperatures gradients can exist on the order of 1000 K per inch [14]. It is for these specific cases that relaxing the constant thermal conductivity assumption is beneficial.

Consider now a sensor modeled as a cylindrical probe made with a material representative of a platinum thermocouple. At 300 K, platinum has $k \approx 70$ W/mK and at 1500 K, $k \approx 90$ W/mK [21]. As a first major step towards temperature dependent thermal properties, let us assume that k varies in a locally linear manner with temperature as in Equation 10:

$$k(T) = k_0 + k_1 (T - T_0) \qquad \text{Eq. (10)}$$

For platinum, we may approximate $k(T)$ as linear using k_0 = 70 W/mK at a reference temperature T_0 = 300 K and slope k_1 = 0.0167 W/mK². To utilize the full generality of our numerical approach, we may also apply a non-uniform film coefficient profile along the side of the fin, which varies linearly from $h(x = 0)$ = 0 W/m² K to $h(x = L)$ = 100 W/m² K with an elevated tip film coefficient given by $h_{tip}/h(x = L)$ = 3.0, as well as compare solutions with and without radiation. Taking base diameter d = 0.5 mm, L = 5 mm, T_b = 500 K, T_f = 1500 K, T_{surr} = 1500 K, we get the results shown in Figure 6. Also shown is the solution if k is assumed constant at the average of the base and fluid temperatures.

Due to the large variability in profile temperatures, using conductivity with linear temperature dependence gives a better answer with minimal increase in computational cost. A probe tip temperature comparison between results including radiation shows a 13 K increase in tip temperature when using $k(T)$ compared to k = constant in the presence of radiation (907.1 K and 894 K respectively). Furthermore, in the absence of strong convective conditions, radiation tends to dominate. The effect of radiation can be observed by the 300 K differences in tip temperatures between solutions with and without radiation.

Validation and Integration with CFD/CHT

The use of the enhanced low-order model (LOM) presented above to predict the probe thermal profile requires knowledge of the heat transfer conditions along the surface, namely the local convective film coefficient, and including radiative view factors and emissivity/absorptivity of the TC and its surroundings. Due to challenges associated with experimental measurements of film coefficient on small surfaces, it has become common to rely on CFD with conjugate heat transfer (CHT) to capture necessary physical details required for accurate film coefficient determination. In this section, we use CFD/CHT with and without radiation in order to validate the fin governing equations used for thermal performance predictions. Furthermore, it is shown that our enhanced LOM can be used as a non-linear radiation correction tool for computations excluding radiation, which greatly reduces computational time while maintaining high fidelity. The procedure for radiation solution correction is as follows:

1. Perform steady-state CFD/CHT without radiation to get film coefficient profile, $h(x)$.
2. Use $h(x)$ from (1) as input to LOM code and validate that solution from CFD/CHT and LOM agree for case without radiation using:

$$\frac{d}{dx}\left[kA_c\frac{dT}{dx}\right]=h(x)P\left(T-T_f\right) \qquad \text{Eq. (11)}$$

3. Now, add radiation by specifying emissivity and surrounding temperatures in LOM code using:

$$\frac{d}{dx}\left[kA_c\frac{dT}{dx}\right]=h(x)P\left(T-T_f\right)+\varepsilon\sigma P\left(T^4-T_{surr}^4\right) \qquad \text{Eq. (12)}$$

FIGURE 7 Computational setup for CFD/CHT. Axisymmetric representation of a sheathed TC in ambient flow with chilled base excluding radiation.

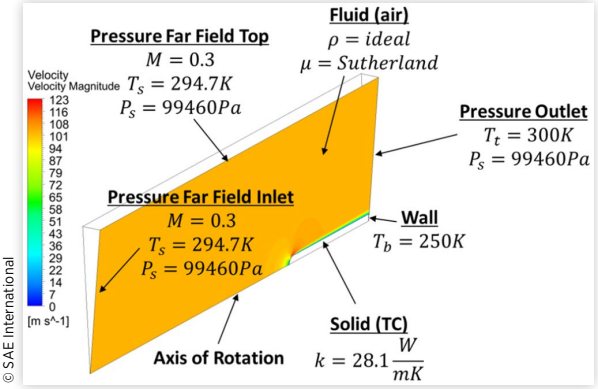

FIGURE 8 Mesh of CFD/CHT computation. 2D unstructured tetrahedral elements used to compose the fluid and solid regions with quadrilateral inflation layer elements near sheath wall.

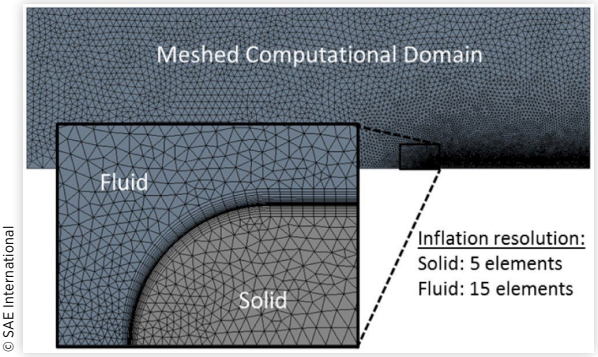

For this CFD/CHT analysis shown in Figure 7, a homogeneous rod of constant thermal conductivity with a rounded tip representative of a 0.010 inch, type E (k = 28.1 W/mK) sheathed TC with an L/d of 10 was aligned axially to an oncoming steady flow at a Mach number of 0.3 and total temperature of 300 K at ambient pressure (99460 Pa). The fluid used was ideal air with temperature dependent dynamic viscosity based on Sutherland's Law. The k-ω SST turbulence model was used with default values for model constants provided in ANSYS Fluent 17.0. Pressure-far-field boundary conditions were applied to both the inlet and the top surfaces of the computational domain with a turbulent intensity of 1% and turbulent viscosity ratio equal to one. The exit plane was defined using a pressure outlet boundary with ambient gage pressure. A fixed temperature boundary condition of 250 K was applied at the base of the TC in order to induce significant conduction along the fin, a phenomenon commonly observed with chilled-mount probes. The problem was simplified using a quasi-3D axisymmetric approach. ANSYS Mesh Generator was used to produce the 2D unstructured grid (Figure 8), consisting of 19,166 fluid elements and 4,921 solid elements. Inflation layers were generated in

FIGURE 9 Film coefficient profile on TC surface as function of non-dimensional axial location for CFD/CHT solution without radiation.

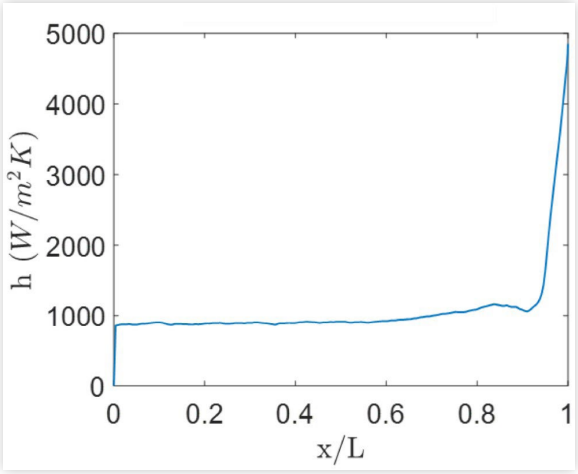

FIGURE 10 Temperature profile as function of non-dimensional axial location for LOM (dashed) and CFD/CHT (solid) excluding radiation.

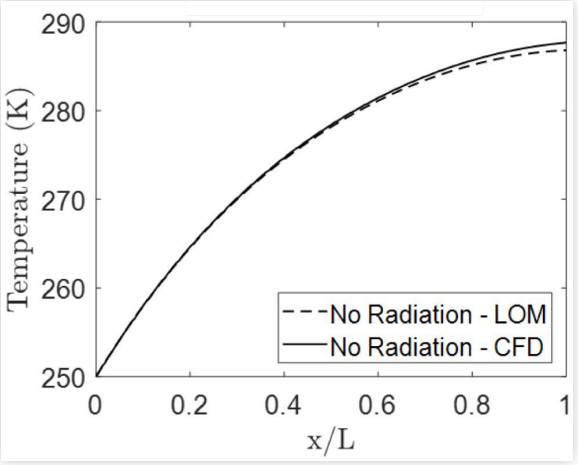

both the fluid and solid domains near the TC surface with element counts of 15 and 5 elements thick respectively.

Following the procedure listed above, step (1) requires a steady-state CFD/CHT solution to the model problem without radiation. The film coefficient profile was extracted from the converged solution as a function of the axial position along the surface of the TC and that is plotted in Figure 9, where $x/L = 0$ and 1.0 are the TC base and tip locations, respectively. The film coefficient, as used in our LOM, is defined as the ratio of the local surface heat flux to the temperature difference between the local wall and surrounding fluid temperature, $h(x) = \frac{q(x)}{T_f - T(x)}$. A user-defined expression of this form was set in ANSYS Post to define the desired film coefficient profile, with the added assumption that $T_f \approx T_t$. The film coefficient profile behaves as expected with a nearly constant value along the TC length and an enhanced film coefficient value at the tip, agreeing with the widely observed h_{tip}/h_{side} of 3 to 5 [11].

The film coefficient profile from (1) can now be input into the LOM code to predict the temperature solution. Presented in Figure 10 is a comparison of the LOM predictions and CFD/CHT temperature profile solutions without radiation. The tip temperature prediction is approximately 1 K lower than the CFD/CHT solution, but it is well within desired solution accuracy considering the large conduction effects present. With this comparison, our enhanced LOM has been validated for solutions without radiation.

The final step (3) is to use the film coefficient profile obtained from the no-radiation CFD/CHT solution in the LOM predictions now including radiation. This analysis assumes that the inclusion of radiation will have minimal effect on the previously calculated film coefficient, especially in the presence of high forced convection. By changing the emissivity from 0 to 1.0 and establishing a surrounding temperature of 1000 K (further assuming emissivity = absorptivity), we can obtain a new "corrected" solution including the effects of radiation. The black curves in Figure 11 show the previous solutions without radiation computed using CFD/CHT and the LOM.

Without the need to perform a new CFD computation, the "corrected" solution including radiation is shown by the dashed red line. For comparison, a CFD/CHT computation including radiation was performed using the Discrete Ordinates (DO) model in ANSYS Fluent (solid red line). The difference between the CFD/CHT and LOM including radiation was less than 1.5 K, maintaining a high level of accuracy coupled with a significant reduction in computation time.

The CFD/CHT computation was performed on a 6-core Workstation, resulting in an approximately 10 minute computation, which was reduced to under 5 seconds using our LOM code. This was a relatively inexpensive CFD/CHT computation due to the axisymmetric simplification and simple geometry. For much more complex problems, such as full 3D computations with sensor/mount interactions, the saved computational time becomes even more significant due to no added complexity to the LOM once an acceptable film coefficient profile is determined.

Summary/Conclusions

We have greatly extended the pin fin analysis that has been used previously to model total temperature probes. Here, an enhanced, low-order model is presented that includes conduction with variable thermal conductivity, convection with varying convection coefficient, varying diameter (and thus area) along the length of the sensor and radiation, all implemented in a convenient *MATLAB* code. The method was validated by comparing results with available analytic solutions that are applicable for restricted cases and a CFD/CHT simulation.

To illustrate the utility of the new analysis tool presented here, a few example cases were selected to study the influences of some key parameters. In particular, radiation on or off, h_{tip}/h ratio, probe length, and thermocouple and sheath material choices were considered. The tool can be used to thoroughly study these items and any other combinations of parameters that describe the general problem.

Of course, in order to use this new tool for specific applications, one needs simple methods to find values of h_{tip} and h or h_{tip}/h. For unshielded probes, the correlation for $Nu_d(Re_d)$ in Ref. [10] can be used to find $h_{tip.}$ Moffat also suggests that typical shielded probes diffuse the velocity to about 1/8th of the freestream value. Assuming an isentropic diffusion process, the same $Nu_d(Re_d)$ correlation might be used with a modified local value for Re_d to find h_{tip}. Alternatively, CFD/CHT methods such as in Ref. [11] can be used to find h_{tip} correlations for specific shielded probe configurations. One such correlation is given in Ref. [11]. Last, we have already noted that the available information suggests h_{tip}/h values of 3-5, and that can be used to determine h.

We have also developed a new and unique computational procedure to integrate the enhanced low-order model with CFD/CHT to accurately predict the important influences of radiation under different conditions in a very efficient manner.

The work presented here focuses on steady-state probe performance. However, temporal response can be equally as important, especially for small probes in a highly unsteady environment. The addition of a thermal diffusivity term in the governing equations can further allow for time dependent solutions under a variety of forcing functions and will be the topic of future work. Furthermore, we envision adding a model for the influence of a streamlined, cooled mounting strut. Last, it is a simple matter to relax the assumption that emissivity = absorptivity.

Finally, the methods developed here for application to total temperature probes clearly also can be usefully employed for usual pin fin applications in heat transfer enhancement.

The *MATLAB* code is posted at:
http://www.aoe.vt.edu/research/onlinesoft.html/.

FIGURE 11 Temperature profile as function of non-dimensional axial location for LOM (dashed) and CFD/CHT (solid) excluding radiation.

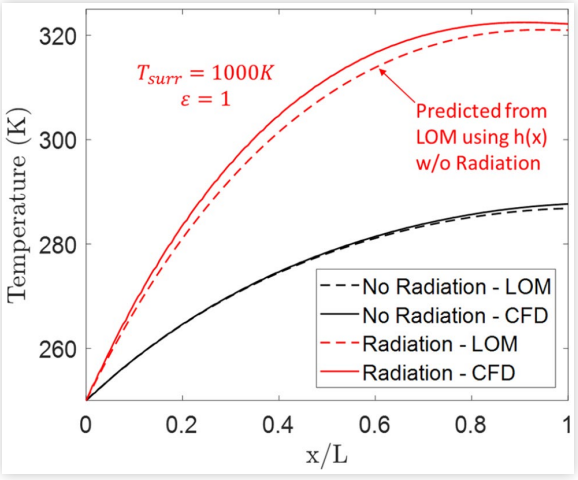

Contact Information

Direct communications to
Prof. Joseph Schetz
ptiger@vt.edu.

Definitions/Abbreviations

A(x) - area

CFD - computational fluid dynamics

CHT - conjugate heat transfer

$d(x)$ - diameter
G - $=2/5(\sigma\varepsilon P/kA)$
$h(x)$ - side convection coefficient
h_{tip} - tip convection coefficient
i - node index
$k(T)$ - thermal conductivity
k_0 - reference conductivity
k_1 - slope of conductivity variation
L - length
LOM - low-order model
m - $=(hP/kA)^{1/2}$
n - number of nodes
$P(x)$ - perimeter
$T(x)$ - temperature
T_0 - reference temperature
T_f - fluid temperature
T_b - base temperature
T_{surr} - surroundings temperature
x - base to tip coordinate
Δx - element length
α - absorptivity
σ - Stefan-Boltzmann constant
ε - emissivity
1-D - one-dimensional

References

1. Franz, A., "Pressure and Temperature Measurement in Supercharger Investigations," NACA Technical Report NACA-TM-953, National Advisory Committee for Aeronautics, 1940.
2. Lindsey, W.F., "Calibration of Three Temperature Probes and Pressure Probe at High Speeds," Report, National Advisory Committee for Aeronautics, 1942.
3. King, W.J., "Measurement of High Temperatures in High-Velocity Gas Streams," *Trans. ASME* 65:421, 1943.
4. Hottel, H.C. and Kalitinsky, A., "Temperature Measurements in High-Velocity Air Streams," *Journal of Applied Mechanics* 12:A25-A32, 1945.
5. Markowski, S. and Moffatt, E., "Instrumentation for Development of Aircraft Powerplant Components Involving Fluid Flow," SAE Technical Paper 480179, 1948, doi:10.4271/480179.
6. Gerhard, R.E., "Shielded Thermocouples," in *Physical Measurements in Gas Dynamics and Combustion*, (Princeton, NJ, Princeton University Press, 1954).
7. Winkler, E.M., "Design and Calibration of Stagnation Temperature Probes for Use at High Supersonic Speeds and Elevated Temperatures," *Journal of Applied Physics* 25:231-232, 1954, doi:10.1063/1.1721609.
8. Moffat, R.J., "Gas Temperature Measurement," in A. I. Dahl (Ed.), *Temperature, Its Measurement and Control in Science and Industry*, Vol. 3, Part 2, (Reinhold, New York, 1962).
9. Gorlin, S.M. and Slezinger, I.I., "Wind Tunnels and Instrumentation," Izdatel'stvo "Nauka," Moskva, 1964.

10. Albertson, C.W. and Bauserman Jr., W.A., "Total Temperature Probes for High-Temperature Hypersonic Boundary Layer Measurements," NASA TM 4407, 1993.
11. Reardon, J., Schetz, J.A., and Lowe, K.T., "Computational Modeling of Total-Temperature Probes," *Journal of Thermophysics and Heat Transfer* 31(3):609-620, 2017, doi:10.2514/1.T4991.
12. Kraus, A.D., "Sixty-Five Years of Extended Surface Technology (1922-1987)," *Applied Mechanics Reviews* 41:621-364, 1988, doi:10.1115/1.3151910.
13. Schetz, J.A., Vincent, T., and Lowe, K.T., "Analysis of Base-Cooled Total Temperature Probes with Radiation," ASME Paper IMECE 2016-65130, 2016.
14. Siegel, R. and Howell, J.R., *Thermal Radiation Heat Transfer*, (Washington, DC, Hemisphere Publishing Corp., 1992), ISBN: 0891162712.
15. Shouman, A.R., "An Exact General Solution for the Temperature Distribution and Composite Radiation Convection Heat Exchange along a Constant Cross-Sectional Area Fin," *Quart. Appl. Math.* 25:458-462, 1968, doi:10.1090/qam/99882.
16. Asadi, M. and Khoshkho, R.H., "Temperature Distribution along a Constant Cross Sectional Area Fin," *International Journal of Mechanics and Applications* 3:131-137, 2013, doi:10.5923/j.mechanics.20130305.04.
17. Sadri, S., Raveshi, M.R., and Amiri, S., "Efficiency Analysis of Straight Fin with Variable Heat Transfer Coefficient and Thermal Conductivity," *J. Mech. Sci. Tech* 26:1283-1290, 2012, doi:10.1007/s12206-012-0202-4.
18. Ascher, U.M., Mattheij, R., and Russel, R., *Numerical Solution of Boundary Value Problems for Ordinary Differential Equations*, Second Edition, (Philadelphia, SIAM, 1995), ISBN: 978-0-89871-354-1.
19. Huang, M.J. and Chen, C.K., "Conjugate Mixed Convection and Conduction Heat Transfer along a Vertical Circular Pin," *Int. J. Heat Mass Transfer* 28:523, 1985, doi:10.1016/0017-9310(85)90174-7.
20. Kraus, D.A., Aziz, D., and Welty, J.R., *Extended Surface Heat Transfer*, (New York, John Wiley & Sons, 2001), doi:10.1002/9780470172582.
21. Powell, R.W., Ho, C.Y., and Liley, P.E.. "Thermal Conductivity of Selected Materials," Tech. Report, Thermophysical Properties Research Center, West Lafayette, 1966 (Print).

5. Analysis of Pin Fins Including Radiation and Transients

The contents of this chapter have been accepted in *Computational Thermal Sciences* (Tyler G. Vincent, Joseph A. Schetz, and K. Todd Lowe. "Analysis of Pin Fins Including Radiation and Transients").

Significant portions were previously presented as Tyler G. Vincent, Joseph A. Schetz, and K. Todd Lowe. "Analysis of Pin Fins Including Radiation." In *13th International Conference on Heat Transfer, Fluid Mechanics and Thermodynamics 2017*. uri: `http://hdl.handle.net/2263/62422`.

ANALYSIS OF PIN FINS INCLUDING RADIATION AND TRANSIENTS

Vincent T.G., Schetz J.A.* and Lowe K.T.
*Author for correspondence
Departments of Aerospace & Ocean and Mechanical Engineering,
Virginia Tech,
Blacksburg, VA 24061,
USA,
E-mail: ptiger@vt.edu

ABSTRACT
The design of fins for heat transfer enhancement remains a topic of great interest in a number of engineering areas and applications, despite an extensive literature on the subject. One can apply detailed computational methods for simultaneous convection, conduction and radiation heat transfer, but such approaches are not suitable for rapid, routine design studies. So, there is still a place for approximate analytical and low-cost numerical methods, and that is the subject of the first part of this paper. Developed here is an enhanced, low-order model (LOM) that extends traditional pin fin analysis to include a more realistic radiation treatment and that further allows temperature dependent thermal conductivity, variable heat transfer coefficients over the tip and sides of the fin with variable area distribution, and transient response. The LOM solution procedure was packaged in a *MATLAB* code intended for routine use by designers and analysts. Next, a novel reduced-order modelling (ROM) technique was developed and illustrated, which couples heat transfer coefficient information from a computational fluid dynamics/conjugate heat transfer (CFD/CHT) simulation with the new LOM, boasting significantly reduced run times with comparable accuracy to the original full-scale simulations.

NOMENCLATURE

$A(x)$	[m^2]	cross-sectional area of fin
c	[J/kgK]	specific heat capacity
CFD/CHT	[-]	computational fluid dynamics/ conjugate heat transfer
$d(x)$	[m]	diameter of fin
F	[-]	radiation view factor from fin to surroundings
G	[$1/m^2K^4$]	$=2/5(\sigma\varepsilon P/kA)$
$h(x,t)$	[W/m^2K]	convection heat transfer coefficient on fin side
h_{tip}	[W/m^2K]	convection heat transfer coefficient on fin tip
i	[-]	node index
$k(T)$	[W/mK]	thermal conductivity
k_0	[W/mK]	reference thermal conductivity
k_1	[W/mK^2]	slope of linear thermal conductivity
L	[m]	length of the fin
LOM	[-]	enhanced low-order model
m	[1/m]	$=(hP/kA)^{1/2}$
n	[-]	number of nodes

ODE	[-]	ordinary differential equation
P(x)	[m]	partial differential equation
PDE	[-]	partial differential equation
$\dot{q}(x,t)$	[W/m^3]	internal heat generation
Q_b	[W/m^2]	base heat transfer
t	[s]	time
$T(x,t)$	[K]	temperature
T_0	[K]	reference temperature
T_f	[K]	fluid temperature
T_b	[K]	base temperature
T_{surr}	[K]	surroundings temperature
x	[m]	base to tip coordinate
α	[-]	absorptivity
ε	[-]	emissivity
η_f	[-]	fin efficiency
ρ	[kg/m^3]	density
σ	[WK^4/m^2]	Stefan-Boltzmann constant

INTRODUCTION

The use of fins to enhance heat transfer is ubiquitous in industrial and consumer applications and even in nature (Farlow et al., 1976; Hill and Veghte, 1976). So, the design and analysis of fins for heat transfer enhancement remains a topic of great interest, despite a broad and deep prior literature on the subject (e.g. Kraus, 1988; Kraus et al., 2001). Prediction of the combined effects of convection, conduction and radiation remains an area of concern, and that is made more difficult when further considering transient response. For high heat transfer fins, it is common for the temperature of the convecting fluid to differ greatly from that of the fin base, leading to substantial axial conduction within the fin. Additionally, radiation plays a significant role in cases where absolute temperatures are high or the fin temperature varies significantly from its surroundings. It is also important to consider the fin's transient response in a case with time-varying operating conditions. For the evaluation of fin performance either under steady or time-varying conditions, one can apply detailed computational methods for simultaneous convection, conduction and radiation heat transfer. *ANSYS Fluent* has been used for related studies (Reardon et al., 2017), but such approaches are not suitable for rapid, routine design studies. So, there is still a place for approximate analytic and numerical methods, and that is the topic of the first part of this paper.

Some early analytical methods treated a so-called "pin fin" (a straight or tapered rod projecting from a wall) with combined convection and conduction. Kraus (1988) provides a very thorough review of the literature. While useful, these treatments were quite restrictive in a number of ways. Some, but not all, of the restrictions are covered in the so-called Murray-Gardner-Kern Assumptions (Kraus, 1988): (1) The heat flow and temperature distribution are steady in time, (2) The fin material is homogeneous and isotropic, (3) There are no heat sources in the fin, (4) The heat flow to or from the fin surface is proportional to the temperature difference between the surface and the surrounding fluid, (5) The thermal conductivity of the fin is constant, (6) The heat transfer coefficient is the same over the fin surface, (7) The temperature of the surrounding fluid is uniform, (8) The temperature of the base of the fin is uniform, (9) Temperature gradients normal

to the surface may be neglected (1-D assumption), (10) The heat transferred through the tip of the fin is negligible compared to that passing through the sides, (11) The joint between the fin and the prime surface offers no bond or contact resistance. One can add an additional common assumption: (12) Radiation is neglected, or radiation is treated without convection.

Analyses of the pin fin for heat transfer enhancement have also been used to study total temperature probes where the fluid flow is directed towards the tip of the fin. That was the topic of some of our recent work (Schetz et al., 2016).

It is very difficult to treat radiation from/to the fin within a purely analytical method, so the only available solutions in the literature are limited to very restrictive cases. Here, we have extended the pin fin analysis to include a more realistic radiation treatment, as well as allowed for variable thermal conductivity, variable heat transfer coefficients over the tip and sides of the fin, continuously varying cross-sectional fin area, and transient response to time-dependent boundary conditions.

The usual pin fin analyses in the literature all assume prior knowledge of the convection heat transfer coefficient, and that presents a severe limitation. The most straight forward approach is to simply divert to complex CFD/CHT methods, but that is time consuming and costly. We have pursued a hybrid approach that uses a very limited number of CFD/CHT simulations to provide heat transfer coefficient inputs that can be used with an extended LOM such as developed in this paper to simulate cases over a much broader parameter space.

DISCUSSION OF PRIOR ANALYSES

While many forms of the 1-D conducting fin governing equation exist, many rely heavily on the simplifying assumptions of Murray-Gardner-Kern (Kraus, 1988) mentioned in the previous section. In an attempt to relax many of those assumptions, one generalized form can be constructed allowing for a spatially varying convection heat transfer coefficient, temperature dependent thermal conductivity, axial variation in fin cross sectional area, radiation effects, internal heat generation, and transient response (eqn. (1)). Of high significance is the upholding of the 1-D conduction assumption, which neglects accounting of temperature gradients in the fin radial direction.

$$\frac{\partial}{\partial x}\left[k(T)A(x)\frac{\partial T(x,t)}{\partial x}\right] = h(x,t)P(x)\left[T(x,t)-T_f\right] + \sigma FP(x)\left[\varepsilon T^4(x,t)-\alpha T_{surr}^4\right] + \dot{q}(x,t) + \rho c\frac{\partial T(x,t)}{\partial t} \quad (1)$$

The term on the left-hand-side quantifies the change in axial conduction along a differential fin element. That is balanced by the transfer of heat via convection and radiation into the sides of the fin element and internal heat generation under steady conditions, the first three terms on the right hand side, respectively. Here, radiation is treated with a single, uniform surroundings temperature (T_{surr}), further allowing for view factor input (F), and independent variation in the fin emissivity (ε) and the surrounding's absorptivity (α). Often, radiation boundary conditions are not known in

detail. Therefore, this level of detail in the treatment of radiation can be useful, especially when considering the capability to rapidly vary these conditions to get fin response over a wide range of radiation environments during a design process. The final term represents the unsteady accumulation or depletion of thermal energy within the fin. Consequently, as more of the classic fin model assumptions are relaxed, as is the case in eqn. (1), the availability of exact analytic solutions decreases.

Assuming, for the moment, a constant cross-section area (and hence perimeter), h and k constant, $\varepsilon=\alpha$ (grey bodies), F=1.0, steady state and no internal heating, the governing equation is:

$$\frac{d^2T(x)}{dx^2} = \frac{hP}{kA}\left[T(x) - T_f\right] + \frac{\sigma\varepsilon P}{kA}\left[T^4(x) - T_{surr}^4\right] \tag{1a}$$

The simplest cases neglect radiation, and the equation above reduces further to a linear ODE with a well-known solution (Kraus, 1988), but the assumption of constant h is often unrealistic. It is an easy matter to extend the solution to allow $h_{tip} \neq h$ by modifying the boundary condition at $x=L$. The resulting solution gives (Schetz et al., 2016):

$$\frac{T(x) - T_f}{T_b - T_f} = \frac{\cosh\big(m(L-x)\big) + \frac{h_{tip}}{mk}\sinh\big(m(L-x)\big)}{\cosh(mL) + \frac{h_{tip}}{mk}\sinh(mL)}$$

$$Q_b = \sqrt{hPkA}\big(T_b - T_f\big)\frac{\sinh(mL) + \left(\frac{h_{tip}}{mk}\right)\cosh(mL)}{\cosh(mL) + \left(\frac{h_{tip}}{mL}\right)\sinh(mL)} \tag{2}$$

where Q_b is the heat transfer at the base.

Consider next prior treatments of the pin fin problem including radiation using eqn. (1a). The boundary condition at $x=L$ is now

$$h_{tip}\left[T(L) - T_f\right] + \sigma\varepsilon\left[T(L)^4 - T_{surr}^4\right] = -k\left[\frac{dT}{dx}\right]_{x=L} \tag{3}$$

Since eqn. (1a) is a non-linear ODE, analytical solutions are only obtained for restrictive, limiting cases. If $T_{surr}=T_f$, multiply eqn. (1a) by dT/dx and integrate once to get (Siegel and Howell, 1992):

$$\frac{1}{2}\left(\frac{dT}{dx}\right)^2 = \frac{hP}{kA}\left[\frac{1}{2}T^2 - TT_f\right] + \frac{\sigma\varepsilon P}{kA}\left[\frac{1}{5}T^5 - TT_f^4\right] + C \tag{4}$$

For the very restrictive case where $T_f=0$ and a very long fin so that both $T(L)$ and $(dT/dx)_{x=L}\rightarrow 0$, $C=0$, and:

$$\frac{dT}{dx} = \pm\sqrt{\frac{2}{5}\frac{\sigma\varepsilon P}{kA}T^5 + \frac{hP}{kA}T^2} \tag{5}$$

One selects the appropriate sign for the expected behavior of $dT/$dx. For example, if $T(x)$ is decreasing along the fin, the minus sign is appropriate. Using $T(0)=T_b$, integrate to obtain:

$$\int_0^x dx = -\int_{T_b}^{T} \frac{dT}{T\left[\frac{2}{5}\left(\frac{\sigma\varepsilon P}{kA}\right)T^3 + \frac{hP}{kA}\right]} \tag{6}$$

Further integration yields the closed form solution (Siegel and Howell, 1992):

$$x = \frac{1}{3m}\left[ln\frac{\sqrt{GT_b^3 + m^2} - m}{\sqrt{GT_b^3 + m^2 + m}} - ln\frac{\sqrt{GT^3 + m^2} - m}{\sqrt{GT^3 + m^2 + m}}\right] \tag{7}$$

where $G=2/5(\sigma\varepsilon P/kA)$. Even though this solution is only obtained following very restrictive assumptions, it is still useful by displaying the key lumped parameters, G and m.

One can find interesting solutions for other restricted cases in the literature, all for $h_{tip}=h$ or an insulated tip, $(dT/dx)_{x=L}\rightarrow 0$. See for example Shouman (1967) and Asadi and Khoshkho (2013). Generally, numerical evaluation of complex integrals is required even for such cases.

Cases with variable cross-section area, $A(x)$, and variable heat transfer coefficient, $h(x)$, (except for the simplest case of $h_{tip} \neq h$) are much more complicated. See Kraus et al. (2001) for a thorough exposition of available results. Sadri et al. (2012) considered variable $k(T)$ and simplified $h(x)$ variations. There is much less work in the literature for cases with varying $A(x)$ and $h(x)$ in the presence of radiation.

Based on the discussions above, one may conclude that there is no suitable analytic solution for general application to the pin fin case, certainly for unsteady cases. That conclusion motivated the work described in the following sections.

ENHANCED LOW-ORDER MODEL – NUMERICAL METHODS

It is our goal to implement a numerical solution (which we will refer to as the enhanced low-order model or LOM) that generalizes the thermal behaviour of a 1-D, conducting, pin fin with radiation allowing for transient response. This means allowing for the heat transfer coefficient to vary along the fin length and with time, $h(x,t)$, and allowing for area variation along the fin length, $A(x)$. For cases with large thermal gradients along the fin, model accuracy can be further improved by replacing the constant solid conductivity assumption with a local temperature-dependent conductivity, $k(T)$. Internal heat generation will not be explored in the latter sections of this paper and thus is neglected, however it is a simple matter to include internal heat generation in further analyses. Thus, the governing differential equation considered here takes the form:

$$\frac{\partial}{\partial x}\left[k(T)A(x)\frac{\partial T(x,t)}{\partial x}\right] = h(x,t)P(x)\left[T(x,t)-T_f\right] + \sigma F P(x)\left[\varepsilon T^4(x,t) - \alpha T_{surr}^4\right] + \rho c\frac{\partial T(x,t)}{\partial t} \quad (8)$$

The problem further requires two boundary conditions. At $x = 0, T(0,t) = T_b$ and at x = L:

$$\left.\frac{\partial T(x,t)}{\partial x}\right|_{x=L} = \frac{-h_{tip}}{k\left(T(L,t)\right)}\left(T(L,t)-T_f\right) - \frac{\sigma F}{k\left(T(L,t)\right)}\left(\varepsilon T(L,t)^4 - \alpha T_{surr}^4\right) \quad (9)$$

In problems seeking transient response, an initial temperature condition, $T(x, t = 0)$, throughout the entire fin is also required.

Consider first steady cases. This is a "two-point boundary value problem" since the two required boundary conditions are applied at two values of the independent variable, *x*. There are three main ways to treat such problems (Ascher et al., 1995): *Shooting, Finite Difference* and *Projections.* In previous low-order model work with constant h, k and A (Schetz et al., 2016), the *Shooting* method was employed. It was observed that as the radiation effects in a problem grew more intense or the boundary condition to match became more complicated, as in eqn. (9), the *Shooting* method required more care to ensure proper convergence. Mabood et al. (2013) used the *Optimal Homotopy Asymptotic Method (OHAM)* for the solution of the two-point boundary value problem involving a heat-generating fin with convection and radiation, creating an analytic series solution without the need for linearization or discretization. While their solutions were in good agreement with existing numerical approaches, this approach was found to be too limiting for the more general cases of interest in this paper. Here, we have selected an implicit *Finite Difference* approach, because it was found to be more robust.

The local first and second spatial derivatives of temperature and geometry are approximated using a second-order accurate, 5-point, central-differencing scheme, derived to allow for non-uniform element lengths. Non-uniform gridding helps improve accuracy with a reduction in computational cost by allowing for finer grids near regions of large spatial gradients (thermal, geometric, or film coefficient) without the need to refine regions of small gradients where coarser grids are adequate. Temporal derivatives are approximated using a second-order accurate, 3-point backward-differencing scheme, with the time step size held constant. Refer to Appendix A for a more detailed discussion regarding discretization of the governing equations used for this paper.

The implicit *Finite Difference* method requires N equations for N node temperatures to solve for the temperature at each node along the fin. At nodes $i = 1$ and $i = N$ (see Figure A1), the two boundary conditions in eqn. (9) are applied. For each of the nodes $i = 2$ through $(N - 1)$, the discrete form of eqn. (8) is used. Due to the non-linearity of the governing equation with radiation, an iterative approach is required to solve the system of equations. MATLAB's *fsolve* function is useful for iteratively solving such a system of non-linear equations (MATLAB, 2018).

Following evaluation of the temperature solution, one can compute fin performance. It is common to represent the performance of a fin using the fin efficiency, η_f, which is defined as the ratio of

actual fin heat transfer rate, Q_b, to the idealized maximum amount of heat transfer through the base, Q_{max}, assuming the fin is entirely at its specified base temperature (Kraus et al., 2001):

$$\eta_f = \frac{Q_b}{Q_{\max}} \tag{10}$$

The fin heat transfer rate can be determined by calculating the conduction heat transfer at the fin base using a numerically estimated temperature gradient from the temperature solution. To achieve a reasonable level of accuracy, a second-order accurate, 4-point forward-differencing scheme was used for the base temperature gradient. It is critical that we consider how the definition of fin efficiency handles the addition of radiation heat transfer. If radiation affects the fin heat transfer rate (i.e. $\varepsilon \neq 0$), it is logical to adjust the denominator of fin efficiency to include idealized radiation to the surroundings. Further generalizing fin efficiency to account for variable film coefficient and geometry gives:

$$\eta_f = \frac{Q_b}{\left(T_b - T_f\right)\int_{x=0}^{L} hPdx + \sigma F(\varepsilon T_b^4 - \alpha T_{surr}^4)\int_{x=0}^{L} Pdx} \tag{11}$$

If radiation is neglected, eqn. (11) simplifies to the standard definition of fin efficiency in eqn. (10) for a conducting fin with convection.

ENHANCED LOW-ORDER MODEL – VERIFICATION AND VALIDATION

In this section, we have conducted a verification and validation (V&V) exercise to demonstrate the accuracy of our method. This has involved comparing the Enhanced LOM numerical results with those from exact solutions for limiting cases and experiments from the literature and simulations with a commercial 3-D thermal solver. The exact solutions for those limiting cases, experiments and thermal solvers have proven to well replicate physical reality. By verifying that the Enhanced LOM results match those materials, we validate our method by extension. The V&V cases presented here were carefully selected to independently prove the Enhanced LOM treatment of the relaxed classical fin restrictions including the treatment of radiation, axial variation in cross-section area, spatially varying film coefficient, variable thermal conductivity, and forced unsteady behavior. Table 1 provides a summary of all V&V cases performed, including all necessary model input parameters and V&V strategy. All cases involving radiation are evaluated with a view factor of unity (F=1.0). For V&V Cases 1-5, 1000-node grids were used, exactly matching the exact analytic solutions when available, which provided assurance of a grid independent solution. However, a more formal grid independence study was performed for Cases 6(a) and 6(b), and the results are presented later in this section.

V&V Cases 1 and 2: steady, constant cross-section area fins with constant thermal conductivity, k, and heat transfer coefficient, h

Cases 1 and 2 consider pin fins with constant cross-section area, A, and heat transfer coefficient, h, (except for the simplest case of $h_{tip} \neq h$). The first case has the exact solution in eqn. (2) where radiation is neglected. Using eqn. (2) with the provided test case conditions, one finds that the total

fin heat transfer, Q_b, is -4.4W for this simulated fin with a cooled base in a high convection environment. The result from the Enhanced LOM using 1000 nodes yields a total fin heat transfer that matches the exact solution. The second case has the exact solution given here as eqn. (7), which allows for radiation, but requires assuming $T_f = T_{surr} = 0$ and a very long fin so that both $T(L)$ and $(dT/dx)_{x=L} \rightarrow 0$. It is obvious that these are severe restrictions, but one can still use the predictions for numerical model V&V. In this case, radiation is enhanced by choosing $T_b = 1500$K and reducing convection with $h = 50$ W/m^{2}K and an adiabatic tip ($h_{tip}/h = 0$). The temperature decay is also likely slower, so L was increased to 100 mm to better simulate the infinite length required for the analytic solution. The analytical solution in eq. (7) for this case gives $x = 8.37$ mm for $T(x) = 500$K, and the numerical result agrees very well with that, thus proving the LOM for cases with radiation. Neglecting radiation leads to an error of more than 100K at that location.

V&V case 3: steady, variable cross-section area fins with constant thermal conductivity, k, and heat transfer coefficient, h

In many heat transfer applications, it is desirable to design a pin fin with a variable cross sectional area along its length, $A(x)$. This may be motivated by several factors including the fin's structural capabilities, volumetric constraints, or various heat transfer requirements.

For the case of constant heat transfer coefficient without radiation, several analytical solutions exist in the literature for fins with lengthwise area variation (Kraus et al., 2001). For V&V of variable area incorporation into the LOM, the temperature solution for a conical fin with the provided Case 3 parameters was computed using the numerical model. Subsequently, the fin efficiency was calculated using eqn. (11), yielding $\eta_f = 0.34$. An exact, analytical solution for the fin efficiency of a conical fin is:

$$\eta_f = \frac{2}{mL} \frac{I_2(2mL)}{I_1(2mL)} \tag{12}$$

where I_1 and I_2 are modified Bessel functions of the first kind. The evaluation of the analytic fin efficiency (eqn. (12)) using Case 3 input parameters showed excellent agreement with the LOM solution, thus proving the LOM for variable area fins.

V&V Cases 4(a) and 4(b): steady, constant cross-section area fins with constant thermal conductivity, k, and variable heat transfer coefficient, h(x)

There has long been considerable interest in fin analyses that permit the heat transfer coefficient to vary along the length of the fin, $h(x)$, because that is the situation in most practical applications. See for example Huang and Chen (1985) and the extensive review of older work in Kraus (1988). Unfortunately, there is no simple, analytic solution with variable heat transfer coefficient, even without radiation, available that can be used to directly compare to the LOM. For V&V of variable heat transfer coefficient, Cases 4(a) and 4(b), with constant $h(x)$ and linearly varying $h(x)$, respectively, were solved using the LOM, and the relationship of the resulting temperature profiles and fin efficiencies were compared to trends found in the literature. A low value of the film coefficient near the base and a high value near the tip as exhibited in Case 4(b) can be expected in many practical situations. Case 4(a) is intended to represent the solution if the model did not allow for variable $h(x)$ and instead, required a representative uniform value of h. In this case (4(a)), h is evaluated as the surface averaged $h(x)$ from the linearly varying Case 4(b). Figure 1 shows the

LOM-predicted temperature profiles for Cases 4(a) and 4(b). Both cases excluded radiation. Here, we found $\eta_f = 0.29$ for the constant *h* assumption and 0.17 for the linear *h(x)*. This behavior of a constant *h* assumption over-predicting η_f is in agreement with the literature (Huang and Chen, 1985) for other assumed *h(x)* cases. We take this as at least partial V&V of allowing for spatially varying film coefficient the LOM.

V&V case 5: unsteady, constant cross-section area fins with constant thermal conductivity, k, and heat transfer coefficient, h

The analysis of unsteady pin fins has a comparable number of applications to that of steady fins, therefore that has been the direct focus of many exact, unsteady, fin solutions (Donaldson and Shouman, 1972; Aziz and Na, 1980; Mao and Rooke, 1994; Suryanarayana, 1976). One such solution (Donaldson and Shouman, 1972) utilizes the method of separation of variables to solve for the unsteady temperature response in a fin initially at a uniform temperature T_i, subjected to a step change in base temperature at $t = 0$ seconds:

$$T(x,t) = T_b + (T_b - T_f)\left[\frac{\cosh\left((L-x)\sqrt{\frac{4h}{kd}}\right)}{\cosh\left(L\sqrt{\frac{4h}{kd}}\right)} - 1\right] + \frac{2}{L}\sum_{n=1}^{\infty}\left\{\left[\frac{T_i - T_f}{\lambda_n} - \frac{(T_b - T_f)\lambda_n}{\left(\frac{4h}{kd} + \lambda_n^2\right)}\right] \times \exp\left[-\frac{k}{\rho c}\left(\frac{4h}{kd} + \lambda_n^2\right)t\right]\sin(\lambda_n x)\right\} \quad (13)$$

where $\lambda_n = (2n-1)\pi/2L$ and $n = 1,2,\ldots,\infty$. For model V&V of transient response, we computed the unsteady temperature solution using both the exact solution in eqn. (13) and the LOM for V&V Case 5. The fin is initially at a uniform temperature T_i= 300K and at t = 0 seconds, T_b is stepped to 500K. The numerical LOM solution was computed using a time step of 1×10^{-3} seconds. A comparison of the exact and LOM solution, shown in Figure 2 at many time steps, shows excellent agreement, thus proving that the LOM is capable of accurately evaluating unsteady solutions.

V&V Cases 6(a) and 6(b): steady, variable cross-section area fins with temperature dependent thermal conductivity, k(T), and variable heat transfer coefficient, h(x)

For V&V Cases 1-4, many of the classical fin simplifying assumptions were independently relaxed including fins with the influence of radiation and variable cross-section area, thermal conductivity, and heat transfer coefficient. Of course, the aim of the development of this Enhanced LOM approach is to gain the ability to predict fin performance with any combination of these effects, providing a more powerful tool for more realistic fin design studies. Cases 6(a) and 6(b) include all of the aforementioned effects, thus an exact solution does not exist. For V&V purposes, ANSYS Fluent, a commercial Computational Fluid Dynamics (CFD) code with Conjugate Heat Transfer (CHT) capabilities is used to produce solutions for Cases 6(a) and 6(b) for comparison to the LOM solutions. The critical difference between the LOM and Fluent solvers is the LOM only spatially discretizes axially along the fin, while Fluent creates a mesh

with elements spanning both axially and radially within the fin. Therefore, these cases also serve to test the assumption of one-dimensionality present in the LOM.

The specific case input parameters can be found in Table 1 for Cases 6(a) and 6(b). The top of Figure 3 shows the fin geometry (note the axis of revolution represented by segment C-D), which is comprised of a long uniform area section (segment A-B) and a hemi-spherical tip (segment B-D). A fixed temperature boundary condition T_b=300K was applied to the fin base, while convecting boundary conditions of 1000 W/m^{2}K and 3000 W/m^{2}K were applied to the fin side and tip segments, respectively. While Case 6(a) does not include radiation, Case 6(b) further includes black body radiation ($\varepsilon = \alpha = 1$) to the surroundings at T_{surr}=1000K. An axisymmetric approximation was applied in the Fluent solution, since no circumferential variations are expected. Figure 3 also provides a visualization of the grid resolutions used in this V&V study. A uniformly sized, 2-D tetrahedral meshing method was used to generate the grids for the Fluent solutions. For proper comparison of solutions between Fluent and the LOM, the exact location of the surface nodes the 2-D Fluent mesh along segment A-B-D were used as the node locations for the 1-D LOM solution. A comparison of the coarse 1-D and 2-D grids used are illustrated in Figure 3. For both Case 6(a) without radiation and Case 6(b) with radiation, all three grid resolutions were used to compute the temperature solutions. The fin base heat flux and tip temperature for each computation was computed, and the results can be found in Table 2.

For proper grid independence, one must ensure a numerical solution does not change depending on the level of grid refinement. A comparison of the base heat flux and tip temperature values predicted by the Fluent solver shows virtually no change, despite the extreme variation in grid refinement. This strongly suggests that even the coarsest 2-D Fluent mesh is adequate for accurate thermal predictions in this fin study. While comparison of the base heat flux and tip temperature values predicted by the 1-D LOM presented here shows a slight variation, the solution differences between the coarsest and finest grids can be considered negligible (less than 0.5% variation), thus the conclusion of solution convergence using even the coarsest LOM grid is the same.

A comparison of temperature solutions between Fluent and the LOM shown in Figure 4 using the coarsest grid reveals that the LOM somewhat under-predicts the fin temperature for both cases with and without radiation. This difference is the result of allowing only 1-D conduction in the LOM, in a case where high geometric variations exist. While, this restriction is expected to introduce error in the fin performance predictions using the LOM, this error is anticipated to be small (less than 1% variation in the tip temperatures for this example), and use of the LOM for similar cases can be further justified by the significant computational savings.

STEADY EXAMPLES USING ENHANCED LOW-ORDER MODEL

In this section, several fundamental, steady, examples of pin fin solutions are presented to investigate the effects of varying the major fin performance parameters, in both radiative and non-radiative environments using the enhanced LOM. These parameters include fin aspect ratio (*L/d*), fin shape, film coefficient distribution, and material thermal property variations. The LOM transient capabilities are further explored in the next section to analyse a more practical engineering application involving a pin fin.

Constant cross-section area fins with constant heat transfer coefficient
An engineer is always interested in the effects of fin length, and one can investigate that with the tools developed here. Consider cylindrical fins with length to diameter ratio, L/d, ranging from 1.0 to 10.0 under the conditions presented in Figure 5, with diameter fixed at d = 1mm. To emphasize the impact of radiation, we used a side film coefficient of h = 500 W/m^{2}K. Results for the fin base heat transfer for each fin length are given in Figure 5. The influence of conduction to the cooled base reduces the fin temperature as the fin becomes shorter which increases the local heat transfer rate into the sides of the fin, but the smaller overall surface area drives total fin heat transfer down. Also, one can observe that there is a point at which further increasing the fin length no longer improves heat transfer rate. Lastly, it can be seen that the effects of radiation are diminished as the fin becomes shorter.

Variable cross-section area fins with constant heat transfer coefficient over the surface
Another interesting way to alter pin fin performance is to alter the fin shape. Changing the fin diameter as a function of the fin length allows the designer to control the behavior of the temperature profile. To investigate this effect, compare the temperature solution for three fins all with a base diameter d = *1mm* and L = *10mm* with differing profiles: cylindrical, conical, and convex parabolic as shown in Figure 6a. Setting T_b= 300K, T_f = 1000K, T_{surr} = 300K, h = 100 W/m^{2}K and h_{tip}/h = 0.0, we can compare the fin thermal response as a function of position as shown in Figure 6b.

It is apparent that as the tip becomes more slender due to the profile shape definition, the tip temperature reaches closer to the surrounding fluid temperature (T(L) = 723K, 757K and 990K for the cylindrical, conical and parabolic fins without radiation, respectively). By accounting for radiation to the cooler surroundings, the fin temperatures can be seen to drop as expected. Further investigation of the parabolic fin solution shows only a 2% discrepancy in the total fin heat transfer through the base when neglecting radiation (-0.59W with radiation and -0.60W without). However, more notable is a 203K reduction in temperature at the tip of the parabolic fin when compared with the solution without radiation. This tip temperature discrepancy would be easily overlooked if only base heat transfer rates were investigated. Thus, a quick, yet accurate calculation of the tip temperature can be valuable if fluid temperatures are near the melting point of the fin material.

Variable cross-section area fins with variable heat transfer coefficient over the surface and temperature-dependent thermal conductivity
An exhaustive literature review of 1-D pin fin solutions showed relatively little consideration with regard to varying thermal conductivity based on local temperature. A constant thermal conductivity assumption can prove reasonably accurate if the temperature gradients along the fin are small. However, in cases where the fin base is significantly different from the surrounding fluid, large thermal gradients can exist along the fin length. In extreme cases, temperatures gradients can exist on the order of 1000K per inch (Englerth, 2015). It is for such cases that relaxing the constant thermal conductivity assumption is needed.

Consider now a conical fin made with a material representative of iron. At 300K, iron has $k \approx 80$ W/mK and at 1000K, $k \approx 32.5$ W/mK (Powell et al. 1966). As a first major step towards

temperature dependent thermal properties, assume that k varies in a locally linear manner with temperature as in eqn. (14):

$$k(T) = k_0 + k_1(T - T_0) \tag{14}$$

For iron, we may approximate $k(T)$ as linear using k_0 = 80 W/mK at a reference temperature T_0 = 300K and slope k_1= -0.0679 W/mK^2. To utilize the full generality of our numerical approach, we may apply a non-uniform film coefficient profile along the side of the fin, which varies linearly from $h(x=0)$ = 0 W/m^{2}K to $h(x=L)$ = 500 W/m^{2}K, as well as compare solutions with and without radiation. Taking base diameter d = 1.0 mm, L = 10 mm, T_b = 300K, T_f = 1000K, T_{surr} = 1000K, we get the results shown in Figure 7. Also shown is the solution if k is assumed constant at the average of the base and fluid temperatures. Note that in our previous examples, the surroundings were cooler than the fluid temperature resulting in radiation away from the fin. This example has surroundings that are equal to the fluid temperature resulting in radiation into the fin.

Due to the large variability in profile temperatures, using conductivity with linear temperature dependence gives a much better result with minimal increase in computational cost compared to constant conductivity. A fin heat transfer rate comparison between results including radiation shows a 25% reduction in magnitude when using $k(T)$ compared to k = constant (-2.08W and -2.80W respectively).

REDUCED ORDER MODELLING OF PIN FINS

The use of the enhanced low-order model (LOM) presented above to predict fin performance requires knowledge of the heat transfer conditions along the surface, namely the local convective film coefficient, including radiative view factors and emissivity/absorptivity of the fin and its surroundings when radiation is involved. Due to challenges associated with experimental measurements of film coefficient on small surfaces common in pin fin applications, it has become common to rely on CFD with conjugate heat transfer (CHT) to capture necessary physical details required for accurate film coefficient determination. In our previous work (Vincent et al., 2017), we developed a novel procedure for integrating CFD/CHT-extracted film coefficient profiles into the LOM as a way to include radiation effects in a fin solution otherwise neglecting radiation, without the need to run additional computationally intensive simulations. The novelty of this method is in the ability of the LOM to non-linearly add the influence of radiation into the solution. This method significantly reduced the computational cost of subsequent calculations and maintained a very high level of accuracy.

In this section, the procedure for CFD/CHT integration with the LOM introduced in Vincent et al. (2017) is extended to develop a reduced order model (ROM) technique for the generalization of single-condition, high fidelity, CFD/CHT simulations, now including unsteady effects. The examples included here show an effective use of the ROM technique for predicting the influence of significant radiative conditions, transient response to a step-change in the base temperature boundary condition, and varying fin material, all from a single steady-state CFD/CHT simulation excluding radiation.

Overview of the Reduced Order Modelling Approach

The goal of a reduced order model is to reduce the number of degrees of freedom (i.e., the model independent variables) in a way that reduces the overall computational expense with an acceptable loss of accuracy. The ROM success, therefore, depends on the ability to identify a surrogate model capable of achieving the desired results. In the context of fins used for heat transfer applications, it is common for the convecting fluid to have highly complex 2-D/3-D flow features. To accurately model the thermal performance of such a fin, it is common practice to employ full 2-D/3-D CFD flow codes with CHT capabilities to model the heat transfer between the convecting fluid and solid boundaries, and radiation to surroundings if applicable. In cases where the fin is slender or the thermal conductivity of the fin is large compared to convection (i.e., Biot Number << 1), the fin begins to develop a 1-D temperature variation axially along the fin. For these cases, the enhanced LOM becomes a perfect surrogate model for the multi-dimensional fin solution, since it reduces the number of independent spatial variables by only considering axial temperature variations.

Once a CFD/CHT solution of a pin fin problem is complete, the film coefficient profile along the surface of the fin can be extracted. If the CFD/CHT solution is axisymmetric, the film coefficient profile produced will be 1-D along the fin axis, feeding nicely into the LOM. If the CFD/CHT solution is three-dimensional (3-D), the film coefficient profile produced will need to be reduced to 1-D before being input into LOM. This can be done by circumferentially averaging at every axial position, ensuring the overall heat transfer of the averaged, 1-D, film coefficient solution matches closely with the full, 3-D, solution.

In the presence of significant forced convection heat transfer conditions, it is reasonable to assume that the film coefficient profile along the surface of the fin is mainly dependent on flow conditions and fin geometry. Consequently, a film coefficient profile can be assumed effectively independent of radiation conditions (T_{surr}, F, ε, and α), fin material properties (k, ρ, and c), base temperature (T_b), or internal heat generation ($\dot{q}$). Therefore, with the film coefficient profile provided by a single CFD/CHT solution, one may change any of the above parameters in the LOM and produce an accurate solution without the need for further detailed CFD/CHT simulations.

The procedure for performing the ROM technique adopted from Vincent et al. (2017) is summarized here:

(1) Perform steady-state CFD/CHT without radiation for the baseline case of interest to get film coefficient profile, $h(x)$.

(2) Using $h(x)$ from (1) as input to the LOM code (discretized version of eqn. (15)), one may further add radiation by specifying T_{surr}, ε and α, add internal heating by specifying $\dot{q}(x,t)$, or change material properties by changing k. Additionally, one could introduce transient effects by changing boundary or initial conditions.

$$\frac{\partial}{\partial x}\left[kA\frac{\partial T(x,t)}{\partial x}\right] = h(x)P(x)\left[T - T_f\right] + \sigma FP(x)[\varepsilon T^4 - \alpha T_{surr}^4] + \rho c\frac{\partial T}{\partial t} + \dot{q}(x,t) \quad (15)$$

The following examples serve to validate the ROM methodology for a realistic fin problem. Specifically, the ROM will be used to predict the change in fin performance due to the inclusion of radiation, change of fin thermal conductivity, and unsteady response to a step change in fin base temperature. A CFD/CHT simulation was performed for each of the presented examples for comparison to the ROM solutions.

Steady CFD/CHT Example

The fin geometry for the ROM study examples is identical to that used in V&V Cases 6(a) and 6(b) found in Table 1. For this case, a fixed thermal conductivity of 28.1 W/mK was chosen for comparison to an example first introduced in Vincent et al. (2017). Unlike the V&V cases where the convective film coefficient is assumed *a priori*, this case uses *ANSYS Fluent* to perform a CFD/CHT simulation to evaluate a more realistic convective film coefficient along the surface for a high velocity fluid directed toward the fin tip and passing axially over the length of the fin towards the base. The fluid domain solution was performed using steady-state Reynolds-averaged Navier-Stokes (RANS) equations with the $k-\omega$ SST turbulence model for closure of the Reynolds stresses. Details of the fin and fluid geometry and boundary conditions can be found in Figure 8 and Table 3.

Based on the grid independence study performed earlier for V&V Cases 6(a) and 6(b), a fin body-sizing equivalent to the coarsest grid was deemed adequate for convergence. The fluid domain elements were created conformal to the fin surface, with 15 layers of prismatic cells surrounding the fin for boundary layer refinement. The remainder of the fluid domain outside of the fluid boundary layer refinement region consisted of an unstructured tetrahedral mesh, with a growth rate of 5%, resulting in a total of 19,166 fluid elements.

The film coefficient profile was extracted from the converged solution as a function of the axial position along the surface of the fin in conjunction with step (1) of the ROM procedure, and that is plotted in Figure 9a, where $x/L = 0$ and 1.0 are the fin base and tip locations, respectively. The elevated film coefficient near the fin tip ($0.95<x/L<1.0$) is a result of flow stagnation, visible in the velocity contours of Figure 9b. The remainder of the fin surface is dominated by the presence of a non-separating, length-wise boundary layer, resulting in a nearly uniform film coefficient distribution over the remainder of the fin. A direct validation of the presented CFD results with experiments is not available, since obtaining accurate film coefficient data on a fin this small is impractical with currently available experimental methods. However, this film coefficient result is in good agreement with the work of Reardon et al. (2017), who consistently observed an elevated fin tip heat transfer coefficient on the order of 3 to 5 times larger than the fin side for a fin in axial flow directed toward the tip. This film coefficient profile can now be input into the LOM code to predict the temperature solution under any variation of parameters mentioned in step (2) of the ROM procedure.

Reduced Order Model V&V

First, to V&V the ROM approach, the ROM solution with the original problem parameters was compared to the original CFD/CHT solution without radiation, as shown in Figure 10. The comparison shows a nice agreement with approximately a 1K difference between solutions at the fin tip. This result confirms the ROM is successfully maintaining high accuracy at a small fraction

of the computational time. For this example, the CFD/CHT solution was performed using a 6-core workstation, taking approximately 6.5 minutes to complete 10,000 solution iterations (achieving a continuity residual of 10^{-8}). The ROM solution on the same workstation, not utilizing parallel capabilities, took approximately 2.5 seconds, showing an impressive 156:1 reduction in computational time.

Adding Radiation using the Reduced Order Model

One use of the ROM technique is to add radiation effects to an existing fin solution without radiation. Following step (2), a new solution including radiation was obtained and plotted in Figure 11 using the film coefficient profile from Figure 9a and specifying $T_{surr} = 1000$ K, $F = 1.0$ and $\varepsilon = \alpha = 1.0$. Here, the new ROM radiation solution (dashed red curve) is compared to the original solution without radiation (dashed black curve). One can see a large increase in overall fin temperature as a result of radiation from the hot surroundings. For further comparison, a second CFD/CHT computation including radiation was performed using the Discrete Ordinates (DO) model in ANSYS Fluent (solid red line). The difference between the full CFD/CHT and ROM solutions including radiation was less than 1.5K, showing that this reduced-order method maintained a very good accuracy.

Changing Fin Material using the Reduced Order Model

In many cases, it is desirable to select a material with a high thermal conductivity to increase overall fin heat transfer, but material properties such as specific heat capacity and density should also be considered if transient response is significant to one's application. Additionally, in extreme applications, material properties/characteristics such as structural capabilities, chemical resistance, and temperature limitations must also be considered. Recall, the fin in the steady CFD/CHT example presented earlier considered a fin with a thermal conductivity of 28.1 W/mK. Imagine a change in the fin material resulting in a new thermal conductivity of 50 W/mK with the same geometry. Similar to the treatment of radiation, the effects of changing fin material can also be handled using the ROM, in this case by simply changing the thermal conductivity in the LOM. The effects of changing fin material while using the original $h(x)$ variation are presented in Figure 12, showing how well the ROM compared to a full CFD/CHT simulation. As expected, the increase in thermal conductivity allows for increased axial conduction along the fin and reduced the overall temperature of the fin.

Transient Response to Base Temperature Change using Reduced Order Model

Encouraged by the ability of the new ROM approach to accurately handle large changes like adding radiation to a CFD/CHT solution without radiation or introducing a different material with different thermal conductivity, we can further extend the approach to transient effects. In some applications using a fin for heat transfer, it is expected that the temperature of the base surface to which the fin is attached can vary with time. Of course, this will induce a transient response within the fin and vary the base heat transfer.

Consider now a hypothetical scenario where the fin in the current example is subjected to an instantaneous step change in the base temperature, $T(x = 0, t = 0)$, from the original 250K up to 300K. Since the fin has a finite mass, it will necessarily take a finite time to reach a new steady-state temperature, thus creating a time-dependent solution. As assumed earlier, variations in the temperature of the fin should have little effect on the film coefficient profile due to high levels of

forced convection, therefore the original time-independent film coefficient profile from Figure 9a should be sufficient for predicting the transient response using the ROM. This step change was implemented both using the ROM and CFD/CHT, and a comparison of the results is shown in Figure 13 at many time steps. The CFD/CHT computation was performed by advancing the original steady state solution with the updated base temperature boundary condition using a time step of 1×10^{-4} seconds. This time step was matched in the ROM solution for a more appropriate comparison.

As expected, following the initial step change in the base temperature, a rapid change in the fin temperature near the base resulted due to close proximity with the altered boundary condition. However, fin temperatures near the tip experience a significant delay due to the fin thermal diffusivity ($k/\rho c_p$), chosen to be 1.187×10^{-5} m^2/s for this sample problem. As time proceeds, the thermal disturbance is sufficiently propagated and begins to affect the temperatures even at the tip, but temperature variation with time begins to decay. Given enough time, the solution would reach steady state. Due to the fluid temperature equalling the base temperature in this example, one would expect the entire fin to reach a uniform temperature of 300K. Visible in the results in Figure 13, the deviation between the temperature solutions from the ROM and CFD/CHT grows slightly as time advances, which is a result of assuming the film coefficient profile will be unaffected as temperatures change. However, making this assumption allowed for a very impressive agreement when considering that on a 6-core workstation, the transient CFD/CHT solution took approximately 2 hours to perform compared to less than a minute using the ROM method.

Recall that the example computation performed in this case employed an axisymmetric approach, which only requires the computational expense of a 2-D problem. Despite the relative simplicity of the computation, the ROM realized a significant reduction in runtime. Further increasing the complexity of the CFD/CHT to a full 3-D problem can add an exponential increase in computational time for the computation, but there is no increase in ROM run time, making the relative cost savings even more impressive.

Transient Response to Combined Base Temperature Change and Sudden Radiation Exposure using the Reduced Order Model

In the previous example, transient response was induced by suddenly changing the base temperature boundary condition of the fin. Another possibility for inducing transient response is by suddenly changing the radiation conditions surrounding the fin. This final example uses the ROM to predict the combined transient response of a simultaneous step base temperature change and an instantaneous exposure to a radiative surrounding. This hypothetical scenario is intended to further showcase the potential of the ROM technique to also accurately predict the combined effects of simultaneously changing multiple problem parameters without needing to run additional CFD/CHT computations.

Recall in the previous example, the base temperature was instantaneously stepped from 250K up to 300K at $t = 0$ seconds. Consider now also suddenly exposing the entire fin to a surrounding temperature of 1000 K, as in the conditions in the steady case with radiation presented earlier. These results were computed using both the ROM and CFD/CHT and a comparison of the results is shown in Figure 14 at many time steps.

As before, a rapid change in the fin temperature near the base propagates toward the tip as time proceeds. Without radiation, the solution from Figure 13 is expected, however one can see a significant difference in the solution presented in Figure 14. The most notable difference is the temperature response near the fin tip. Since radiation heat transfer acts over the entire fin length, the fin tip temperatures are immediately impacted, resulting in a much larger change in temperature over the same duration. Additionally, as expected from the steady case with hot surroundings, the fin becomes warmer than the fluid medium. Despite the additional complexity of this problem, the ROM produces results with very good accuracy to the full CFD/CHT simulation, which took much more computational time and effort.

CONCLUSIONS

In this work, we have created a new enhanced low-order model (LOM) that extends traditional pin fin analysis to include a more realistic radiation treatment, and also variable thermal conductivity, variable heat transfer coefficients over the tip and sides of the fin with variable fin cross-sectional area distribution, and transient response. The LOM solution procedure was packaged in a *MATLAB* code intended for routine use by designers and analysts. The method was verified and validated by comparing results with available analytic solutions for limiting cases and experiments from the literature, and simulations with a commercial thermal solver.

To illustrate the utility of the new LOM tool presented here, a few example cases were selected to study the influences of some key parameters. In particular, radiation on or off, fin length, fin shape, material choices, constant h versus variable $h(x)$, and constant k versus variable $k(T)$ were considered. The tool can be used to thoroughly study these items and any other combinations of parameters that describe the general problem, and all cases can be further analyzed transiently.

Next, a novel, reduced-order modelling (ROM) technique was developed, which integrates heat transfer coefficient information from a complex computational fluid dynamics/conjugate heat transfer (CFD/CHT) simulation with the new LOM, boasting significantly reduced run times with comparable accuracy to the original full-scale simulations. Several examples were included showing the ROM's ability to rapidly and accurately adjust an existing steady-state, no radiation, solution for desired radiation effects, changed material properties, and even predict the transient response to changing the base temperature boundary condition, all without the need to run additional CFD/CHT simulations. This practicality gives a designer more flexibility in defining model parameters when performing high fidelity computations, since many subsequent parameter adjustments can be made using the ROM approach with high accuracy. The method relies on the assumption that convection heat transfer coefficients for a baseline case is largely insensitive to changes in boundary and initial conditions and/or changes in case parameters relative to the baseline. Of course, such an assumption cannot be completely general. But, we have demonstrated that it can be prudently applied to cover rather large changes relative to a baseline case, resulting in very substantial benefits in computational efficiency.

The *MATLAB* enhanced LOM solution code is posted at: http://www.aoe.vt.edu/research/onlinesoft.html/.

REFERENCES

Asadi, M. and Khoshkho, R.H., "Temperature Distribution along a Constant Cross Sectional Area Fin," Int. Journal of Mechanics and Applications, vol. 3, no. 5, pp. 131-137, 2013.

Ascher, U.M., Mattheij, R. and Russel, R., *Numerical Solution of Boundary Value Problems for Ordinary Differential Equations* (2nd Edition), SIAM, 1995.

Aziz, A. and Na, T.Y., "Transient Response of Fins by Coordinate Perturbation Expansion," *Int. J. Heat and Mass Transfer*, Vol. 23, pp. 1695-1698, 1980.

Donaldson, A.B. and Shouman, A.R., "Unsteady-State Temperature Distribution in a Convecting Fin of Constant Area," *Appl. Sci. Res.*, Vol. 26, Nos. 1-2, pp. 75-85, 1972.

Englerth, S.T., An Experimental Conduction Error Calibration Procedure for Cooled Total Temperature Probes, Thesis, Virginia Polytechnic Institute and State University, 2015.

Farlow, J.O., Thompson, C.V. and Rosner, D.E., "Plates of the Dinosaur Stegosaurus: Forced Convection Heat Loss Fins?", *Science*, vol. 192, no. 4244, pp. 1123-1125, 1976.

Hill, R.W. and Veghte, J.H., "Jackrabbit Ears: Surface Temperatures and Vascular Responses," *Science*, Volume 194, Issue 4263, pp. 436-438, 1976.

Huang, M.J. and Chen, C.K., "Conjugate mixed convection and conduction heat transfer along a vertical circular pin," Int. J. Heat Mass Transfer, vol. 28, no. 3, 523, 1985.

Kraus, A.D., "Sixty-five years of extended surface technology (1922–1987)," *Applied Mechanics Reviews*, vol. 41, Issue 9, pp. 621–364, 1988.

Kraus, A.D., Aziz, D. and Welty, J.R., *Extended Surface Heat Transfer*, John Wiley & Sons, 2001.

Mabood, F., Khan, Waqar A., and Ismail, A., "Series Solution for Steady Heat Transfer in a Heat-Generating Fin with Convection and Radiation," Mathematical Problems in Engineering, vol. 2013, Article ID 806873, 7 pages, 2013. DOI: 10.1155/2013/806873

Mao, J. and Rooke, S.,"Transient Analysis of Extended Surfaces with Convective Tip," *Int. Commun. Heat Mass Transf.*, Vol. 21, pp. 85-94, 1994.

MATLAB and Statistics Toolbox Release 2018a, The MathWorks, Inc., Natick, Massachusetts, United States, 2018.

Powell, R.W., Ho, C.Y., and Liley, P.E., *Thermal Conductivity of Selected Materials*. Tech. West Lafayette: Thermophysical Properties Research Center, 1966.

Reardon, J.P., Schetz, J.A. and Lowe, K.T., "Computational Modelling of Total-Temperature Probes," *J. Thermophysics and Heat Transfer*, vol. 31, no. 3, pp. 609-620, 2017.

Sadri, S., Raveshi, M.R. and Amiri, S., "Efficiency analysis of straight fin with variable heat transfer coefficient and thermal conductivity," J. Mech. Sci. Tech, 26 (4), pp. 1283-1290, 2012.

Schetz, J.A., Vincent, T. and Lowe, K., "Analysis of Base-cooled Total temperature Probes with Radiation," *ASME International Mechanical Engineering Congress and Exposition*, vol. 1, 2016. DOI: 10.1115/IMECE2016-65130.

Shouman, A.R., "An Exact General Solution for the Temperature Distribution and Composite Radiation Convection Heat Exchange along a Constant Cross-sectional Area Fin," *Quart. Appl. Math.*, vol. 25, pp. 458-462, 1967.

Siegel, R. and Howell, J.R., *Thermal Radiation Heat Transfer*, Hemisphere Publishing Corp, 1992.

Suryanarayana, N.V., "Transient Response of Straight Fins Part II," *J. Heat Transf.*, Vol. 98, pp. 324-326, 1976.

Vincent, T.G., Schetz J.A. and Lowe, K.T., "Enhanced Low-Order Model with Radiation for Total Temperature Probe Analysis and Design," SAE Technical Paper 2017-01-2047, 2017.

APPENDIX A

Discretization of Unsteady, 1-D, Conducting Pin-Fin Differential Equation

In this paper, we implement a highly generalized solution to the unsteady, 1-D, conducting pin fin with radiation (eqn. (A1)) allowing for variable heat transfer coefficient and area along the fin length, $h(x,t)$ and $A(x)$ respectively, as well as temperature dependent thermal conductivity within the solid, $k(T)$:

$$\frac{\partial}{\partial x}\left[k(T)A(x)\frac{\partial T(x,t)}{\partial x}\right] = h(x,t)P(x)\left[T(x,t)-T_f\right] + \sigma FP(x)[\varepsilon T^4(x,t) - \alpha T_{surr}^4] + \rho c\frac{\partial T(x,t)}{\partial t} \quad (A1)$$

To numerically solve this differential equation, eqn. (A1) must be spatially and temporally discretized. Using the product rule, the left hand side can be expanded:

$$\frac{\partial}{\partial x}\left[k(T)A(x)\frac{\partial T}{\partial x}\right] = A(x)\left(\frac{\partial T}{\partial x}\right)^2\frac{dk(T)}{dT} + k(T)\frac{\partial T}{\partial x}\frac{dA(x)}{dx} + k(T)A_c(x)\frac{\partial^2 T}{\partial x^2} \quad (A2)$$

Both cross section area and temperature have derivatives with respect to axial position, x, and require approximate local spatial derivatives. For improved accuracy, a second-order accurate, 5-point central-difference approximation for the first and second derivatives using the $(i \pm 2)$, $(i \pm 1)$ and $(i)^{th}$ spatial nodes was desired (see Figure A1 for spatial node numbering). Using Taylor Series Expansion (TSE) to extrapolate node temperatures surrounding the $(i)^{th}$ node gives:

$$T_{i-2} = T_i - \left.\frac{\partial T}{\partial x}\right|_i \Delta x_{2L} + \left.\frac{\partial^2 T}{\partial x^2}\right|_i \frac{\Delta x_{2L}^2}{2!} - \left.\frac{\partial^3 T}{\partial x^3}\right|_i \frac{\Delta x_{2L}^3}{3!} + \Theta(\Delta x^4) \quad (A3)$$

$$T_{i+2} = T_i + \left.\frac{\partial T}{\partial x}\right|_i \Delta x_{2R} + \left.\frac{\partial^2 T}{\partial x^2}\right|_i \frac{\Delta x_{2R}^2}{2!} + \left.\frac{\partial^3 T}{\partial x^3}\right|_i \frac{\Delta x_{2R}^3}{3!} + \Theta(\Delta x^4) \quad (A4)$$

$$T_{i-1} = T_i - \left.\frac{\partial T}{\partial x}\right|_i \Delta x_L + \left.\frac{\partial^2 T}{\partial x^2}\right|_i \frac{\Delta x_L^2}{2!} - \left.\frac{\partial^3 T}{\partial x^3}\right|_i \frac{\Delta x_L^3}{3!} + \Theta(\Delta x^4) \quad (A5)$$

$$T_{i+1} = T_i + \left.\frac{\partial T}{\partial x}\right|_i \Delta x_R + \left.\frac{\partial^2 T}{\partial x^2}\right|_i \frac{\Delta x_R^2}{2!} + \left.\frac{\partial^3 T}{\partial x^3}\right|_i \frac{\Delta x_R^3}{3!} + \Theta(\Delta x^4) \quad (A6)$$

where Δx_{2L} and Δx_{2R} are the sum of the two element lengths to the left and right of the $(i)^{th}$ spatial node, respectively and Δx_L and Δx_R are the single element lengths to the left and right of the $(i)^{th}$ spatial node, respectively. This approach accounts for variable element sizes, further allowing solutions with non-uniform gridding.

To approximate $\partial T/\partial x$, one must chose constants a, b, c, and e to multiply eqns. (A3) through (A6), respectively, in order to eliminate the $\partial^2 T/\partial x^2$ terms upon their summation (i.e. satisfy eqn. (A7)):

$$0 = a\frac{\Delta x_{2L}^2}{2!} + b\frac{\Delta x_{2R}^2}{2!} + c\frac{\Delta x_L^2}{2!} + e\frac{\Delta x_R^2}{2!} \quad (A7)$$

One solution is:

$$a = \frac{\Delta x_{2R}^2}{\Delta x_{2L}^2}, \quad b = -1\,, \quad c = \frac{\Delta x_R^2}{\Delta x_L^2}, \quad e = -1 \quad (A8)$$

Taking the sum of the multiplied eqns. (A3) – (A6) and rearranging yields:

$$\left.\frac{\partial T}{\partial x}\right|_i = \frac{aT_{i-2} + cT_{i-1} - (a+b+c+e)T_i + eT_{i+1} + bT_{i+2}}{\Delta x_{2R} b + \Delta x_R e - \Delta x_{2L} a - \Delta x_L c} \quad (A9)$$

Similarly to calculate $\partial^2 T/\partial x^2$, one must determine multipliers a', b', c', and e' to eliminate the $\partial T/\partial x$ terms from the summation of the multiplied eqns. (A3) – (A6):

$$a' = \frac{\Delta x_{2R}}{\Delta x_{2L}}, \quad b' = 1\,, \quad c' = \frac{\Delta x_R}{\Delta x_L}, \quad e' = 1 \quad (A10)$$

resulting in the following solution for $\partial^2 T/\partial x^2$:

$$\left.\frac{\partial^2 T}{\partial x^2}\right|_i = \frac{a'T_{i-2} + c'T_{i-1} - (a' + b' + c' + e')T_i + e'T_{i+1} + b'T_{i+2}}{\frac{1}{2}(\Delta x_{2R}^2 b' + \Delta x_R^2 e' + \Delta x_{2L}^2 a' + \Delta x_L^2 c')} \tag{A11}$$

For spatial nodes $(i = 2)$ and $(i = N - 1)$, where N is the index of the tip node, there are not enough nodes to the left or right for a 5-point central-differencing scheme to approximate gradients. Therefore, a simpler 3-point, central-differencing scheme is used for both the first and second derivatives:

$$\left.\frac{\partial T}{\partial x}\right|_{i=2,N-1} = \frac{cT_{i-1} - (c + e)T_i + eT_{i+1}}{\Delta x_R e - \Delta x_L c} \tag{A12}$$

$$\left.\frac{\partial^2 T}{\partial x^2}\right|_{i=2,N-1} = \frac{c'T_{i-1} - (c' + e')T_i + e'T_{i+1}}{\frac{1}{2}(\Delta x_R^2 e' + \Delta x_L^2 c')} \tag{A13}$$

Since both T and A are functions of x, the numerical approximation for their derivatives will take the same form, thus the solution for $\partial T/\partial x$ can also be used for evaluating dA/dx. For a circular cross-section fin, it is convenient to input diameter, D, at the defined node locations. Therefore, one can define a second-order accurate central difference approximation for dD/dx as:

$$\left.\frac{dD}{dx}\right|_i = \frac{aD_{i-2} + cD_{i-1} - (a + b + c + e)D_i + eD_{i+1} + bD_{i+2}}{\Delta x_{2R} b + \Delta x_R e - \Delta x_{2L} a - \Delta x_L c} \tag{A14}$$

Similarly to the solution for $\partial T/\partial x$, spatial nodes $(i = 2)$ and $(i = N - 1)$ have derivatives approximated using:

$$\left.\frac{dD}{dx}\right|_{i=2,N-1} = \frac{cD_{i-1} - (c + e)D_i + eD_{i+1}}{\Delta x_R e - \Delta x_L c} \tag{A15}$$

$$\left.\frac{d^2 D}{dx^2}\right|_{i=2,N-1} = \frac{c'D_{i-1} - (c' + e')D_i + e'D_{i+1}}{\frac{1}{2}(\Delta x_R^2 e' + \Delta x_L^2 c')} \tag{A16}$$

For a circular cross-section fin, dA/dx is:

$$\left.\frac{dA}{dx}\right|_i = \frac{\pi}{2} D_i \left.\frac{dD(x)}{dx}\right|_i \tag{A17}$$

While it is possible to implement an experimentally determined curve for thermal conductivity as a function of temperature, one may more simply approximate the thermal conductivity as linearly dependent with temperature:

$$k(T) = k_0 + k_1(T - T_0) \tag{A18}$$

This choice was made to ease the burden of implementing further numerical derivatives since:

$$\left.\frac{dk}{dT}\right|_i = k_1 \tag{A19}$$

While linear dependence is a relatively simple model, it manages to greatly improve solution fidelity compared to a constant conductivity model. In cases where linear conductivity is not sufficient, more general finite-difference approaches can be used to evaluate dk/dT, allowing for more complex $k(T)$ behaviors.

For transient cases, one must also approximate the time derivate of temperature, $\partial T/\partial t$. For this study, a second-order, 3-point backward-differencing scheme with a constant, fixed, time step was used for evaluating $\partial T/\partial t$ at the $(i)^{th}$ spatial node and $(j)^{th}$ temporal node:

$$\left.\frac{\partial T}{\partial t}\right|_i^j = \frac{T_i^{(j-2)} - 4T_i^{(j-1)} + 3T_i^{(j)}}{2\Delta t} \tag{A20}$$

When $(j = 2)$, corresponding to the first time step following the initial condition, the time derivative is evaluated using:

$$\left.\frac{\partial T}{\partial t}\right|_i^{j=2} = \frac{T_i^{(2)} - T_i^{(1)}}{\Delta t} \tag{A21}$$

Discretization of Boundary Conditions

Since this is a second order differential equation, two boundary conditions are required. A fixed temperature boundary condition is applied to the fin base:

$$T(x = 0, t) = T_1(t) = T_b(t) \tag{A22}$$

The second boundary condition is enforced at the tip, which states that the conductive heat flux at the tip is equal to the sum of the convective and radiative heat fluxes at the tip:

$$-k\big(T(L,t)\big)\left.\frac{\partial T}{\partial x}\right|_{x=L} = h_{tip}\big(T(L,t) - T_f\big) + \sigma F(\varepsilon T(L,t)^4 - \alpha T_{surr}^4) \tag{A23}$$

For $\partial T/\partial x$ at $x = L$, one can use a second-order accurate, 4-point backward difference scheme (eqns. (A24) and (A25)):

$$a'' = 2\Delta x_{2L}^2 \Delta x_{3L}^2, \quad b'' = -\Delta x_L^2 \Delta x_{3L}^2, \quad c'' = -\Delta x_L^2 \Delta x_{2L}^2 \tag{A24}$$

$$\left.\frac{\partial T}{\partial x}\right|_{x=L} = \frac{(a'' + b'' + c'')T_N - a''T_{N-1} - b''T_{N-2} - c''T_{N-3}}{a''\Delta x_L + b''\Delta x_{2L} + c''\Delta x_{3L}} \tag{A25}$$

For evaluation $\partial T/\partial x$ at $x = 0$ (required for the calculation of fin base heat transfer), one can use a second-order accurate, 4-point forward difference scheme (eqns. (A26) and (A27)):

$$a''' = 2\Delta x_{2R}^2 \Delta x_{3R}^2, \quad b''' = -\Delta x_R^2 \Delta x_{3R}^2, \quad c''' = -\Delta x_R^2 \Delta x_{2R}^2 \tag{A26}$$

$$\left.\frac{\partial T}{\partial x}\right|_{x=L} = \frac{(a''' + b''' + c''')T_1 - a'''T_2 - b'''T_3 - c'''T_4}{-a'''\Delta x_R - b'''\Delta x_{2R} - c'''\Delta x_{3R}} \tag{A27}$$

FIGURES

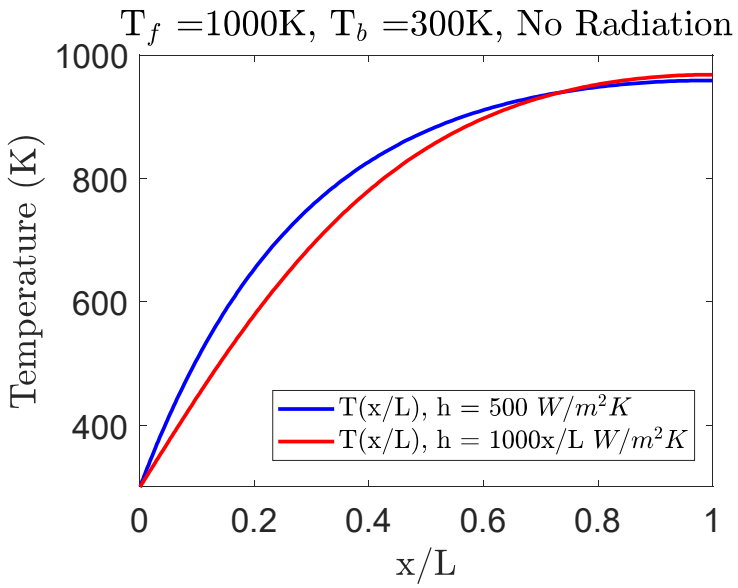

Figure 1. Numerical temperature solution results for variable film coefficient V&V Cases 4(a) and 4(b).

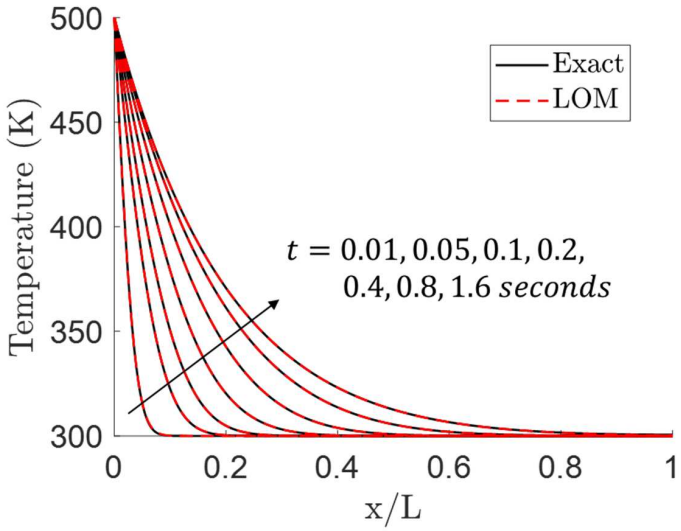

Figure 2. Comparison of exact (black curve) and numerical (red dotted curve) results for unsteady step response V&V Case 5: d = 1.0 mm, L = 10 mm, k = 16 W/mK, c = 490 J/kgK, ρ = 8050 kg/m^3, ε = 0, T_f = 300K, $T_i\ (x)$=300K, $T_b(t>0)$ = 500K, h = 1000 W/m^{2}K and h_{tip}/h = 0 (insulated)

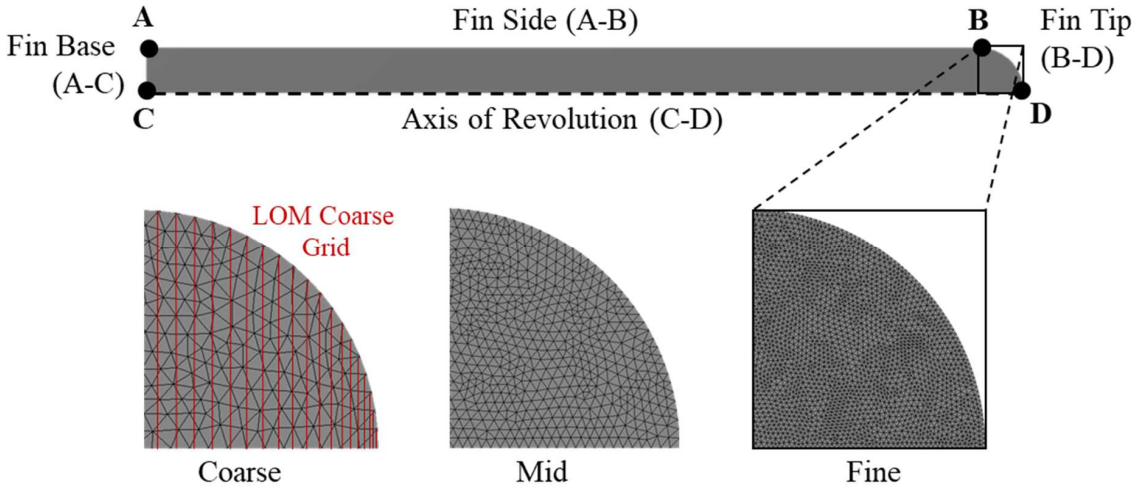

Figure 3. Geometry used for V&V Cases 6(a) and 6(b) (top) and grids used for Fluent and LOM solutions (bottom).

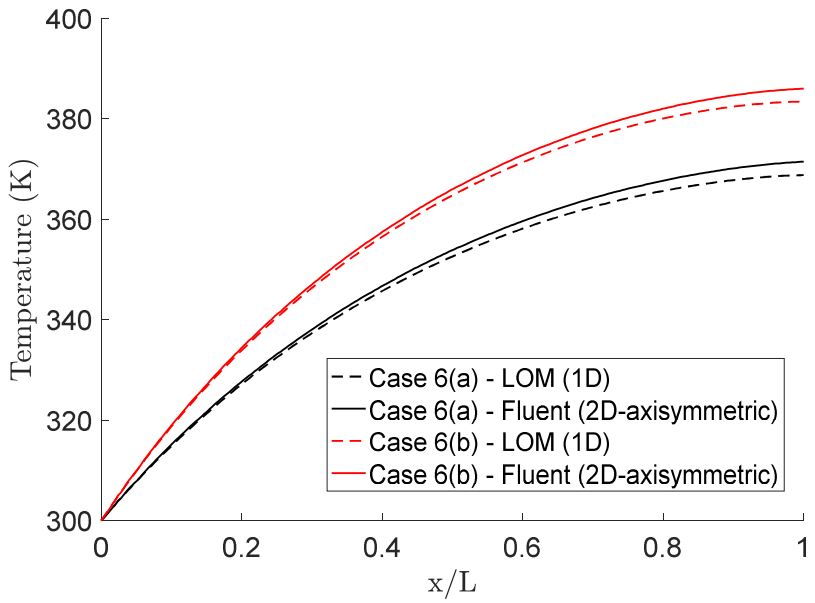

Figure 4. Comparison of fin temperature profiles for V&V Cases 6(a) and 6(b) using the Enhanced LOM and Fluent solvers.

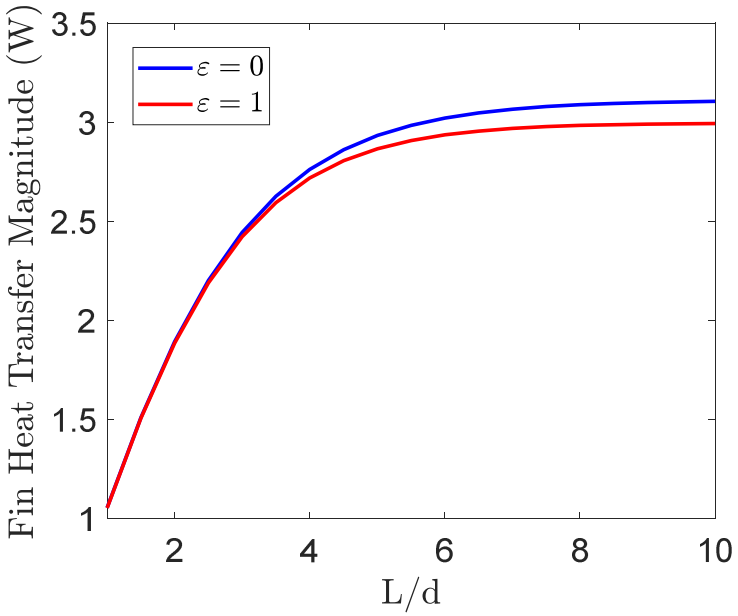

Figure 5. Numerical solution results for: d = 1.0 mm, k = 16 W/mK, ε = 0 (top/blue curve) and ε = 1.0 (bottom/red curve), T_b = 300K, T_f =1000K, T_{surr} = 300K, h = 500 W/m^{2}K and h_{tip}/h = 0 (insulated tip).

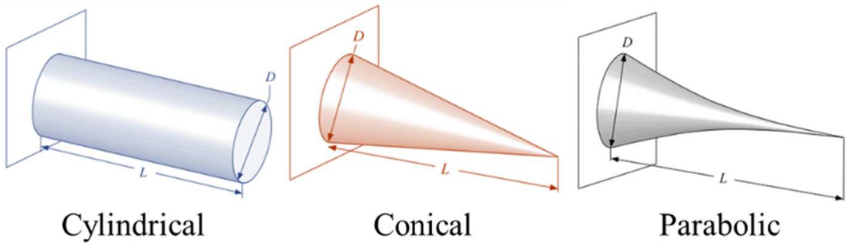

(a) Pin fin profiles for consideration: cylindrical with circular cross section (left), conical with pointed tip (middle) and concave parabolic with pointed tip (right)

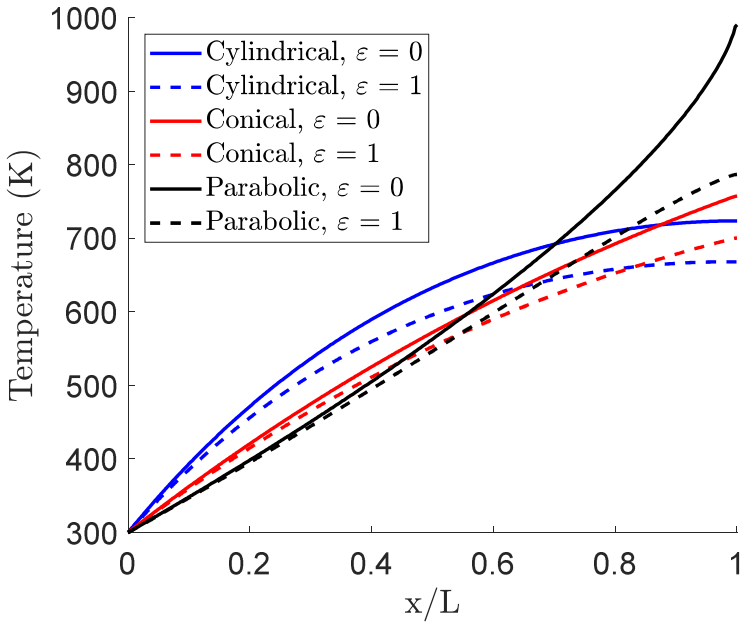

(b) Temperature variations

Figure 6. Numerical solution results for varying fin profiles with: d_{base} = 1.0 mm, L = 10 mm, k = 16 W/mK, ε = 0 (solid curves) and ε = 1.0 (dotted curves), T_b = 300K, T_f =1000K, T_{surr} = 300K, h = 100 W/m^{2}K and h_{tip}/h = 0.0.

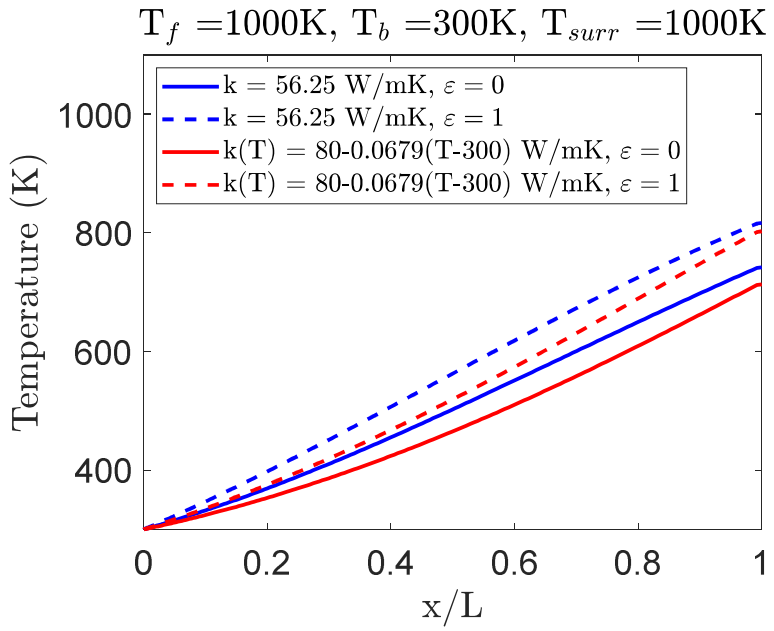

Figure 7. Numerical solution results conical fin with: d_{base} = 1.0 mm, L = 10 mm, k = 56.25 W/mK (blue curves) and k(T) = 30-0.0679(T-300) W/mK (red curves), ε = 0 (solid curves) and ε = 1.0 (dotted curves), T_b = 300K,T_f=1000K, T_{surr} = 1000K, $h(x/L)$ = 500x/L W/m^{2}K and h_{tip}/h = 0.0.

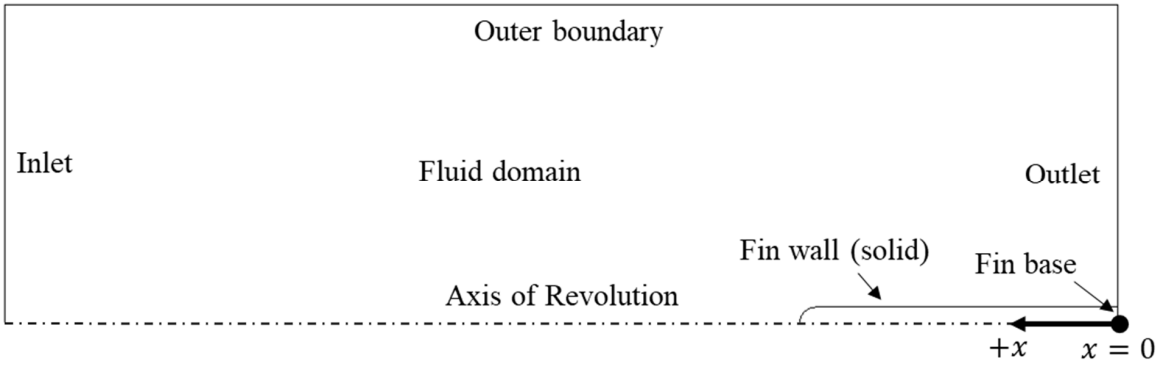

Figure 8. Computational model geometry including fin (solid) and surrounding fluid domains.

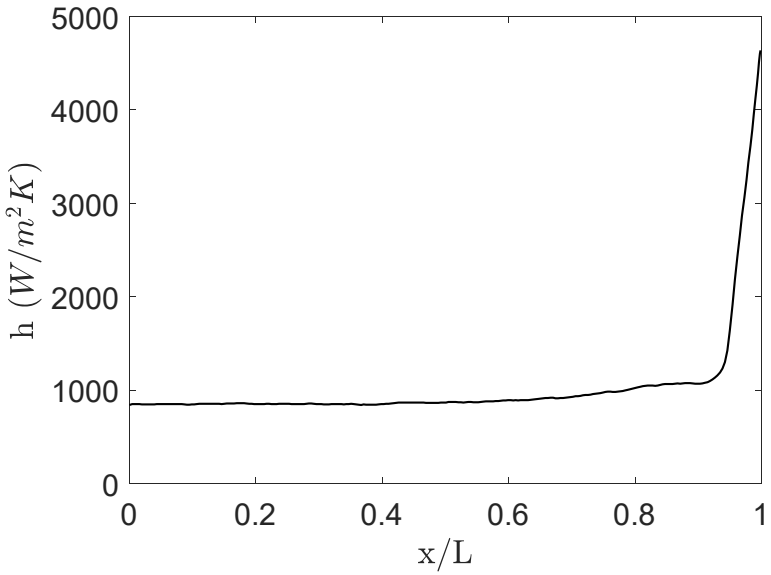

(a) Convective film coefficient profile along fin from base (*x/L*=0) to tip (*x/L*=1)

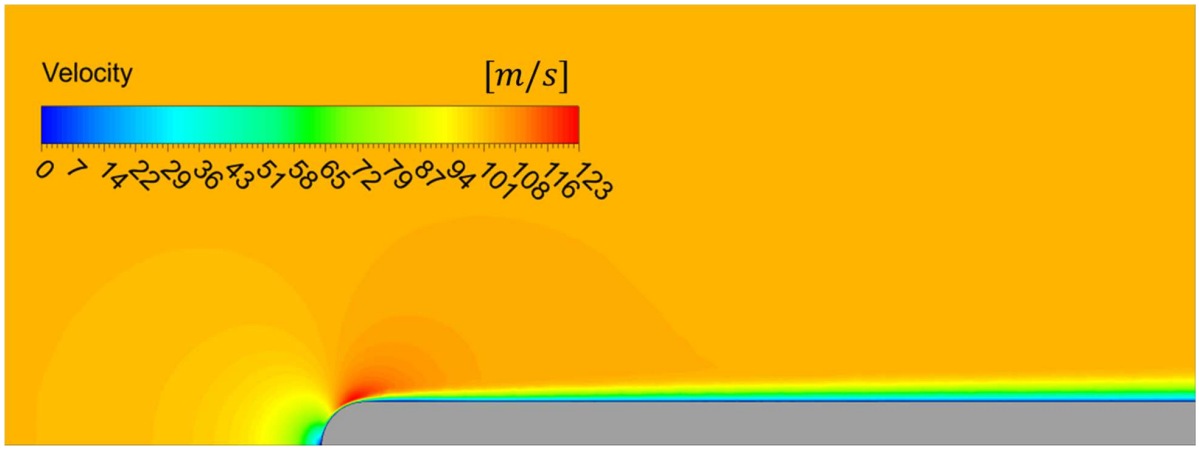

(b) Contour of velocity magnitude around fin

Figure 9. (a) Film coefficient profile on fin surface as function of non-dimensional axial location for CFD/CHT solution without radiation. (b) Contour of velocity magnitude around fin body revealing the formation of a tip stagnation region and length-wise boundary layer growth.

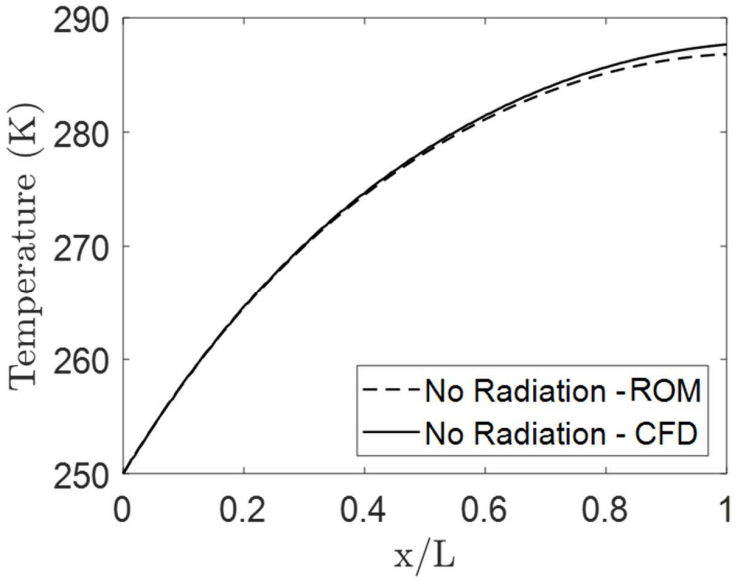

Figure 10. Temperature profile as a function of non-dimensional axial location for ROM (dashed) and CFD/CHT (solid) excluding radiation.

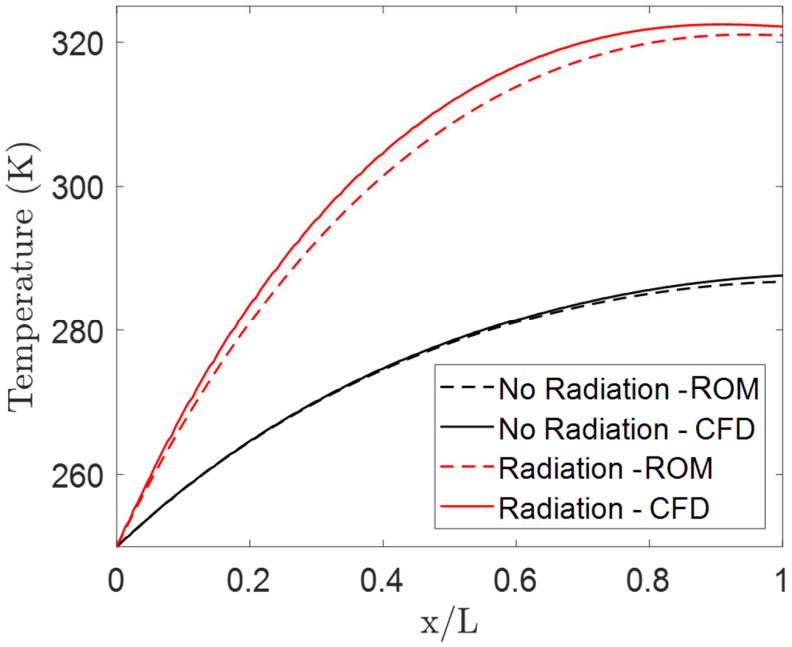

Figure 11. Temperature profiles as a function of non-dimensional axial location for ROM (dashed) and CFD/CHT (solid) for radiation with $\boldsymbol{T_{surr}}$ =1000K and $\boldsymbol{\varepsilon = \alpha = 1.0}$ (red) and no radiation (black) cases.

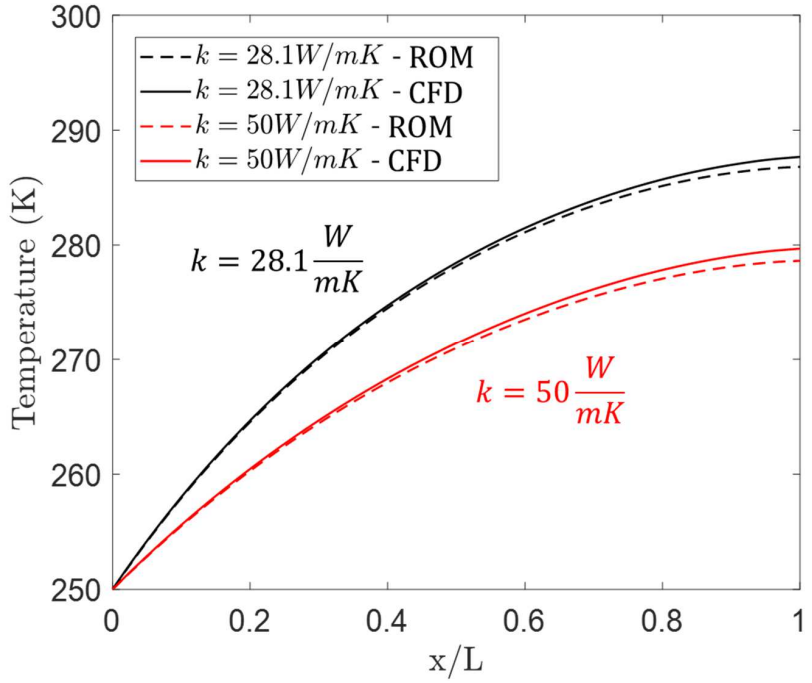

Figure 12. Temperature profiles as a function of non-dimensional axial location for ROM (dashed) and CFD/CHT (solid) for k = 50 W/mK (red) and k = 28.1 W/mK (black) cases.

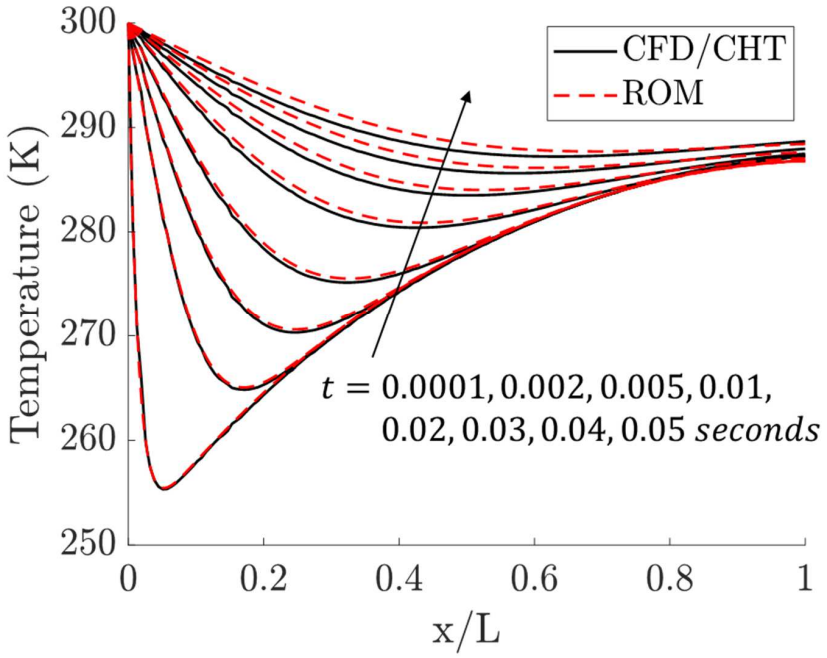

Figure 13. Temperature profiles as a function of non-dimensional axial location for ROM (red dashed) and CFD/CHT (solid black) for various times resulting from a step change in base temperature from 250K to 300K.

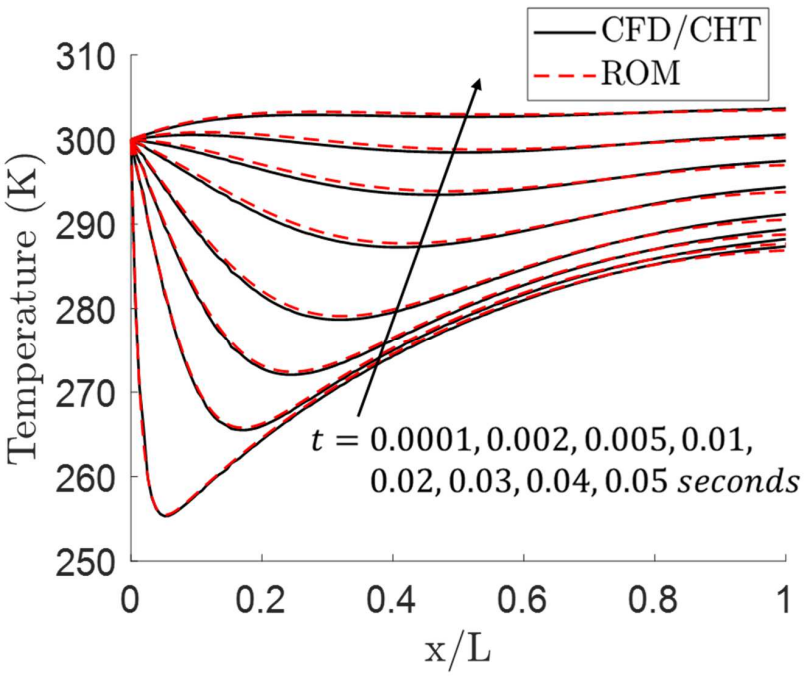

Figure 14. Temperature profiles as a function of non-dimensional axial location for ROM (red dashed) and CFD/CHT (solid black) for various times resulting from a step change in base temperature from 250K to 300K and a sudden exposure to radiation with $\boldsymbol{T_{surr} = 1000K}$, $\boldsymbol{F = 1.0}$ and $\boldsymbol{\varepsilon = \alpha = 1.0}$.

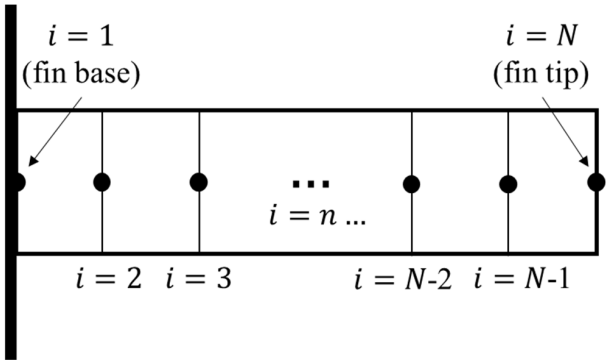

Figure A1. Spatial discretization of fin with node numbering.

TABLES

Table 1. Summary of Enhanced LOM numerical V&V cases with model inputs and chosen V&V method.

Case	1	2	3	4(a)	4(b)	5	6(a)	6(b)
Fin Profile $d(x)$ [mm]	1	1	1-x/L	1	1	1	1.0 ($x/L < 0.95$) *Dome-tip	1.0 ($x/L < 0.95$) *Dome-tip
Fin Length L $[mm]$	10	100	10	10	10	10	10	10
Film Coefficient $h(x)$ $[W/(m^2K)]$	1000	50	1000	500	1000x/L	1000	1000 ($x/L < 0.95$) 3000 ($x/L > 0.95$)	1000 ($x/L < 0.95$) 3000 ($x/L > 0.95$)
Tip Film Coefficient h_{tip} $[W/(m^2\,K)]$	1000	0	0	0	0	0	3000	3000
Thermal Conductivity $k(T)$ $[W/mK]$	16	16	16	16	16	16	$100 + 0.5(T - 300)$	$100 + 0.5(T - 300)$
Radiation ε $[-]$ at T_{surr} $[K]$	None	1.0 at 0K	None	None	None	None	None	1.0 at 1000K
Steady/ Unsteady	Steady	Steady	Steady	Steady	Steady	**Unsteady	Steady	Steady
Fluid Temp. T_f $[K]$	1000	0	1000	1000	1000	300	500	500
Base Temp. T_f $[K]$	300	1500	300	300	300	300 ($t < 0$) 500 ($t > 0$)	300	300
V&V Method	Exact Soln.	Exact Soln.	Exact Soln.	Huang and Chen, 1985	Huang and Chen, 1985	Exact Soln.	ANSYS Fluent	ANSYS Fluent

* $d(x) = \sqrt{1 - 4\left[L\left(\frac{x}{L} - 0.95\right)\right]^2}$ for $(x/L > 0.95)$

**Additionally, $\rho = 8050\,\frac{kg}{m^3}$ and $c_p = 490\,\frac{J}{kgK}$

Table 2. Comparison of Fluent and LOM results for V&V Cases 6(a) and 6(b), including influence of grid resolution.

Case	Grid	2D Elements (Fluent)	1D Elements (Enhanced LOM)	Fluent Base Heat Flux $[MW/m^2]$	Enhanced LOM Base Heat Flux $[MW/m^2]$	Fluent Tip Temperature $[K]$	Enhanced LOM Tip Temperature $[K]$
6 (a)	Coarse	6,297	249	-6.59	-6.47	371.5	368.8
6 (b)	Coarse	6,297	249	-8.34	-8.22	386.0	383.4
6 (a)	Mid	25,257	512	-6.59	-6.48	371.5	369.0
6 (b)	Mid	25,257	512	-8.34	-8.23	386.0	383.7
6 (a)	Fine	103,800	1017	-6.59	-6.49	371.5	369.1
6 (b)	Fine	103,800	1017	-8.34	-8.23	386.0	383.7

Table 3. CFD/CHT boundary conditions

Boundary Name	Condition Type	Input Parameters
Inlet	Pressure far-field	$M = 0.3, T_s = 294.7K, P_s = 99460Pa$
Outer boundary	Pressure far-field	$M = 0.3, T_s = 294.7K, P_s = 99460Pa$
Outlet	Pressure far-field	$M = 0.3, T_s = 294.7K, P_s = 99460Pa$
Fin base	Temperature	$T_b = 250K$
Fin wall	Coupled wall	No-slip wall
Axis of Revolution	Axis of revolution	-

6. Conclusions and Outlook

This present work focused on two main areas necessary for advancing the development of total temperature sensors for new and existing operating environments. The first sought to better understand how probe geometry and flow condition impacts the convective heat transfer on the sensor surface, influencing sensor response to conduction, radiation and transient effects using Computational Fluid Dynamics (CFD) with Conjugate Heat Transfer (CHT) techniques. The second involved the development of a reduced-order model technique for evaluation of sensor thermal performance for improving the estimation of steady and unsteady sensor errors due to multi-mode heat transfer, especially radiation.

6.1 Conclusions

New total temperature measurement locations and flow environments have created a need for better informed design models, capable of evaluating new probe designs. This Dissertation is comprised of three papers that summarize the contributions made by the author during his Ph.D. studies, addressing this need for improved probe performance models and evaluation methods.

The first paper was motivated by the limitations of existing probe performance models to evaluate the influence of geometric modifications on overall probe performance. CFD/CHT simulations were performed over a variety of vented-shield probe geometries and free stream flow environments, revealing many details of the flow field local to the sensor and how this flow ultimately impacts the heat transfer into the sensor. The geometric modifications investigated were the location of the shield vent/bleed holes relative to the length of the shield, sensor diameter relative to the inner diameter of the shield, and shield outer diameter relative to the overall thickness of the strut. For all sensor geometries investigated, there was a significant pressure gradient observed directed normal to the leading edge of the strut due to expected flow deceleration as the free-stream flow approaches the probe body. The sensor and shield are located within this pressure gradient. The shield vent discharge pressure environment is directly impacted by this pressure gradient, influencing the amount of oncoming flow that is ingested by the shield. It is this shield internal flow that ultimately drives forced convection heat transfer over the sensor surface, heavily influencing the impact of conduction, radiation and transient errors on the sensor indicated temperature. Movement of the vents closer to the strut leading edge subjected the vent exit flow to

higher discharge pressures, reducing both the movement of flow within the shield and convection heat transfer into the sensor. The opposite effect was noted for movement of the vent holes further away from the strut leading edge. Changing the sensor diameter relative to a fixed shield inner diameter had virtually no influence on the amount of flow entering the shield, however, this does cause a change in the flow hydraulic area within the shield, impacting flow velocity. Higher velocity increases convection heat transfer, but this effect is offset by the reduction in sensor length to diameter ratio, known to increase the influence of conduction errors. Lastly, changes in shield outer diameter relative to the maximum strut thickness influenced the size and location of the adverse pressure gradient caused by the strut. Increasing the shield outer diameter reduced the vent discharge pressure, resulting in increased flow inside the shield. For each geometric modification, the resulting mass flow rate inside of the shield and convection heat transfer coefficients along the sensor tip and sides was quantified. The observed mass flow ratio for each case was normalized by a reference mass flow rate (based on known flow and sensor geometric parameters) and related to the three geometric parameters varied in this study to form an analytic empirical correlation that can be used to directly estimate sensor local flow inside the shield. Of great significance was the observation that this sensor local flow correlation is independent of free stream flow Reynolds Number, verified by comparing the mass flow ratio across a range of flow temperature and pressure environments from 70°F to 2500°F and 1 atm to 10 atm, respectively. The convection heat transfer coefficients for each case were used to generate an analytic empirical model for evaluating sensor tip and side film coefficient as a function of shield internal flow Reynolds numbers given by the new mass flow ratio correlation. Together, these correlations provide the necessary information to close existing sensor thermal performance models, without the need for additional experimentation or simulations.

The second and third papers were motivated by the inability of existing low-order models to handle a more general treatment of radiation and transient errors due to the limited availability of analytic solutions to the governing heat transfer equations. Historically, sensors for total temperature probes have been modeled as pin fins due to their long, slender bodies, and is the basis for existing analytic conduction error models from the literature. These analytic models are mainly limited to steady state conduction error predictions, significantly limiting the definition of sensor film coefficient surface distribution, sensor geometric profile, and sensor material properties. Furthermore, there are no existing analytic solutions to the 1-D fin equations with combined conduction, convection, and radiation that is satisfactory for practical use. In these papers, a highly generalized for of the 1-D pin fin equations is solved using a second-order finite-differencing scheme in MATLAB (code provided) for the evaluation of sensor error under multi-mode heat transfer environments.

The solution has been generalized to allow for variable convective heat transfer coefficients over the sensor tip and sides ($h(x)$), axial variation in sensor cross-section area ($A(x)$), temperature dependent thermal conductivity ($k(T)$), more realistic radiation treatment, and transient response to changing boundary conditions (transient response only included in the third paper). Using this generalized numerical solution, several example cases were conducted to show how sensor performance predictions due to variations in typical sensor design parameters compare when considering both solutions with and without radiation. In some cases, the influence of radiation was shown to be highly significant (e.g. conical tipped sensors). Additionally, a novel, reduced-order modeling (ROM) technique was developed, which integrates heat transfer coefficient information from a complex CFD/CHT simulation with the new generalized numerical fin solution code, boasting significantly reduced run times with comparable accuracy to the original full-scale simulations. Several examples were included showing this ROM approach to rapidly and accurately adjust an existing steady-state, no radiation, solution for desired radiation effects, changed material properties, and even predict the transient response to changing the base temperature boundary condition, all without the need to run additional CFD/CHT simulations. This practicality gives a designer more flexibility in defining model parameters when performing high fidelity computations, since many subsequent parameter adjustments can be made using the ROM approach with high accuracy. The method relies on the assumption that convection heat transfer coefficients for a baseline case is largely insensitive to changes in boundary and initial conditions and/or changes in case parameters relative to the baseline. Of course, such an assumption cannot be completely general. But, we have demonstrated that it can be prudently applied to cover rather large changes relative to a baseline case, resulting in very substantial benefits in computational efficiency.

In conclusion, the improved understanding of the influence probe geometry has on the convection heat transfer coefficient distribution over the sensor surface in a vented-shield, combined with the new generalized fin solution code, provides a powerful suite of tools to be used by probe designers for the evaluation of new sensor designs in a variety of flow environments.

6.2 Outlook

There are several key areas to continue investigating for fully characterizing total temperature probe performance, as follows:

- For all computational results presented in this work, a steady, low turbulence, free stream environment was used. In light of more recent experimental investigations of sensor perfor-

mance at Virginia Tech (not covered in this body of work), increasing free stream turbulence has the potential to significantly impact sensor performance.

- The characterization of off-angle sensor performance (i.e. flow not directed parallel to sensor) was not included here. It has been historically shown that probes with a Kiel head or vented-shield design have great insensitivity to flow angle with respect to velocity error. This insensitivity to angle has not been directly shown for probes experiencing large conduction effects.
- In harsh environments (high-temperature and/or high-velocity), sensor survivability becomes a significant consideration in the probe design process. The further incorporation of structural modeling with the sensor thermal performance methods presented here could greatly serve to reduce the risk of sensor failures during extreme condition testing.